A STUDY ON THE DEFECT CHEMISTRY OF BARIUM-STRONTIUM-COBALT-IRON-OXIDE SYSTEM

BY

JAE-IL JUNG

A THESIS

SUBMITTED TO THE FACULTY OF

ALFRED UNIVERSITY

IN PARTIAL FULFILLMENT OF THE REQUIREMENTS
FOR THE DEGREE OF

DOCTOR OF PHILOSOPHY

IN

CERAMICS

ALFRED, NEW YORK

JULY, 2010

Alfred University theses are copyright protected and may be used for education or personal research only. Reproduction or distribution in any format is prohibited without written permission from the author.

A STUDY ON THE DEFECT CHEMISTRY OF BARIUM-STRONTIUM-COBALT-IRON-OXIDE SYSTEM

BY

JAE-IL JUNG

B.S. KYUNGPOOK NATIONAL UNIVERSITY, SOUTH KOREA (1996)

M.S. UNIVERSITY OF PENNSYLVANIA (2006)

SIGNATURE OF AUTHOR (SIGNATURE ON FILE)

APPROVED BY (SIGNATURE ON FILE)
DOREEN D. EDWARDS, ADVISOR

(SIGNATURE ON FILE)
ALASTAIR N. CORMACK, ADVISORY COMMITTEE

(SIGNATURE ON FILE)
SCOTT T. MISTURE, ADVISORY COMMITTEE

(SIGNATURE ON FILE)
WALTER A. SCHULZE, ADVISORY COMMITTEE

(SIGNATURE ON FILE)
CHAIR, ORAL THESIS DEFENSE

ACCEPTED BY (SIGNATURE ON FILE)
DOREEN D. EDWARDS, DEAN
KAZUO INAMORI SCHOOL OF ENGINEERING

ACCEPTED BY (SIGNATURE ON FILE)
NANCY EVANGELISTA, ACTING ASSOCIATE PROVOST
AND DIRECTOR OF GRADUATE AND PROFESSIONAL PROGRAMS
ALFRED UNIVERSITY

ACKNOWLEDGMENTS

First of all, I am heartily thankful to my thesis advisor, Professor Doreen D. Edwards, whose advice and support enabled me to go through the itinerary of this Ph. D pursuit. I am particularly grateful for her encouragement and guidance in the development of writing skills as well as in my research. She is the one who opened the gate for me to the field of defect chemistry study and writing skills. Her generosity and trust during struggling times will not be forgotten in my life. I also wish to thank Professors Alastair N. Cormack and Walter A. Schulze for serving as my committee members. I specially give thanks to Professor Scott T. Misture for his active involvements and discussions.

This work was supported by New York State Office of Science, Technology and Academic Research (C030093), Applied Coatings, Inc. and New York State College of Ceramics.

I wish to thank a number of people who contributed to this work. I am thankful to the Dr. James Ovenstone for his devoted contribution and cowork in XRD and preliminary study. I wish to thank Professor Nathan P. Mellott for his kind advice and great help in XPS study. Thanks are given to Francis A. Williams for furnishing electrical equipment. I am indebted to Gerald L. Wynick for his cordial fellowship as a Christian friend as well as for his great advice and direction in microstructure works. FT-IR study would not have been possible without the clear explanation and training of Dr. Robert A. Lacey. I also give a cordial appreciation to Professor Michele M. Hluchy and Jean A. Bilson for the unlimited help in the measurement of Iodometric titration. I wish to thank Matthew R, Brophy for helping with new TG-DTA. I also wish to thank Dr. Jake W. Amoroso for various labwares and sincere discussions. I am indebted to Dr. Michelle A. Hall for her devoted helps and advices.

It has been a great pleasure to work with several people. I wish to thank my past and present lab-mates: Dr. Jake W. Amoroso, Stephen B. Sanford, Brian A. Riley, Emily S. Asenath, Brittany L. Higgins, Kara E. Vaneck. I enjoyed sharing offices with Andrew B. Crawford, Istvan L. Szabo, Aladdin S. Geleil, Sean M. Breed and Liang Shen.

I give thanks to Pastor Charles L. and Donna Dear and John C. Huges for their continuous prayer and fellowship. I wish to thank Deacon San-Beum Lee and Deacon Tae-Ja

Hong for their relentless prayer and love. I am also thankful to Choel-Hyo Lee, Sang-Wok Park and other Bible study group members in Korea who prayed for me all throughout my pursuit of this study.

I wish to thank my parents, brothers and sister, who have been forever my supporters.

I give thanks to my wife, Jeong-A Cho, for her sacrificial dedication, support and encouragement without which this study was not possible. I also wish to thank my two daughters, Yoo-Jin and Hyun-Ah Jung, who have been my pleasant shelter.

Last of all, I dedicate this tiny academic achievement to the Lord, the great Savior and Provider in my life.

TABLE OF CONTENTS

LIST OF TABLES

Page

LIST OF FIGURES

Page

ABSTRACT

BSCF, or $Ba_{0.5}Sr_{0.5}Co_{0.8}Fe_{0.2}O_{3-\delta}$, is a well known mixed electronic and ionic conductor (MEIC) that has been considered as potential cathode for intermediate temperature solid oxide fuel cells (IT-SOFCs).

Initial 4-point conductivity measurements of $Ba_{0.5}Sr_{0.5}Co_xFe_{1-x}O_{3-\delta}$ (x = 0, 0.2, 0.4, 0.6, and 0.8) as a function of temperature in air were conducted with Pt-paste electrodes. Below 400°C, conductivity was thermally activated (E_a = 0.21 – 0.4eV). Above 400°C, conductivity decreased with increasing temperature, which was attributed to a decrease in p-type carriers resulting from the formation of oxygen vacancies associated with the reduction of Fe^{4+}.

The conductivity of BSCF (x = 0.8) as a function of pO_2 was also measured. Above 400°C for pO_2 > 0.01atm, the conductivity increased with increasing pO_2, confirming *p*-type conduction. For pO_2 < 0.01atm, a slight increase in conductivity with decreasing pO_2 was observed. To further investigate the possibility of *n*-type conduction in BSCF at low pO_2, the conductivity and thermopower simultaneously as a function of temperature and pO_2 for five compositions of $Ba_{0.5}Sr_{0.5}Co_xFe_{1-x}O_{3-\delta}$ ($0 \leq x \leq 0.8$) were measured. These measurements enable better understanding of the conduction mechanism of BSCF according to the changes of temperatures and oxygen partial pressures.

With XPS analysis, as cobalt concentration increases, the trend of peak shifts in O_{1s} and cations (Co, Fe) has been studied. This study provides the fundamental background of bonding state on the surface of BSCF ceramics.

I. INTRODUCTION

A Solid Oxide Fuel Cell (SOFC) is generically composed of a cathode, an electrolyte and an anode. As an oxygen anion passes from the negative cathode to the positive anode within the fuel cell according to the oxygen partial pressure gradient, the electron separated from the oxygen anion at the anode becomes the source of the produced energy. When SOFC systems were first introduced, the operation temperature was about 1000°C. But, this range of temperature hindered the real application of SOFC, because thermally induced catastrophic failures shortened application time below that which the commercial benefit requires. In order to overcome these kinds of technical problems, Intermediate Temperature Solid Oxide Fuel Cells (IT-SOFCs), applicable below 700°C, were introduced. Accordingly, the proper materials suitable to this condition are required.

Figure 1 shows the transitional trend of cathode materials from triple phase

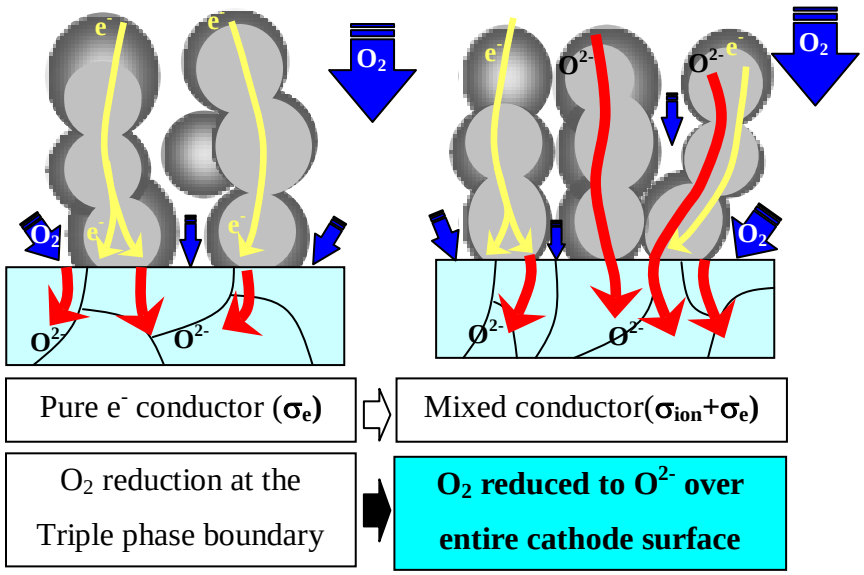

Figure 1. Schematic diagram for the transition of cathode material from triple phase boundary (TPB) system to mixed electronic ionic conductor (MEIC). Adapted from Weber.[1]

boundary (TPB) systems to mixed electronic ionic conductor (MEIC). In triple phase boundary (TPB) systems, electrons and oxygen gas are transported separately through cathode and reacted into an oxygen anion at the triple phase boundary on the electrolyte surface. MEICs as the cathode material allow both electronic and ionic carriers to be simultaneously transported into the electrolyte, as shown in Figure 1, so that the system can transport charge carriers more efficiently. In addition to SOFC, MEIC can be used in diverse application fields such as oxygen membrane, proton conductor, etc. Several perovskite types of materials such as LSC ($La_{1-x}Sr_xCo_3O_{3-\delta}$) LSCF ([La, Sr][Co, Fe]$O_{3-\delta}$) and BSCF([Ba, Sr][Co, Fe]$O_{3-\delta}$) have been introduced as promising MEICs.[2-9] [10] However, there are still some unsolved technical problems in order for these materials to be applied; the selection of proper materials, optimized processing for mass production, stability, performance time, etc. Defect chemistry can be helpful to better understand a material system from diverse standpoints such as crystal structure, electrical conductivity and microstructure.

This study focuses on the defect chemistry of BSCF perovskite ceramics, mainly on the effect of changing ratios between cobalt and iron cations in B-sites of $Ba_{0.5}Sr_{0.5}Co_xFe_{1-x}O_{3-\delta}$ (BSCF).

As preliminary studies, XRD analysis was carried out by changing temperature and oxygen partial pressure, which set the limitation of oxygen partial pressure before it decomposes. Also, the microstructure analysis was carried out to understand the initiation of decomposition under strong reducing atmosphere. The oxygen vacancies formed due to changes in temperature and oxygen partial pressure are shown in Figure 2. The oxygen vacancy formation is also expected due to composition changes.

Oxygen vacancy formation is intimately related with charge valence states of B-sites in BSCF, which will determine the conduction mechanism of electrical properties. As a way of a quantitative approach to BSCF conductivity mechanism, the carrier concentrations were measured by the thermoelectric power method, simultaneously with DC conductivity measurement. Additionally, XPS analysis was conducted to specifically understand the effect of the changing ratio of Co/Fe in BSCF and the heat treatment on bonding energy (BE) state of cations, which is intimately correlated with oxygen anion.

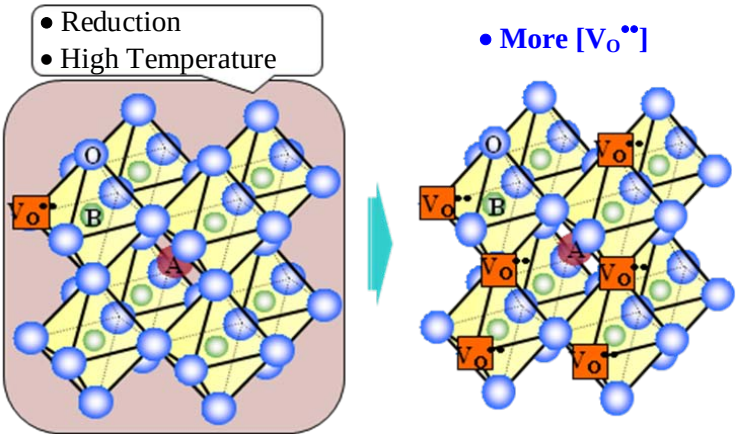

Figure 2. Schematic diagram for the formation of oxygen vacancies as a function of temperature and oxygen partial pressure in perovskite structure. Adapted from Zeng.[11]

The extensive study of where and how oxygen vacancies are formed within the BSCF structure is useful. The results will provide thermodynamic- and/or kinetic-information from the relation between cations and oxygen as exemplified by the decomposition model in Figure 3.

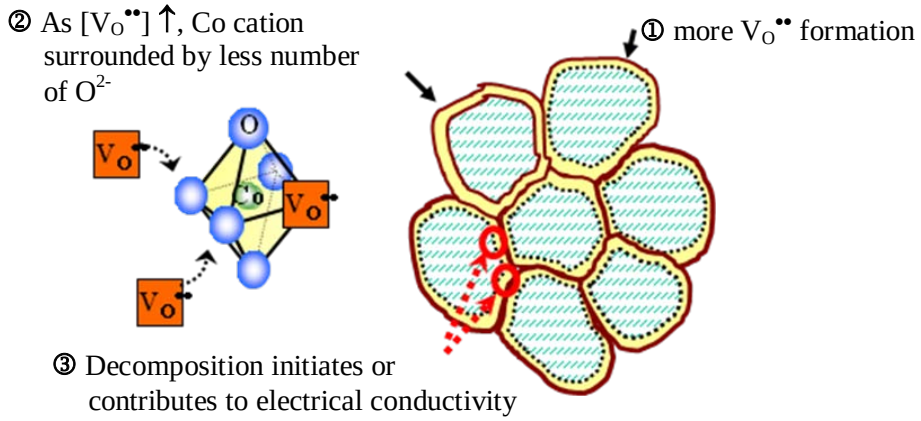

Figure 3. Schematic diagram of expected structural decomposition, 2nd phase formation or electrical conductivity affected by oxygen vacancy formation.

A. References

1. A. Weber and E. Ivers-Tiffée, "Materials and Concepts for Solid Oxide Fuel Cells (SOFCs) in Stationary and Mobile Applications," *J. Power Sources,* **127** [1-2] 273-83 (2004).

2. Z. Chen, R. Ran, W. Zhou, Z. Shao, and S. Liu, "Assessment of $Ba_{0.5}Sr_{0.5}Co_{1-y}Fe_yO_{3-\delta}$ (Y = 0.0-1.0) for Prospective Application as Cathode for IT-SOFCs or Oxygen Permeating Membrane," *Electrochim. Acta,* **52** [25] 7343-51 (2007).

3. J. A. Lane, S. J. Benson, D. Waller, and J. A. Kilner, "Oxygen Transport in $La_{0.6}Sr_{0.4}Co_{0.2}Fe_{0.8}O_{3-\delta}$," *Solid State Ionics,* **121** [1-4] 201-8 (1999).

4. A. Petric, P. Huang, and F. Tietz, "Evaluation of La-Sr-Co-Fe-O Perovskites for Solid Oxide Fuel Cells and Gas Separation Membranes," *Solid State Ionics,* **135** [1-4] 719-25 (2000).

5. A. Mineshige, M. Inaba, T. Yao, Z. Ogumi, K. Kikuchi, and M. Kawase, "Crystal Structure and Metal-Insulator Transition of $La_{1-x}Sr_xCoO_3$," *J. Solid State Chem.,* **121** [2] 423-9 (1996).

6. J. Mizusaki, T. Matsuura, S. Yamauchi, K. Fueki, and J. Tabuchi, "Electrical Conductivity and Seebeck Coefficient of Nonstoichiometric $La_{1-x}Sr_xCoO_{3-D}$," *J. Electrochem. Soc.,* **136** [7] 2082-8 (1989).

7. L. W. Tai, M. M. Nasrallah, H. U. Anderson, D. M. Sparlin, and S. R. Sehlin, "Structure and Electrical Properties of $La_{1-x}Sr_xCo_{1-y}Fe_yO_3$. Part 1. The System $La_{0.8}Sr_{0.2}Co_{1-y}Fe_yO_3$," *Solid State Ionics,* **76** [3-4] 259-71 (1995).

8. L. W. Tai, M. M. Nasrallah, H. U. Anderson, D. M. Sparlin, and S. R. Sehlin, "Structure and Electrical Properties of $La_{1-x}Sr_xCo_{1-y}Fe_yO_3$. Part 2. The System $La_{1-x}Sr_xCo_{0.2}Fe_{0.8}O_3$," *Solid State Ionics,* **76** [3-4] 273-83 (1995).

9. Y. Teraoka, H. M. Zhang, K. Okamoto, and N. Yamazoe, "Mixed Ionic-Electronic Conductivity of $La_{1-x}Sr_xCo_{1-y}Fe_yO_{3-\Delta}$ Perovskite-Type Oxides," *Mater. Res. Bull.,* **23** [1] 51-8 (1988).

10. J. Vondrák and L. Dolezal, "The Electric and Electrochemical Properties of Electrode Perovskite $La_{1-x}Sr_xCoO_3$," *Electrochim. Acta,* **29** [4] 477-83 (1984).

11. P. Zeng, Z. Chen, W. Zhou, H. Gu, Z. Shao, and S. Liu, "Re-Evaluation of $Ba_{0.5}Sr_{0.5}Co_{0.8}Fe_{0.2}O_{3-\Delta}$ Perovskite as Oxygen Semi-Permeable Membrane," *J. Membr. Sci.,* **291** [1-2] 148-56 (2007).

II. LITERATURE REVIEW

A. Technolonological Application of BSCF

BSCF is being considered as a cathode for intermediate-temperature solid oxide fuel cells (IT- SOFC) and oxygen separation membrane. A strong candidate of cathode materials for IT-SOFC, BSCF incorporated into a thin-film doped ceria fuel cell showed high power densities of 1,010 $mWcm^{-2}$ and 402 $mWcm^{-2}$ at 600°C and 500°C, respectively, when operated with humidified hydrogen as at the cathode side.[1] Also, as a MEIC material, BSCF has attracted much attention in recent years for its applications in oxygen separation, partial oxidation of methane to syngas and construction membrane reactors for catalytic conversion of light hydrocarbons.[2-4] For practical applications, a dense oxygen separation membrane should possess the following properties: (1) high oxygen permeation flux with both high oxygen ionic and electronic conductivities; (2) structural stability within appropriate ranges of temperature and oxygen partial pressure; (3) sufficient mechanical strength and chemical compatibility.[4] Among many materials, perovskite or perovskite-related type oxides were found to be an outstanding material for oxygen permeation as MEIC.[3]

B. Crystal Structure and Phase Stability of BSCF

BSCF possesses a cubic perovskite structure. B-site metal ions (Co, Fe) are coordinated by six oxygen ions to form the close packing of BO_6 octahedra. A-site ions (Ba^{2+}(1.61Å), Sr^{2+}(1.44Å)) are coordinated by 12 adjacent oxygen ions and fit between the BO_6 octahedra as shown in Figure 4. The ideal lattice parameter, a, can be obtained with $a = \sqrt{2}\ (R_A + R_O) = 2(R_B + R_O)$. On the basis that the lattice parameter, a, is equal to $\sqrt{2}\ (R_A + R_O)$, the calculated lattice parameter for BSCF should be around 4.25Å. On the other hand, the calculated lattice parameter from $a = 2\ (R_B + R_O)$ can be about 4.02Å.

The measured lattice constant by XRD analysis is around 3.95Å,[5] which implies that BO_6 octahedra determines lattice constant with $a = 2(R_B + R_O)$. Therefore, it is expected that the electron clouds surrounding A-site cations could be overlapped with

those of oxygen anions because of the shortened distance between A-site cations, especially Ba^{2+}, and oxygen anions. Particularly, the bonding state between Ba cation and oxygen anions influence the BE of e^- using XPS. Vasquez *et al.* reported that, as the XPS BE of Ba $4d_{5/2}$ increases from 87.2 to 88.0 eV, the Ba-O bond length linearly increases from 2.802 to 2.818Å in the Tl –cuprate system, which is expected from the Madelung energy change.[6]

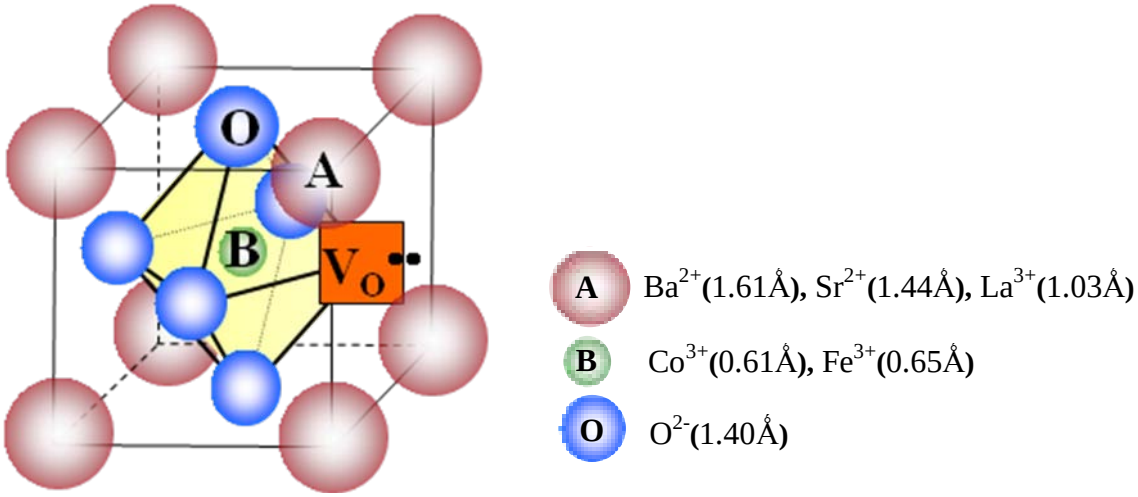

Figure 4. Crystal structures of LSC, LSCF and BSCF.

And, the non-ideal crystal structure keeps a significant concentration of oxygen vacancies as shown in Figure 4, which also would affect unit cell volume size. In addition to the unit cell volume expansion, the calculated tolerance factor (t_f) increases from 1.042 to 1.052 as cobalt concentration increases from x=0 to 0.8 in $Ba_{0.5}Sr_{0.5}Co_xFe_{1-x}O_{3-\delta}$ according to Equation (1)[7]

$$t_f = \frac{(0.5 * r_{Ba^{2+}} + 0.5 * r_{Sr^{2+}} + r_{O^{2-}})}{\sqrt{2}\,(x * 0.4 * r_{Co^{3+}} + x * 0.6 * r_{Co^{4+}} + (1-x) * r_{Fe^{4+}} + r_{O^{2-}})} \quad (1)$$

where, r_{Ba2+} = 1.61Å, r_{Sr2+} = 1.44Å, r_{Co4+} = 0.53Å, r_{Co3+} = 0.61Å, r_{Fe4+} = 0.59Å, r_{Fe3+} = 0.65Å and r_{O2-} = 1.40Å.[8] Perovskite is known to be structurally stable, when the

tolerance factor (t_f) ranges from 0.95 to 1.06, approximating to 1. When t_f deviates from this range, the crystal structure is prone to be unstable. Therefore, the combined effect of t_f and oxygen vacancy will be the determinant in crystal structure stability.

In comparing SCF and BSCF, on the assumption that all of the B cations are in the 3+ oxidation state, δ=0.5, the tolerance factors for SCF and BSCF are 0.977 and 1.00, respectively. If we assume that all cobalts for SCF and BSCF are in the Co^{2+} state, the tolerance factors are 0.93 and 0.957, respectively, so that reduction of Co^{3+} to Co^{2+} is acceptable to the phase stability of BSCF but undesirable in SCF.[9] This explains why SCF is more prone to forming the brownmillerite phase according to temperature or pO_2, even though the initial oxygen stoichiometry of SCF (3-δ=2.7) is higher than BSCF (3-δ=2.48).

The real BSCF perovskite possesses a significant amount of oxygen vacancies, which influence the coordination number, lattice constant, inter-atomic bonding distances and electrostatic properties. P. Zeng *et al.* reported that, when oxygen vacancies are formed, the coordination number will decrease and the crystal lattice will shrink because of the decreasing effective radius of metal ion.[10] But, our group showed that, as cobalt concentration increases from x=0 to 0.8 in $Ba_{0.5}Sr_{0.5}Co_xFe_{1-x}O_{3-\delta}$, the lattice constant (a) increased from 3.931 to 3.986Å in XRD analysis.[11] The unit cell volume expansion is attributed to the formation of oxygen vacancy in perovskite crystal structure.

The diverse structure phases of $BaFeO_{3-\delta}$ can be divided into three domains according to different oxygen nonstoichiometry ranges: (i) $BaFeO_{2.65-2.56}$ with a two-phase mixture of the 6H hexagonal phase and of the orthorhombic phase with a microdomain texture, (ii) $BaFeO_{2.56-2.54}$ with a phase of orthorhombic symmetry and (iii) $BaFeO_{2.54-2.50+\delta}$, a phase showing the intergrowth of six types of domains.[12]

S. McIntosh *et al.* reported that the cubic perovskite structure of $SrCo_{0.8}Fe_{0.2}O_{3-\delta}$ (SCF) with randomly distributed oxygen vacancies between 600 and 900°C at pO_2 = 1 atm turns into vacancy ordered brownmillerite phase with space group I_{cmm} as pO_2 goes below 1 atm and temperature below 800°C.[13-14] The octahedra in the brownmillerite phase are significantly distorted and tilted with an elongated apical bond length relative to the equatorial bond length which causes anisotropic thermal expansion, and leads to

difficulties in applying SCF as a membrane material. The higher oxygen transport of BSCF over SCF can be explained by two aspects : i) the higher oxygen transport rates in the vacancy disordered cubic perovskite than in the brownmillerite phase and ii) the higher initial oxygen stoichiometries of BSCF with 2.70 than SCF with 2.48 in room temperature.[9,14] However, when larger Ba^{2+} cations are doped into the Sr^{2+} site in SCF the average A-O and B-O bond distances could increase, with a subsequent destabilization of the higher B cation oxidation states.[13]

BSCF is reported to start collapsing at oxygen partial pressure below 10^{-8} atm, because the cobalt ion in perovskite can be reduced to cobalt metal at an oxygen partial pressure lower than 10^{-8} atm accompanied with the deterioration of the perovskite structure and the decrease of oxygen permeability.[10,15-16] This means that the valence state of the B-site cation, especially cobalt, can be influential on the perovskite structure stability. And, thermal expansion is enhanced both by the reduction of B site ions into lower valence and decrease B-O bond strength according to Pauling's second rule.[10] Both the high thermal expansion coefficient (TEC) and low chemical stability are closely related with the B site ions, particularly with cobalt concentration in BSCF the structure, because cobalt ions are easily reduced.[17 18 19] A more detailed discussion about phase stability studies for BSCF conducted as a part of this project will be presented in Chapter III.

C. Oxygen Non-Stoichiometry and Valence of Cations in BSCF

Oxygen non-stoichiometry is closely related with the valences of cations in the perovskite structure and significantly influences the crystallographic structure. The B-cation oxidation state is associated with the oxygen release deduced from the oxygen stoichiometry data, which will eventually affect the stability of crystal structure and electrical properties. As an example, SCF keeps approximately 40% of B^{+4} cations as initial state.[9] The SCF system orders when the average B-cation oxidation state is 3+, corresponding to an oxygen stoichiometry of 2.5. And the continuous temperature increase causes B^{3+} to be reduced to B^{2+} , resulting in an order–disorder transition above 1050 K. The coincidence with TPD (temperature programmed desorption) and

Thermogravimetric analysis (TGA) measurements for Co^{3+} and Co^{2+} reduction in similar materials suggest that the order–disorder transition in SCF is driven by the further reduction of Co. In contrast to SCF, the initial average oxidation state of B cations is less than 3+ within BSCF, which competes with the reduction of Co^{4+} to Co^{3+}. As for SCF, McIntosh *et al.* suggested that further reduction of oxygen stoichiometry occurs primarily through reduction of Co^{3+} to Co^{2+} as Fe^{3+} is more stable in the variances of temperature or pO_2.[9] This argument is consistent with the final B-cation oxidation state of BSCF of 2.1, which is an average value mixed with Co^{2+} and Fe^{3+}.[20]

Harvey *et al.* reported that the average oxidation state of Fe in $Ba_{0.5}Sr_{0.5}Co_{0.8}Fe_{0.2}O_{3-\delta}$ (BSCF5582) is near Fe^{+3} with some amount of Fe^{4+} according to the measurement of energy absorption in XANES analysis, in agreement with the Mossbauer results.[21] Harvey *et al.* also considered that more of Fe is 4+ than Co because the former is more stable than the latter in higher oxidation state, concluding that Fe is predominantly 3+ from 300K to 1233K, and Co is predominantly 3+ from 300 to 1073K, but reduced to 2+ at higher temperatures.[22]

Muller *et al.* reported that the dependencies on pO_2 of oxygen stoichiometries in Co and Fe are not the same according to XANES analysis vs. pO_2.[23] According to the modified band structure of BSCF1982, they suggested the following model: upon oxygen removal at high pO_2 (low Fermi level), Fe rather than Co accepts electrons. Upon further removal of oxygen at lower pO_2 (higher Fermi level), there are now fewer empty Fe states but more empty Co states available, and thus the additional electrons go predominantly into the Co band rather than into the Fe band, as shown in Figure 5. This results in a larger change of the formal oxidation number of Co than in that of Fe.[23]

As a MEIC, BSCF5582 is well known to transport a significant amount of oxygen anions via oxygen vacancies, with the oxygen self-diffusion coefficient and ionic conductivity to be on the order of 10^{-6} cm^2/s and 0.018 S/cm at 700°C.[24] The oxygen stoichiometry of BSCF5582 has been measured by several researchers with the reported values of 3-δ ranging from 2.2 to 2.8 depending on temperature, oxygen partial pressure, and method of measurement.[9,24-26] Chen *et al.* reported room-temperature 3-δ values ranging from 2.68 to 2.83 for BSCF with varying Co:Fe ratios.[18] McIntosh *et al.* reported oxygen stoichiometries (3-δ) of BSCF5582 ranging from 2.34 at 873 K and pO_2 = 1 atm

to 2.19 at 1173 K and $pO_2 = 10^{-3}$ atm and showed good agreement between data sets obtained from thermogravimetric analysis and Rietveld analysis of neutron data.[13] Svarcova *et al.* reported values of 2.42 at 1073K to 2.33 at 1273K for BSCF 5582 in air.[27] Using iodometry and thermogravimetry, Chen *et al.* reported room-temperature oxygen contents of 2.69 for BSCF5582 and 2.78 for BSCF5528 and values of 2.45-2.5 for the same range of compositions at 1173K.[18] Zeng *et al.* reported values of 2.7 at room temperature and values of 2.5 at 1173K[10]. Bucher *et al.* reported values of 2.45 to 2.55 for BSCF5582 in air at 1173K to 873K, respectively.[24]

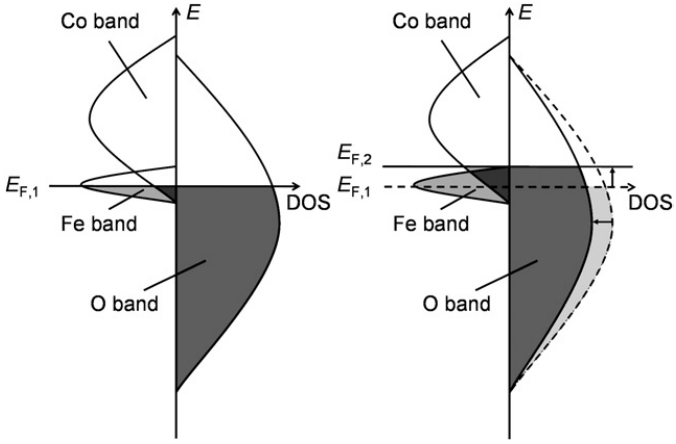

Figure 5. Schematic diagram of the band structure in BSCF1982 near the Fermi level for an arbitrarily chosen reference state (left) and after removal of oxygen (right). The arrows in the image on the right indicate the decrease in the number of oxygen states and the accompanying rise in the Fermi level upon reduction.[23] Copied under permission from RSC.

D. Electrical Properties of BSCF

The conductivity of MEICs depends simultaneously on electronic and ionic charge transport such that the total conductivity is expressed as $\sigma_t = \sigma_i + \sigma_e$. The overall room temperature electrical conductivity of BSCF5582 in air is on the order of 10 S/cm and increases with heating to temperatures of around 400°C. Above ~400°C, the conductivity levels off with further increases in temperature.[5,18] Electrical conduction, particularly from room temperature to 400°C, appears to be dominated by p-type carriers (electronic holes), presumably due to the incorporation of B^{3+} transition metal cations in

the $A^{2+}B^{4+}O_3$ parent compound.[28] The ratio of Co/Fe has a profound effect on the temperature-dependent electrical behavior of BSCF samples.[5,18] The A/B ratio[22,29] and the Sr/Ba ratio[30] affect the magnitude of the electrical conductivity, but do not dramatically change the temperature-dependent behavior.

The oxidation states of the Co and Fe cations, and possibly even the oxygen anions, strongly influence the transport properties of BSCF, but are not well understood. Several studies have suggested that mean valence of Co is lower than the mean valence of Fe.[5,22-23] The reduction of Fe^{4+} is often cited as the source of weight loss, changes in the electrical behavior, and anomalous thermal expansion upon heating above ~400^{o}C, which is generally accompanied by loss of oxygen.[5,19,31]

The cation valence state and oxygen non-stoichiometry are significantly influential on the conductivity, as well as on crystal structures. As has been mentioned, the reduction of the B-site cation gives rise to thermal expansion, which in turn affects conductivity. Al Daroukh *et al*. reported that, in the generic conductive perovskite structures, the logarithm of the ionic conductivity is linearly proportional to thermal expansion, as shown in Equation (2),[32]

$$\sigma_O = -7.08 + 2.9\times10^5 TEC \tag{2}$$

where, σ_O and TEC are expressed in S/cm and $10^{-6}K^{-1}$, respectively, for dimensions. Bucher *et al*. also suggested that the increase of oxygen vacancy concentration can improve oxygen ionic conductivity within the perovskite structure of BSCF according to the Nernst–Einstein equation of Equation (3),[24]

$$\sigma_{ion} = \frac{4F^2\left[V_o^{\bullet\bullet}\right]D_v}{RTV_m} \tag{3}$$

where, V_m is the perovskite molar volume, $[V_o^{\bullet\bullet}]$ is oxygen concentration, and D_v is the oxygen vacancy diffusivity.

But, the oxide ion conductivity depends strongly on the composition, even when the oxygen vacancy population is held constant according to Molecular Dynamics (MD) simulations on $BaCoO_{2.5}$ doped with Fe^{3+}.[33] C.A.J. Fisher *et al.* also reported that substituting Sr for Ba was shown to increase the ionic conductivity of $Ba_{1-x}Sr_xCo_{1-y}Fe_yO_{2.5}$, with the highest ionic conductivity in $SrFeO_{2.5}$, on the assumption that oxygen vacancies tend to cluster around Sr and Co ions when they calculated the numbers of oxygen coordination around each cation species.[33] This implies that the geometric increase of unit cell itself accompanied by oxygen vacancy formation could contribute to neither ionic nor electronic conductivity.

Chen *et al.* reported that the increase of iron concentration in $Ba_{0.5}Sr_{0.5}Co_xFe_{1-x}O_{3-\delta}$ membranes resulted in the decrease of electrical conductivity and influenced the decrease of the oxygen bulk diffusion rate, showing a sharp decrease in the permeation flux with the increase of iron concentration from $x = 0.6$ to 0.8,[18,34] even though TEC increases with increasing iron content in BSCF. Wei *et al.* reported that lattice constant increased accompanied by decreasing conductivity, with increasing Ba doping content in $Ba_xSr_{1-x}Co_{0.8}Fe_{0.2}O_{3-\delta}$ ($0.3 \leq x \leq 0.7$) perovskite oxides indicating that the thermal expansion coefficient (TEC) values and electrical conductivity follows the opposite behavior.[31]

Therefore, on the basis that conductivity can consist of ionic, *p*-type and *n*-type conductors in a material system, it is necessary to investigate the conduction mechanisms in various aspects. Originally introduced as an oxygen separation membrane,[16] BSCF is a MEIC deriving its high oxygen ion conductivity from its oxygen-deficient perovskite structure.

Bucher *et al.* reported the oxygen self-diffusion coefficient and ionic conductivity of BSCF5582 at 700°C to be $10^{-6}cm^2/s$ and $0.018Scm^{-1}$, respectively, which can be converted to $\sim 2.5 \times 10^{-5}cm^2/sec$ of oxygen ionic mobility and $2.22 \times 10^{18}cm^{-3}$ of ionic carrier concentration.[24] It is comparable with 3.8×10^{-2} cm^2/sec of hole mobility and $1.88 \times 10^{18}cm^{-3}$ of hole charge carrier concentration from our measurement. So, the transference number of ionic conductivity (σ_i) is $10^{-2} \sim 10^{-3}$ of the whole conductivity (σ_t) of BSCF5582, $\sim 30Scm^{-1}$, above 400°C. L. Ge *et al.* and P. Zeng *et al.* have reported that

the oxygen vacancy formed by the valence change of the A-site or B-site cations improves oxygen membrane capability in BSCF ceramics.[10,29]

As a MEIC, BSCF has relatively large oxygen vacancy concentration, around 3-δ = 2.54 at 700°C in air. Accordingly, the valence of the B-site cation will be easily changeable as it loses oxygen and may significantly affect the conductivity in BSCF as temperature or pO_2 changes.[18,24,35]

BSCF exhibits moderately high electronic conductivity owing to the mixed valence states of the transition metal B-site cations. As an example, the electrical conductivity of BSCF5582 in air above 500°C is reported to be ~ 30 S/cm.[10] However, the conductivity of BSCF5582 is over an order of magnitude lower than $La_{0.8}Sr_{0.2}Co_{0.8}Fe_{0.2}O_3$ (LSCF8282), a related perovskite oxide used as a SOFC cathode.[36] Unlike LSCF, BSCF does not possess a trivalent donor dopant on the A site of the perovskite structure.

The defect chemistry of $Ba_ySr_{1-y}Co_xFe_{1-x}O_{3-\delta}$ (BSCF) is not well understood as there have been few reports on the effect of composition and partial oxygen pressure on its electrical conductivity. Grunbaum *et al.* investigated the electrical conductivity of $SrCo_{0.8}Fe_{0.2}O_{3-\delta}$ as a function of temperature and pO_2, reporting an activation energy of 0.17eV for the Brownmillerite phase below 1000K, and an activation energy of ~0.34eV for the cubic phase above 1000 K.[37] In an investigation of compositions with x = 0.8, $0.3 \leq y \leq 0.7$, Wei *et al.* showed that conductivity decreases with increasing barium content in air at 773 – 1023K.[31] Chen *et al.* showed an increase in conductivity with increasing cobalt concentration in air and in oxygen above 773K for samples with y = 0.5, $0 \leq x \leq 0.8$.[18] More recent investigations of Ge *et al.* and Zhou *et al.* showed that the electrical conductivity decreases as the ratio of A/B deviates from unity.[29-30,38-39] A more detailed discussion about electrical studies for BSCF conducted as a part of this project will be presented in Chapter IV and Chapter V.

E. References

1. Z. Shao and S. Haile, "A High-Performance Cathode for the Next Generation of Solid-Oxide Fuel Cells," *Nature*, **431** [7005] 170-3 (2004).

2. L. Tan, X. Gu, L. Yang, W. Jin, L. Zhang, and N. Xu, "Influence of Powder Synthesis Methods on Microstructure and Oxygen Permeation Performance of $Ba_{0.5}Sr_{0.5}Co_{0.8}Fe_{0.2}O_{3-D}$ Perovskite-Type Membranes," *J. Membr. Sci.,* **212** [1-2] 157-65 (2003).

3. L. Tan, X. Gu, L. Yang, L. Zhang, C. Wang, and N. Xu, "Influence of Sintering Condition on Crystal Structure, Microstructure, and Oxygen Permeability of Perovskite-Related Type $Ba_{0.8}Sr_{0.2}Co_{0.8}Fe_{0.2}O_{3-d}$ Membranes," *Sep. Purif. Technol.,* **32** [1-3] 307-12 (2003).

4. H. Wang, W. Yang, Y. Cong, X. Zhu, and Y. Lin, "Structure and Oxygen Permeability of a Dual-Phase Membrane," *J. Membr. Sci.,* **224** [1-2] 107-15 (2003).

5. J. Jung, S. Misture, and D. Edwards, "The Electronic Conductivity of $Ba_{0.5}Sr_{0.5}Co_xFe_{1-x}O_{3-\delta}$ (BSCF: X= 0 1.0) under Different Oxygen Partial Pressures," *J. Electroceram.,* **24** [4] 261-9 (2009).

6. R. Vasquez, M. Siegal, D. Overmyer, Z. Ren, J. Lao, and J. Wang, "Chemical Bonding in Tl Cuprates Studied by X-Ray Photoemission," *Phys. Rev. B: Condens. Matter Mater. Phys.,* **60** [6] 4309-19 (1999).

7. B. Liu, Y. Zhang, and L. Tang, "X-Ray Photoelectron Spectroscopic Studies of $Ba_{0.5}Sr_{0.5}Co_{0.8}Fe_{0.2}O_{3-\Delta}$ Cathode for Solid Oxide Fuel Cells," *Int. J. Hydrogen Energy,* **34** [1] 435-9 (2009).

8. R. Shannon, "Revised Effective Ionic Radii and Systematic Studies of Interatomic Distances in Halides and Chalcogenides," *Acta Crystallogr., Sect. A: Cryst. Phys., Diffr., Theor. Gen. Crystallogr.,* **32** [5] 751-67 (1976).

9. S. McIntosh, J. Vente, W. Haije, D. Blank, and H. Bouwmeester, "Structure and Oxygen Stoichiometry of $SrCo_{0.8}Fe_{0.2}O_{3-\delta}$ and $Ba_{0.5}Sr_{0.5}Co_{0.8}Fe_{0.2}O_{3-\Delta}$," *Solid State Ionics,* **177** [19-25] 1737-42 (2006).

10. P. Zeng, Z. Chen, W. Zhou, H. Gu, Z. Shao, and S. Liu, "Re-Evaluation of $Ba_{0.5}Sr_{0.5}Co_{0.8}Fe_{0.2}O_{3-\Delta}$ Perovskite as Oxygen Semi-Permeable Membrane," *J. Membr. Sci.,* **291** [1-2] 148-56 (2007).

11. J. I. Jung, S. T. Misture, and D. D. Edwards, "Oxygen Stoichiometry, Electrical Conductivity, and Thermopower Measurements of $Ba_{0.5}Sr_{0.5}Co_xFe_{1-x}O_{3-\delta}$ (BSCF : X = 0 ~ 0.8) in Air," Solid State Ionics, 2010 (submitted for publication).

12. J. M. Gonzalez-Calbet, M. Parras, M. Vallet-Regi, and J. C. Grenier, "Nonstoichiometry in $BaFeO_{3-Y}$ (0.35 < Y < 0.50)," *J. Solid State Chem.,* **86** [2] 149-59 (1990).

13. S. McIntosh, J. Vente, W. Haije, D. Blank, and H. Bouwmeester, "Oxygen Stoichiometry and Chemical Expansion of $Ba_{0.5}Sr_{0.5}Co_{0.8}Fe_{0.2}O_{3-D}$ Measured by in Situ Neutron Diffraction," *Chem. Mater.*, **18** [8] 2187-93 (2006).

14. S. McIntosh, J. F. Vente, W. G. Haije, D. H. A. Blank, and H. J. M. Bouwmeester, "Phase Stability and Oxygen Non-Stoichiometry of $SrCo_{0.8}Fe_{0.2}O_{3-\delta}$ Measured by in Situ Neutron Diffraction," *Solid State Ionics*, **177** [9-10] 833-42 (2006).

15. P. Hendriksen, P. Larsen, M. Mogensen, F. Poulsen, and K. Wiik, "Prospects and Problems of Dense Oxygen Permeable Membranes," *Catal. Today*, **56** [1-3] 283-95 (2000).

16. Z. Shao, W. Yang, Y. Cong, H. Dong, J. Tong, and G. Xiong, "Investigation of the Permeation Behavior and Stability of a $Ba_{0.5}Sr_{0.5}Co_{0.8}Fe_{0.2}O_{3-\Delta}$ Oxygen Membrane," *J. Membr. Sci.*, **172** [1-2] 177-88 (2000).

17. G. C. Kostogloudis, P. Fertis, and C. Ftikos, "The Perovskite Oxide System $Pr_{1-x}Sr_xCo_{1-y}Mn_yO_{3-\delta}$: Crystal Structure and Thermal Expansion," *J. Eur. Ceram. Soc.*, **18** [14] 2209-15 (1998).

18. Z. Chen, R. Ran, W. Zhou, Z. Shao, and S. Liu, "Assessment of $Ba_{0.5}Sr_{0.5}Co_{1-y}Fe_yO_{3-\delta}$ (Y = 0.0-1.0) for Prospective Application as Cathode for IT-SOFCs or Oxygen Permeating Membrane," *Electrochim. Acta*, **52** [25] 7343-51 (2007).

19. Q. Zhu, T. Jin, and Y. Wang, "Thermal Expansion Behavior and Chemical Compatibility of $Ba_xSr_{1-x}Co_{1-y}Fe_yO_{3-\Delta}$ with 8YSZ and 20GDC," *Solid State Ionics*, **177** [13-14] 1199-204 (2006).

20. H. Hayashi, H. Inaba, M. Matsuyama, N. G. Lan, M. Dokiya, and H. Tagawa, "Structural Consideration on the Ionic Conductivity of Perovskite-Type Oxides," *Solid State Ionics*, **122** [1-4] 1-15 (1999).

21. M. Wilke, G. Partzsch, R. Bernhardt, and D. Lattard, "Determination of the Iron Oxidation State in Basaltic Glasses Using Xanes at the K-Edge," *Chem. Geol.*, **220** [1-2] 143-61 (2005).

22. A. S. Harvey, F. J. Litterst, Z. Yang, J. L. M. Rupp, A. Infortuna, and L. J. Gauckler, "Oxidation States of Co and Fe in $Ba_{1-x}Sr_xCo_{1-y}Fe_yO_{3-d}$ (X,Y = 0.2-0.8) and Oxygen Desorption in the Temperature Range 300-1273k," *Phys. Chem. Chem. Phys.*, **11** [17] 3090-8 (2009).

23. D. Müller, J. Brendt, D. Samuelis, and M. Martin, "Oxidation States of the Transition Metal Cations in the Highly Nonstoichiometric Perovskite-Type Oxide $Ba_{0.1}Sr_{0.9}Co_{0.8}Fe_{0.2}O_3$," *J. Mater. Chem.*, **19** [14] 1960-3 (2009).

24. E. Bucher, A. Egger, P. Ried, W. Sitte, and P. Holtappels, "Oxygen Nonstoichiometry and Exchange Kinetics of $Ba_{0.5}Sr_{0.5}Co_{0.8}Fe_{0.2}O_{3-\Delta}$," *Solid State Ionics,* **179** [21-26] 1032-5 (2008).

25. E. Girdauskaite, H. Ullmann, M. Al Daroukh, V. Vashook, M. Bülow, and U. Guth, "Oxygen Stoichiometry, Unit Cell Volume, and Thermodynamic Quantities of Perovskite-Type Oxides," *J. Solid State Electrochem.,* **11** [4] 469-77 (2007).

26. H. Wang, Y. Cong, and W. Yang, "Oxygen Permeation Study in a Tubular $Ba_{0.5}Sr_{0.5}Co_{0.8}Fe_{0.2}O_{3-\Delta}$ Oxygen Permeable Membrane," *J. Membr. Sci,* **210** [2] 259-71 (2002).

27. S. Švarcová, K. Wiik, J. Tolchard, H. Bouwmeester, and T. Grande, "Structural Instability of Cubic Perovskite $Ba_xSr_{1-x}Co_{1-y}Fe_yO_3$," *Solid State Ionics,* **178** [35-36] 1787-91 (2008).

28. S. Misture, "Large-Volume Atmosphere-Controlled High-Temperature X-Ray Diffraction Furnace," *Meas. Sci. Technol.,* **14** [7] 1091-8 (2003).

29. L. Ge, W. Zhou, R. Ran, S. Liu, Z. Shao, W. Jin, and N. Xu, "Properties and Performance of a-Site Deficient $(Ba_{0.5}Sr_{0.5})_{1-x}Co_{0.8}Fe_{0.2}O_{3-\delta}$ for Oxygen Permeating Membrane," *J. Membr. Sci.,* **306** [1-2] 318-28 (2007).

30. L. Ge, R. Ran, K. Zhang, S. Liu, and Z. Shao, "Oxygen Selective Membranes Based on B-Site Cation-Deficient $(Ba_{0.5}Sr_{0.5})(Co_{0.8}Fe_{0.2})_yO_{3-\delta}$ Perovskite with Improved Operational Stability," *J. Membr. Sci.,* **318** [1-2] 182-90 (2008).

31. B. Wei, Z. Lü, X. Huang, J. Miao, X. Sha, X. Xin, and W. Su, "Crystal Structure, Thermal Expansion and Electrical Conductivity of Perovskite Oxides $Ba_xSr_{1-x}Co_{0.8}Fe_{0.2}O_{3-\delta}(0.3 \le x \le 0.7)$," *J. Eur. Ceram. Soc.,* **26** [13] 2827-32 (2006).

32. M. Al Daroukh, V. Vashook, H. Ullmann, F. Tietz, and I. Arual Raj, "Oxides of the AMO_3 and A_2MO_4 Type: Structural Stability, Electrical Conductivity and Thermal Expansion," *Solid State Ionics,* **158** [1-2] 141-50 (2003).

33. C. A. J. Fisher, M. Yoshiya, Y. Iwamoto, J. Ishii, M. Asanuma, and K. Yabuta, "Oxide Ion Diffusion in Perovskite-Structured $Ba_{1-x}Sr_xCo_{1-y}Fe_yO_{2.5}$: A Molecular Dynamics Study," *Solid State Ionics,* **177** [39-40] 3425-31 (2007).

34. S. Lee, Y. Lim, E. A. Lee, H. J. Hwang, and J.-W. Moon, "$Ba_{0.5}Sr_{0.5}Co_{0.8}Fe_{0.2}O_{3-\Delta}$ (BSCF) and $La_{0.6}Ba_{0.4}Co_{0.2}Fe_{0.8}O_{3-\delta}$ (LBCF) Cathodes Prepared by Combined Citrate-EDTA Method for IT-SOFCs," *J. Power Sources,* **157** [2] 848-54 (2006).

35. A. Mineshige, M. Inaba, T. Yao, Z. Ogumi, K. Kikuchi, and M. Kawase, "Crystal Structure and Metal-Insulator Transition of $La_{1-x}Sr_xCoO_3$," *J. Solid State Chem.,* **121** [2] 423-9 (1996).

36. L. W. Tai, M. M. Nasrallah, H. U. Anderson, D. M. Sparlin, and S. R. Sehlin, "Structure and Electrical Properties of $La_{1-x}Sr_xCo_{1-y}Fe_yO_3$. Part 1. The System $La_{0.8}Sr_{0.2}Co_{1-y}Fe_yO_3$," *Solid State Ionics*, **76** [3-4] 259-71 (1995).

37. N. Grunbaum, L. Mogni, F. Prado, and A. Caneiro, "Phase Equilibrium and Electrical Conductivity of $SrCo_{0.8}Fe_{0.2}O_{3-\delta}$," *J. Solid State Chem.*, **177** [7] 2350-7 (2004).

38. J. Ovenstone, J. Jung, J. White, D. Edwards, and S. Misture, "Phase Stability of BSCF in Low Oxygen Partial Pressures," *J. Solid State Chem.*, **181** [3] 576-86 (2008).

39. W. Zhou, R. Ran, Z. Shao, W. Zhuang, J. Jia, H. Gu, W. Jin, and N. Xu, "Barium- and Strontium-Enriched $(Ba_{0.5}Sr_{0.5})_{1+x}Co_{0.8}Fe_{0.2}O_{3-\delta}$ Oxides as High-Performance Cathodes for Intermediate-Temperature Solid-Oxide Fuel Cells," *Acta Mater.*, **56** [12] 2687-98 (2008).

III. EXPERIMENTAL PROCEDURES

A. Powder Synthesis

The experimental procedure for making powders and samples has been plotted in Figure 6. Laboratory prepared powders were synthesized using a modified Pechini method, using $Ba(NO_3)_2$, $Sr(NO_3)_2$, $Co(NO_3)_2 \cdot 6H_2O$, and $Fe(NO_3)_3 \cdot 9H_2O$ as starting materials. 0.04 mol of ethylenediaminetetraacetic acid (EDTA) was mixed with 40 ml of 1N NH_4OH solution to make NH_3-EDTA buffer solution. 0.01 mol of $Ba(NO_3)_2$, 0.01 mol of $Sr(NO_3)_2$, and x(0.02, , 0.16, 0.12, 0.08, 0.04, 0) mol of $Co(NO_3)_2 \cdot 6H_2O$ and (0.02-x) mol of $Fe(NO_3)_3 \cdot 9H_2O$, were added to the buffer solution in order to make the required stoichiometries of $Ba_{0.5}Sr_{0.5}Co_xFe_{1-x}O_{3-\delta}$ (x = 1.0, 0.8, 0.6, 0.4, 0.2, 0.0). 0.06 mol of anhydrous citric acid was added and the pH value was adjusted to 8 by using 1N NH_4OH solution. Each solution was kept on a hot plate at 100°C and stirred until gelation took place. After 24 hours, the gelled samples were baked in a drying oven at 200°C for 6hr. The as-produced powders were then calcined at 950°C for 8 hours in air.

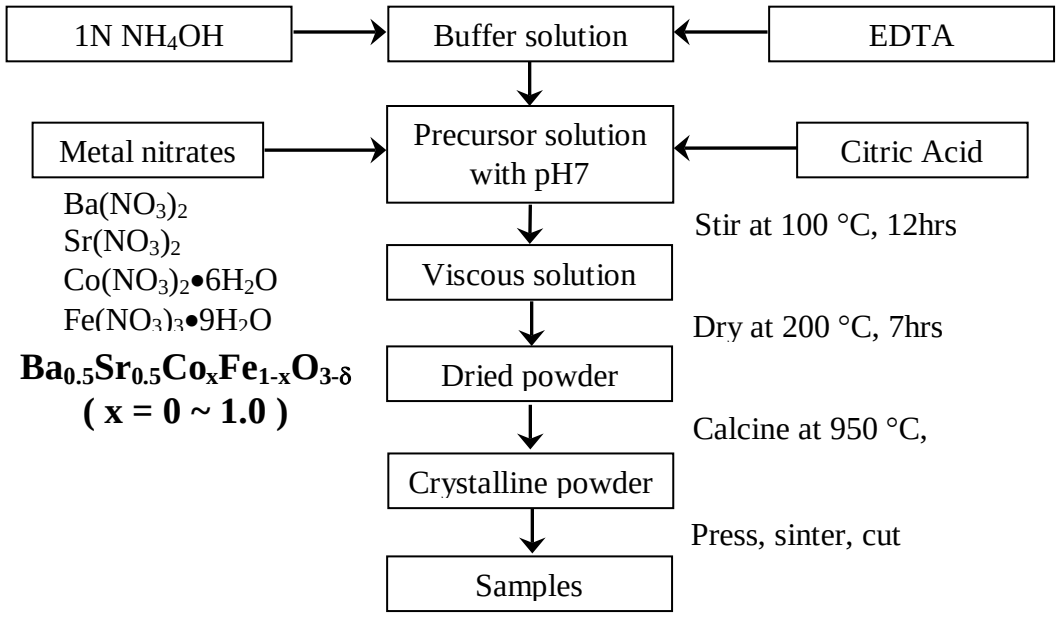

Figure 6. The plot of experimental procedure for making powders and samples.

B. Sintering

To prepare samples suitable for electrical measurements, the synthesized powders were pressed into pellets at 100MPa, and then were cold-isostatically pressed at 150MPa. The samples were sintered at 1100°C for 4hr in air at a heating rate of 4 K/min and cooled at the natural cooling rate of the furnace. X-ray fluorescence spectroscopy was conducted on sintered pellets to determine the resulting cation ratios.[1] All samples were B-site deficient with A/B ratio of ~ 1.1 for all compositions. The Co/Fe ratios were slightly higher than formulated, with x = 0.22, 0.42, 0.62, and 0.82. One of the suppositions for the stoichiometric deviation from designed formula is that each starting nitrate material has different hydration stability when it is open to air.

C. Density Measurement

The relative bulk density of each sample was measured using Archimedes' method. After being dried at 120°C for two days within an oven chamber, the weight of a sample (W_1) was recorded. After the sample was boiled in distilled water at 300°C for 5hrs, weighing was conducted as the sample was immersed within distilled water (W_3), and then, after wiping off the surface of the sample, W_2 was weighed in the air. The bulk density (d_b) was obtained as $d_b = W_1/(W_2 - W_3)$.

D. X-ray Diffraction

The crystal structure and phase purity of the synthesized powders were confirmed using X-ray diffraction, using a Siemens D5000 diffractometer using Cu-Kα radiation, a scan range of 15° to 80°, a step size of 0.02°, and a counting time of 5s. Lattice parameters were determined using a least-squares method.

E. SEM

SEM was carried out using an FEI Quanta 200F field emission environmental SEM equipped with a hot stage, backscatter detector, and EDX detector. The grain size of microstructure on the fractured samples was measured by line-intercept method.[2]

F. TGA

To determine the oxygen content as a function of temperature, thermogravimetric analysis of the calcined BSCF powders was conducted from room temperature to 900^{o}C by heating the sample in 100 K increments at 5 K/min, and holding at each step for 20 minutes after which no further weight loss was observed. The analysis was conducted using a STA449C Jupiter system (Netzsch, USA) in air.

G. Oxygen Stoichiometry Measurements

The room-temperature oxygen content of the powders was determined using iodometric titration, following the method reported by Fujihara.[3-4] After a 40mg portion of powder was weighed in a round-necked glass vessel, 1g of potassium iodide (KI) and 10mL of 6N HCl (hydrochloric acid) were added, and then the vessel was closed and heated until the sample dissolved. After dissolution, the solution was flushed with Ar to avoid air-oxidation of excess I^{-}. The solution was titrated with 0.025N of sodium thiosulfate ($Na_2S_2O_3$) solution, using starch as an indicator. This analysis assumes that trivalent and tetravalent transition metal cations are reduced to their divalent state according to the following reactions:

$$2B^{3+} + 3I^{-} \rightarrow 2B^{2+} + I_3^{-}; \quad B^{4+} + 3I^{-} \rightarrow B^{2+} + I_3^{-}$$

Titration of sodium thiosulfate ($Na_2S_2O_3$) with a starch indicator allows for the determination of liberated iodine, I_3^{-}, according to

$$2S_2O_3^{2-} + I_3^{-} \rightarrow S_4O_6^{2-} + 3I^{-}$$

Assuming that all of the Co and Fe was reduced to its divalent state, the mean valence of B^{2+p} (B = Co, Fe) in $(Ba_{0.5}Sr_{0.5})_A(Co_xFe_{1-x})_BO_{3-\delta}$ was calculated according to the following equation.[5]

$$p = \frac{(M - M_o)CV}{W_s - M_oCV}$$

where, M is the molecular weight of BSCF, M_O is the atomic weight of oxygen, C is the concentration of $Na_2S_2O_3$ standard solution, W_S is the weight of sample and V is the volume of $Na_2S_2O_3$ standard solution used for titration. The oxygen deficiency, δ, was calculated from the equation, $\delta = (2-p)/2$. Iodometric titration of Fe_2O_3 as conducted to assess the accuracy of the technique and suggested an oxygen stoichiometry of 3.1, suggesting ~3% accuracy for the technique.

To determine the oxygen content as a function of temperature, thermogravimetric analysis of the calcined BSCF powders was conducted from room temperature to 900^{o}C by heating the sample in 100 K increments at 5 K/min, and holding at each step for 20 minutes, after which no further weight loss was observed. The analysis was conducted using a STA449C Jupitor system (Netzsch, USA).

H. Electrical Measurements and Data Analysis

For four-point electrical and thermopower measurement, sintered pellets were cut into rectangular shapes of 3mm×4mm×12mm (a × b × L). Two small grooves (0.01inch of width) were cut into the sample surface at ¼ and ¾ of the length (L) of bars to prevent slippage of the inner platinum wires connected to the volt meter.

For four-point probe DC measurement, platinum paste was painted on the cross sectional faces of the sample to form current electrodes. Platinum paste-painted samples were heated at 900°C for 15min to cure the electrodes. The electrical conductivity was measured by the four-point DC method on the rectangular test bars. For conductivity measurements, ~100mA of current was passed through the outer electrodes, and the voltage drop was measured across the inner electrodes. The measurements were performed in the air upon heating from 200 to 1000°C at steps of 100 K. At each temperature step, 10min was allowed for the conductivity stabilization. Conductivity, σ, was calculated as Equation (4),

$$\sigma = \frac{I}{V}\frac{\ell}{A} \tag{4}$$

where, I is current (~100 mA), *V* voltage drop, *l* the inner electrode spacing, and A (a × b) the cross-sectional area of the bar.

Electrical conductivity was measured using a Labview controlled system consisting of a programmable current source (Model JQE 55-2M, Kepco Powder Supply, USA), a voltage meter (Model 2000 Digital Multimeter, Keithley Instruments, USA), a current meter (Model 2000 Digital Multimeter, Keithley Instruments, USA), and a chamber furnace (Model Ney Centurion Qex, USA). Oxygen partial pressure was measured with oxygen analyzer (Model Thermox CG1000, AMETEK, USA) on the outlet of chamber furnace.

In subsequent experiments, DC conductivity and Seebeck coefficient were simultaneously measured vs. T in air. And additional thermopower measurements were conducted vs.pO_2 as pO_2 increases from 10^{-5} to 1 atm at 500°C, 700°C and 900°C using a Labview controlled system consisting of a programmable current source (Model 2400 Sourcemeter, Keithley Instruments, USA), a voltage/current meter (Model 2700 Multimeter/DATA AC*Q*UISTION, Keithley Instruments, USA), and a tube furnace (Model 21100 Tube furnace, Thermolyne, USA). Oxygen partial pressures were measured using an oxygen analyzer (Model Thermox CG1000, AMETEK, USA) on the outlet of chamber furnace.

A bar-shaped sample was mechanically compressed between two outer (current) electrodes attached to two other R-type thermocouples (Pt-13% Rh/Pt, 0.01 inch diameter). Gold foil (0.01 inch thick) was used for outer electrodes. Two inner electrodes consisting of R-type thermocouples were held in contact with the sample by means of gold wire (0.01 inch diameter) wrapped around the sample.

Electrical measurements were recorded at each temperature after equilibrium was achieved as judged by observing conductivity as function of time. To correct for the thermopower contributions, an average conductivity was calculated from measurement collected in forward and reverse directions. Thermopower was measured using the 'steady state straddle' method. The sample was placed in the natural temperature gradient of the furnace to provide 10~20 K gradient along the length of the sample. Temperatures were measured at each thermocouple contact (T_1, T_2, T_3, T_4), and voltage was measured across the platinum legs of the six thermocouple combinations (V_1-V_2, V_1-

V_3, V_1-V4, V_2-V_3, V_2-V_4, and V_3-V_4). Thermoelectric coefficients are obtained by measuring the voltage drop for the temperature gradient along the sample length. The thermoelectric coefficient, or Seebeck coefficient, *Q* is defined as Equation (5)

$$Q = \lim_{\Delta T \to 0} \frac{\Delta V}{\Delta T} \tag{5}$$

To account for contributions from the platinum electrodes, the measured coefficient was corrected as Equation (6)

$$Q_s = Q_m + Q_{pt} = Q_m - 0.01435\,T(°C) - 7.377 \tag{6}$$

where, Q_s is the corrected coefficient, Q_m is the measured coefficient, Q_{pt} is thermoelectric coefficient of platinum, and T is temperature °C.[6]

Figure 7 shows the diagram of measurement comparison between DC 4pt technique and thermopower method.

When *p*-type conduction is dominant, as shown in Equation (7), the ideal slope of charge carrier concentration vs. pO_2 is ¼, on the assumption that oxygen vacancy itself does not affect conduction.[7]

$$O_O + 2h^{\bullet} = \frac{1}{2}O_2(g) + V_O^{\bullet\bullet}$$

$$K = \frac{\left[V_O^{\bullet\bullet}\right] pO_2^{1/2}}{p^2}$$

$$p = \left(\frac{1}{K}\right)^{1/2} \left[V_O^{\bullet\bullet}\right]^{1/2} pO_2^{1/4}$$

$$\ln p \propto \frac{1}{4} \ln pO_2 \tag{7}$$

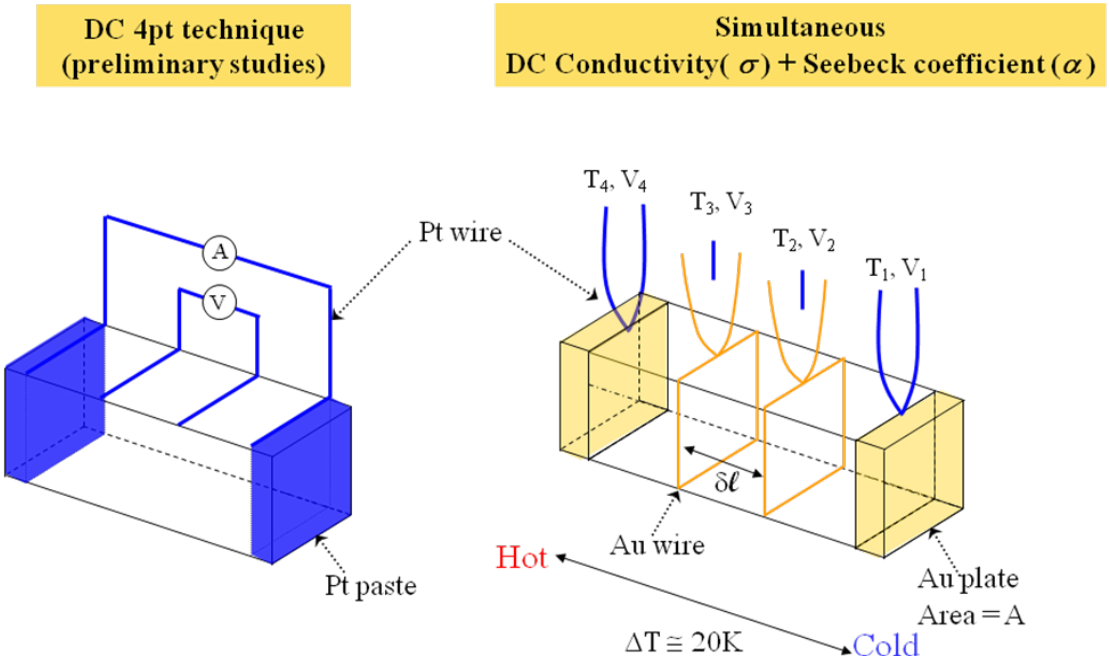

Figure 7. Comparison of two techniques used to measure electrical properties i) conductivity vs. T in different pO_2 and ii) Seebeck coefficient and conductivity vs pO_2 at different temperatures.

The Jonker plot in Equation (8) was used to interpret curves of Seebeck coefficient(α) as a function of log(α/α_i) for a number of values of (E_g/kT +2A).[8]

$$\alpha = \pm\frac{k}{2e}\left(\frac{E_g}{kT}+2A\right)\left(1-\frac{\sigma_i^2}{\sigma^2}\right)^{1/2} - \frac{k}{e}\ln\left[\frac{\sigma}{\sigma_i}\left\{1\pm\left(1-\frac{\sigma_i^2}{\sigma^2}\right)^{1/2}\right\}\right] \qquad (8)$$

where, σ_i denotes intrinsic conductivity and $\sigma = \sigma_+ + \sigma_-$. When the slope of α *vs.* LN(σ/σ_i) is ±86.17μV/K, the conductivity is wholly determined by *n*-type or *p*-type semiconductor conduction. When the conductivity and the Seebeck effect of a series of samples are studied separately, irregularity is expected as a result of deviations from the chemical composition, impurities, defects, etc, because both quantities depend on the actual concentrations of charge carriers. These irregularities disappear by plotting the

Seebeck coefficient as a function of log conductivity : e.g. when the slope deviates from the ideal, it is attributable to a slight contribution of impurity conduction.[8]

I. XPS Analysis

For XPS analysis, the sintered bulk samples were cleaved into neatly fractured surfaces by putting samples between sharp blades fastened to contrived jig and hammering slightly on the top plate of jig, as shown in Figure 8. The fastened blades fixed to plate are mobile just vertically enough to cut through intended spots of samples without moving horizontally. Single sample of individual condition has been prepared for measurement. The fractured samples are inserted into the XPS vacuum chamber within 5min in order to minimize atmosphere contamination. Samples were kept within vacuum chamber for 30hrs before measurements in order to pursue the ideal experimental condition. Before measurement, there was neither Ar nor ion cleansing process on the fracture surface, because there could be the risk of washing selective atoms away during cleansing.

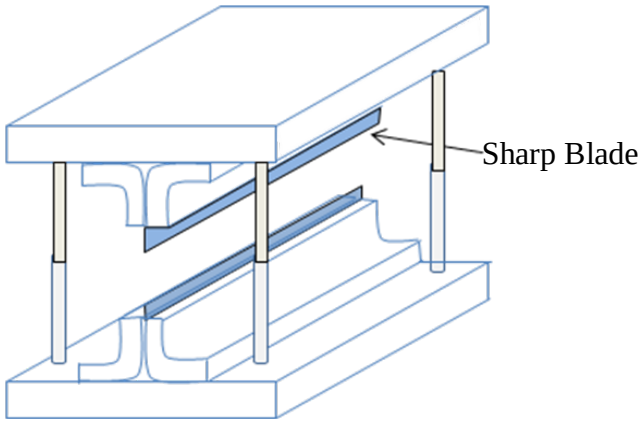

Figure 8. Schematic diagram of contrived jig for cleaving samples

The XPS measurements were performed on a PHI Quantera SXM™ (ULVAC-PHI. Inc, JAPAN) (base pressure 5×10^{-9}Pa) instrument using monochromatic Al Ka radiation (1486.6eV). The analyzer pass energy was set to 26eV for narrow scans, the step size of which was 0.05eV. The number of sweeps was 2 and the signal ratio to noise

was 50. The energy scale was calibrated using the Ag_{4d} peak positions. The spot size of beam on sample was ~100μm. The shifts in energy (charging) of the XPS spectra were corrected using the C_{1s} peak at 284.6eV as a reference peak.

DRIFT (Diffuse Reflectance Infrared Fourier Transformation) was measured for powder samples within the closed chamber of Nexus 670 FT-IR E.S.D.^{TM} (GMI Inc., USA) under the constant flow of 30ml dry air (≤ 10ppm of moisture) from R.T. to 700°C, by heating the sample in 100 K increments, and holding at each step for 20 minutes.

J. References

1. J. Jung, S. Misture, and D. Edwards, "The Electronic Conductivity of $Ba_{0.5}Sr_{0.5}Co_xFe_{1-x}O_{3-\delta}$ (BSCF: X= 0 1.0) under Different Oxygen Partial Pressures," *J. Electroceram.,* **24** [4] 261-9 (2009).

2. G. Vander Voort, "Grain Size Measurement," pp. 85-131 in *Practical Applications of Quantitative Metallography,* ASTM STP 839. Edited by J. L. McCall and J. J.H. Steele. American Society for Testing and Materials, Philadelphia, PA, 1984.

3. J. Ovenstone, J. S. White, and S. T. Misture, "Phase Transitions and Phase Decomposition of $La_{1-x}Sr_xCoO_{3-\Delta}$ in Low Oxygen Partial Pressures," *J. Power Sources,* **181** [1] 56-61 (2008).

4. S. Švarcová, K. Wiik, J. Tolchard, H. Bouwmeester, and T. Grande, "Structural Instability of Cubic Perovskite $Ba_xSr_{1-x}Co_{1-y}Fe_yO_3$," *Solid State Ionics,* **178** [35-36] 1787-91 (2008).

5. L. Rormark, A. B. Morch, K. Wiik, S. Stolen, and T. Grande, "Enthalpies of Oxidation of $CaMnO_{3-\delta}$, $Ca_2MnO_{4-\delta}$ and $SrMnO_{3-\delta}$ Deduced Redox Properties," *Chem. Mater.,* **13** [11] 4005-13 (2001).

6. L. Shen, P. Salvador, and T. Mason, "High Temperature Electrical Properties and Defect Chemistry of $La_{2-x}Ca_xCuO_{4-y}$ Superconductors--I. Electrical Properties," *J. Phys. Chem. Solids,* **57** [9] 1311-9 (1996).

7. *The Defect Chemistry of Metal Oxides*; p. 210. Edited by D. Smyth. Oxford University Press, New York, 2000.

8. G. Jonker, "The Application of Combined Conductivity and Seebeck-Effect Plots for the Analysis of Semiconductor Properties(Conductivity Vs Seebeck Coefficient Plots for Analyzing N-Type, P-Type and Mixed Conduction Semiconductors Transport Properties)," *Philips Res. Rep.,* **23,** 131-8 (1968).

IV. ELECTRICAL PROPERTIES OF BSCF UNDER DIFFERENT OXYGEN PARTIAL PRESSURES

A. Introduction

The electrical conductivity of sintered BSCF ceramics ($Ba_{0.5}Sr_{0.5}Co_xFe_{1-x}O_{3-\delta}$, $0 \leq x \leq 1$) were measured as a function of temperature from room temperature to 1273K. Additionally, the conductivity of one composition – BSCF5582 ($Ba_{0.5}Sr_{0.5}Co_{0.8}Fe_{0.2}O_{3-\delta}$) – was also measured as a function of oxygen partial pressure in the range $10^{-5} \leq pO_2 \leq 1$ atm, in which pO_2 was kept above $pO_2=10^{-5}$atm, because BSCF perovskite structure is unstable below $pO_2=10^{-5}$atm. At low temperatures, below ~ 673K, the electrical conductivity of all BSCF samples ($0 \leq x \leq 0.8$) in air is thermally activated ($0.21eV \leq E_a \leq 0.40eV$) and is dominated by p-type polaron hopping between B^{3+} and B^{4+} cations. The formation of oxygen vacancies above ~673K in air is accompanied by a decrease in p-type carrier concentration. Below ~673K, the electrical conductivity of BSCF5582 is thermally activated ($0.28eV \leq E_a \leq 0.35eV$) over the range $10^{-5} \leq pO_2 \leq 1$ atm. Above ~673K, BSCF5582 ($x = 0.8$) evidence for a p-to-n-type transition was observed, as pO_2 is reduced below ~ 0.01atm. The activation energy of the n-type conduction BSCF5582 is ~ 0.2eV. However, further experiments are necessary to explore the possibility of a *p-n* type.

B. Phase Stability as Preliminary Study

As preliminary work, the XRD analysis on phase stability was mainly executed by Dr. Ovenstone.[1] Figure 9 shows the X-ray data for BSCF5582 sample heated to 1000°C in 10^{-5}atm pO_2. Only peaks corresponding to the cubic perovskite structure are noted in the patterns, indicating that the material is stable over the range from 25°C to 1000°C under $pO_2 = 10^{-5}$atm. All the compositions of BSCF, $0 \leq x \leq 0.8$ retained their cubic symmetry up to 1000°C with no evidence of decomposition throughout the pO_2 range $10^{-5} < pO_2 < 10^{-1}$atm.

In BSC ($Ba_{0.5}Sr_{0.5}CoO_{3-\delta}$), a new phase transition was observed with a rhombohedral to cubic phase transition at ~800°C under $pO_2 = 10^{-5}$atm as shown in Figure 10. The high temperature cubic phase, which until now has not been reported, was retained upon cooling at 10°C/min to room temperature.

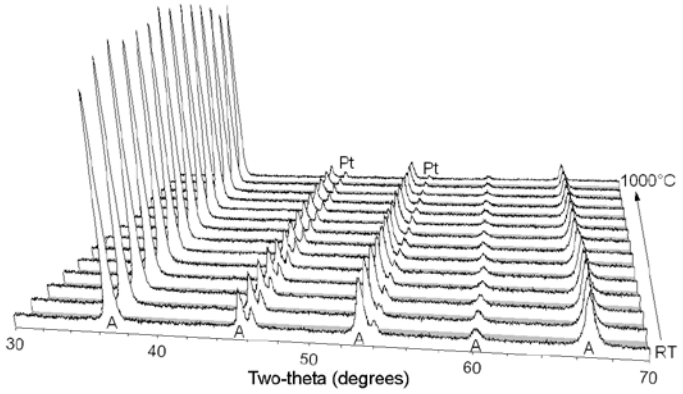

Figure 9. *In-situ* X-ray diffraction data for laboratory prepared $Ba_{0.5}Sr_{0.5}Co_{0.8}Fe_{0.2}O_{3-\delta}$ heated in 10^{-5} atm pO_2. A = cubic $Ba_{0.5}Sr_{0.5}Co_{0.8}Fe_{0.2}O_{3-\delta}$. Minor diffraction peaks from the Pt sample holder are present. The diffraction patterns were collected in 25 K steps, however are shown in 75 K steps for clarity.[1]

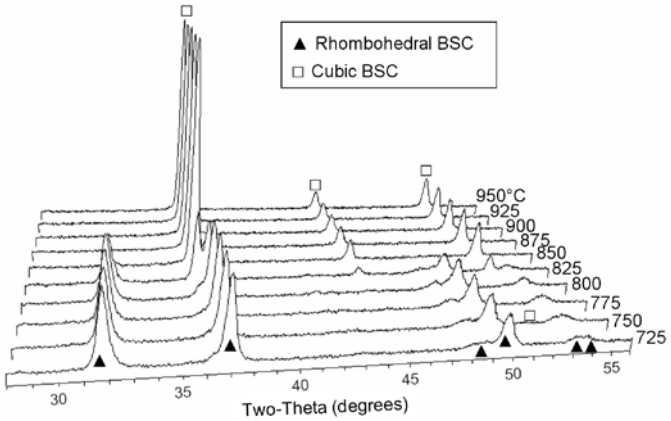

Figure 10. X-ray diffraction data for laboratory prepared BSC heated in 10^{-5} atm pO_2. A = rhombohedral BSC, and B = cubic BSC.[1]

Figure 11 shows the unit cell volume expansion, defined as $\Delta V/V_{RT}$, as a function of temperature for BSCF, $0.2 < x < 0.8$ under $pO_2 = 10^{-5}$atm. Refining the room-temperature data set demonstrated that the high temperature polymorph is a cubic perovskite, resulting in refinement statistics Rwp = 9.8% and GOF = 1.2. The unit cell details at room temperature are: a = 3.989(3)Å; and calculated density = 5.41(2)gcm^{-3}.

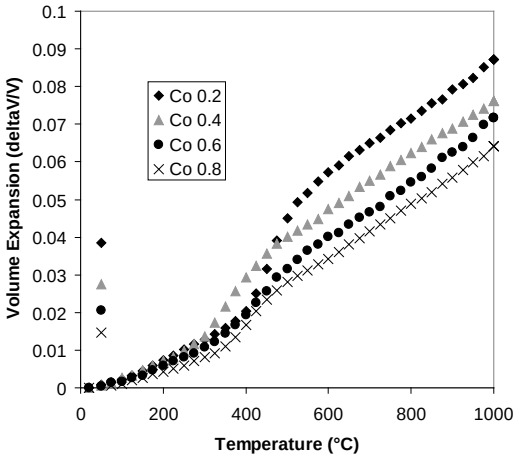

Figure 11. Lattice expansions for laboratory prepared $Ba_{0.5}Sr_{0.5}Co_xFe_{1-x}O_{3-\delta}$ heated in 10^{-5} atm pO_2 calculated from X-ray diffraction data. The data points at 50K are for the samples after cooling.

The thermal expansion coefficients are temperature dependent, but incremental thermal expansion coefficients can be obtained over limited temperature ranges. Between 300°C and 600°C, the samples show a marked increase in expansion as a result of equilibration of the oxygen vacancy concentration in the low pO_2 environment. Vacancy formation is accompanied by an anomalously large increase in unit cell volume, or chemical expansion and is attributed to the reduction of the B-site cations.

C. Results

Figure 12 shows x-ray diffraction patterns across the compositional range of the laboratory prepared BSCF ($Ba_{0.5}Sr_{0.5}Co_xFe_{1-x}O_{3-\delta}$, $0 \leq x \leq 1$) in air. BSF ($Ba_{0.5}Sr_{0.5}FeO_{3-\delta}$) and BSCF ($0.2 \leq x \leq 0.8$) were cubic perovskite, whereas the BSC ($Ba_{0.5}Sr_{0.5}CoO_{3-\delta}$) had a rhombohedral structure. With the increase of the cobalt concentration, there was an increase in the unit cell volume of the material, shown by the shift of 2-θ to low angles in

Figure 12. A comparison of the ionic radii of iron and cobalt in different valent states (r_{Fe4+} = 0.585Å , $r_{Co4+(HS)}$ = 0.53Å, $r_{Fe3+(HS)}$ = 0.64Å , $r_{Co3+(HS)}$ = 0.61Å, $r_{Co2+(HS)}$ = 0.75Å, $r_{Co2+(HS)}$ = 0.78Å, all CN = 6)[2] suggests that cobalt is incorporated in a lower valence state than iron as was suggested in our previous paper.[1]

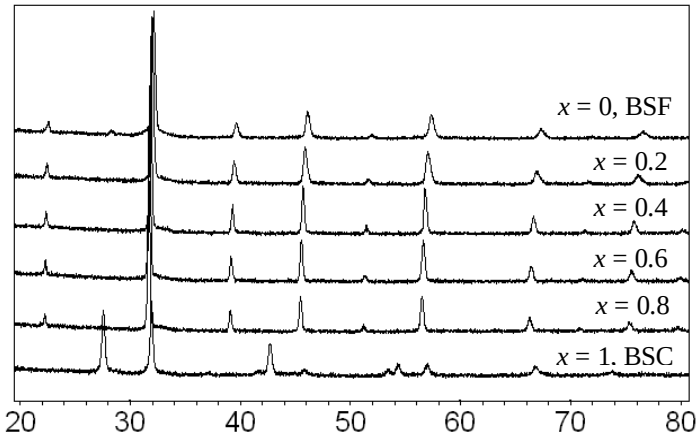

Figure 12. Room temperature X-ray diffraction data for $Ba_{0.5}Sr_{0.5}Co_xFe_{1-x}O_{3-\delta}$ (x = 0 ~ 1.0) calcined at 950°C in air.

Table I summarizes the composition of the samples as measured by X-ray fluorescence spectroscopy. The data suggest that all samples were B-site deficient with an A/B ratio of ~1.1 for all values of x. In all samples the major impurity was aluminum at ~0.3% on a cation basis.

Figure 13 shows the microstructure of BSCF samples sintered in the air. The BSC and BSCF samples were ~90% of their theoretical densities whereas the BSF sample was ~65% of its theoretical density, as shown in Table I. With increasing cobalt concentration, an increase in both grain size and pore size was observed. The increase in grain size with increasing x is attributed to an increase in diffusional mass transport via oxygen vacancies.

Table I. Lattice Parameters, Relative Density, Mean Grain Size and Mean Pore Size of $Ba_{0.5}Sr_{0.5}Co_xFe_{1-x}O_{3-\delta}$

Sample	Lattice Parameters			Relative density (%)	Mean grain size (μm)	Mean pore size (μm)
	a(Å)	**c(Å)**	**γ (°)**			
x = 0	3.931(38)	3.931(38)	90	65.5	2.7 ± 1.2	1.5 ± 1.3
x = 0.2	3.951(34)	3.951(34)	90	91.1	5.5 ± 3.3	2.6 ± 1.8
x = 0.4	3.967(14)	3.967(14)	90	97.6	9.8 ± 6.0	3.6 ± 2.5
x = 0.6	3.977(29)	3.977(29)	90	88.6	14.1 ± 10.5	7.8 ± 2.4
x = 0.8	3.986(33)	3.986(33)	90	87.6	14.8 ± 12.3	8.4 ± 3.8
x = 1.0	9.699(45)	13.009(64)	120	90.5	19.5 ± 10.6	10.5 ± 7.4

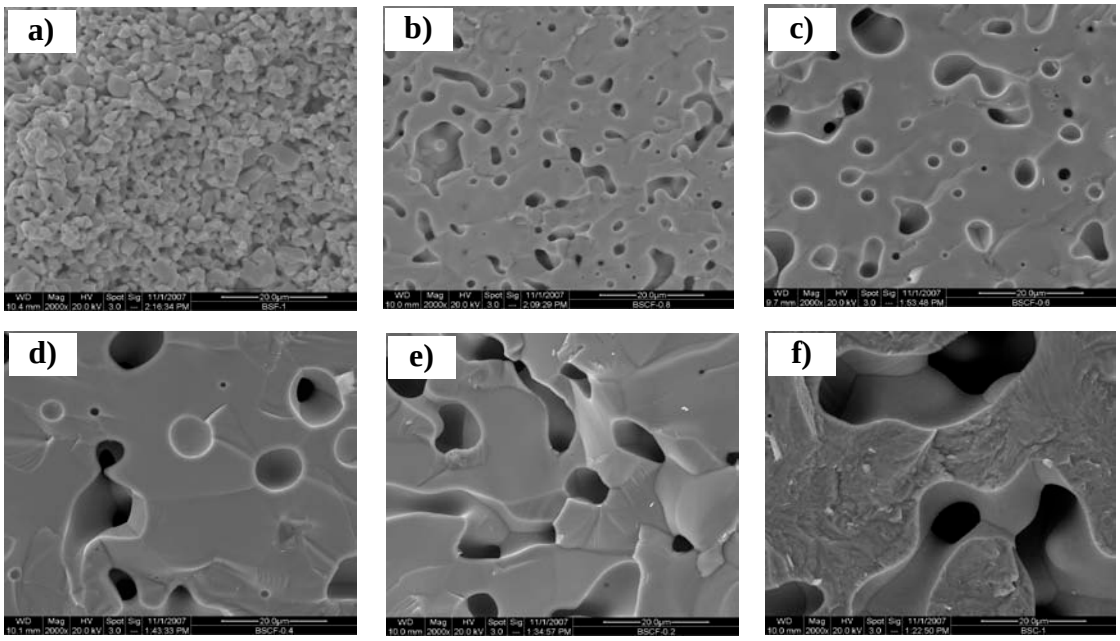

Figure 13. Microstructures for $Ba_{0.5}Sr_{0.5}Co_xFe_{1-x}O_{3-\delta}$ (x = 0 ~ 1.0) sintered at 1100°C for 5hrs in air: a) x = 0, b) x = 0.2, c) x = 0.4, d) x = 0.6, e) x = 0.8 and f) x = 1.0.

In Figure 14, conductivity is plotted as a function of temperature according to Equation (9), which is appropriate for conduction via adiabatic polaron hopping:[3]

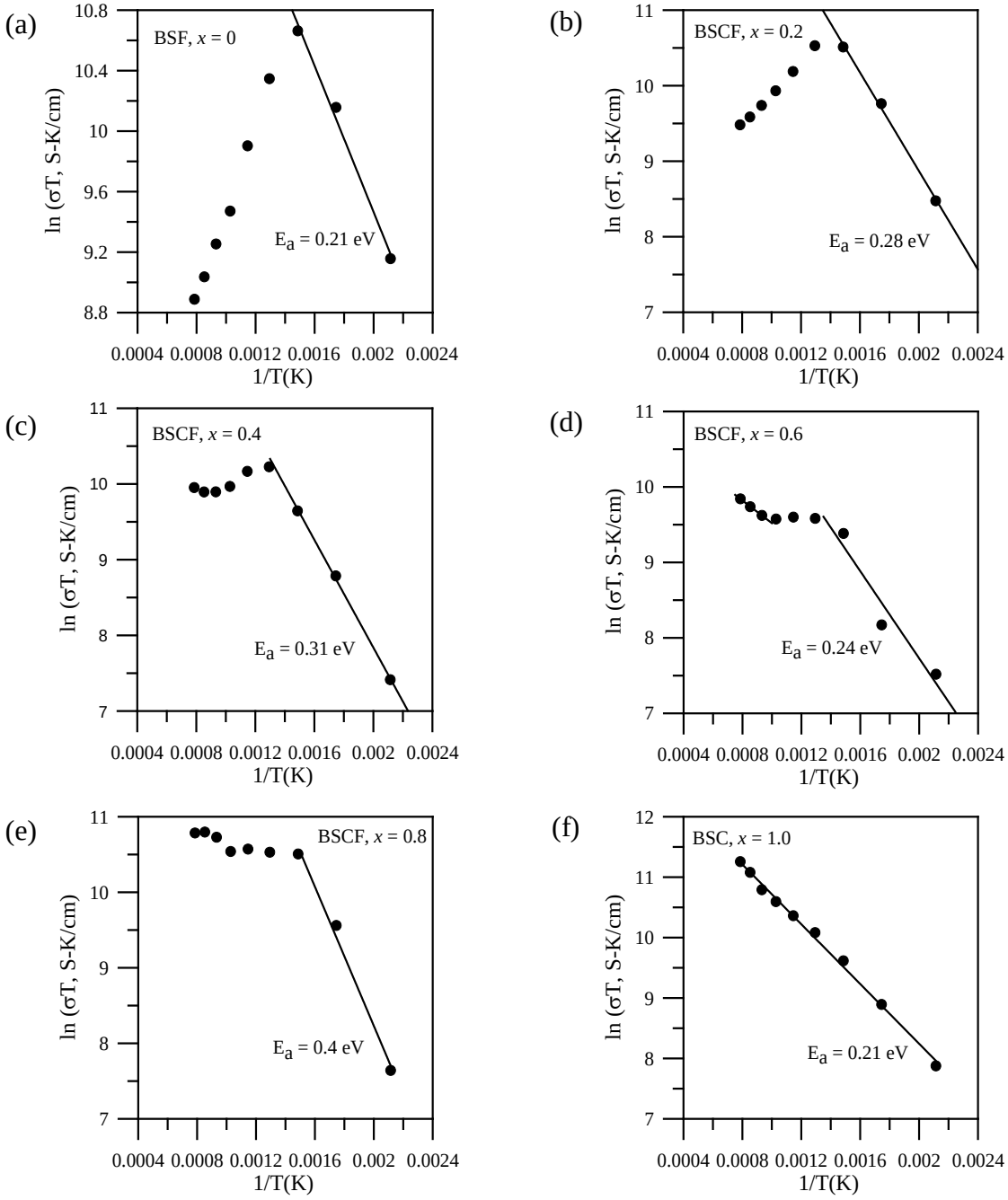

Figure 14. Ln (σT) versus 1/T for $Ba_{0.5}Sr_{0.5}Co_xFe_{1-x}O_{3-\delta}$ ($x = 0 \sim 1.0$) in air: (a) BSF $x = 0$, (b) $x = 0.2$, (c) $x = 0.4$, (d) $x = 0.6$, (e) $x = 0.8$, and (f) $x = 1.0$, BSC.

$$\sigma = \frac{A}{T} e^{-\frac{E_c}{kT}} \quad (9)$$

where E_a is activation energy, T is temperature in Kelvin, k is Boltzmann's constant, and A is the preexponential factor that depends on the site fraction of carriers and the probability that neighboring ions are available to participate in the hopping process. The conductivity of BSC (Figure 14 (f)) is thermally activated over the entire temperature range with an activation energy of 0.21eV. Below ~673K, the conductivity of BSF and BSCF (Figure 14 (a–e)) is thermally activated with activation energies ranging between 0.21eV and 0.40eV, which are comparable to those reported by others. As points of comparison, Grunbaum *et al.* reported activation energies ranging from 0.28 to 0.4eV for the cubic phase of $SrCo_{0.8}Fe_{0.2}O_{3-\delta}$,[4] and Wei *et al.* reported an activation energy of 0.4eV for $Ba_{0.5}Sr_{0.5}Co_{0.8}Fe_{0.2}O_{3-\delta}$ over the temperature range 100–400°C.[5] Above 673K, the slope of the data (ln σT vs. 1/T) generally increases with increasing cobalt concentration, ranging from a negative value in BSF to a positive value in the x=0.8 sample.

The conductivity of the BSCF5582 sample was measured as a function of temperature under static pO_2 conditions ranging from 10^{-5}atm to 1 atm. In general, the features of the ln σT vs. 1/T data were similar to those shown in Figure 15(e). In Figure 15, log σ is plotted as a function of log pO_2 for four temperatures between 300 and 900°C. At 300°C (Figure 15(a)), the conductivity ranges from 6–11 S/cm without a clear dependency on pO_2. At higher temperatures (Figure 15(b–d)), the slopes of logσ vs. log pO_2 is clearly positive for $pO_2 \geq 0.01$atm, suggesting p-type electronic conduction. Lines showing a 1/4 and 1/6 slopes are shown for comparison. At $pO_2 \leq 0.01$atm (Figure 15(b-d)), the slopes of the data are slightly negative values ranging -1/17 to -1/9.

Figure 16 summarizes the observed electrical behavior of the BSCF5582 sample investigated in this study. At low temperatures over the entire pO_2 range studied, BSCF 5582 is thermally activated with E_a ranging from 0.28eV to 0.40eV. In this region., conductivity does not appear to be strongly dependent on pO2. At $pO_2 \geq 0.01$atm, the conductivity above 673K is also thermally activated but with a much lower activation energy around 0.07eV. At $pO_2 \leq 0.01$atm, conductivity increases slightly with

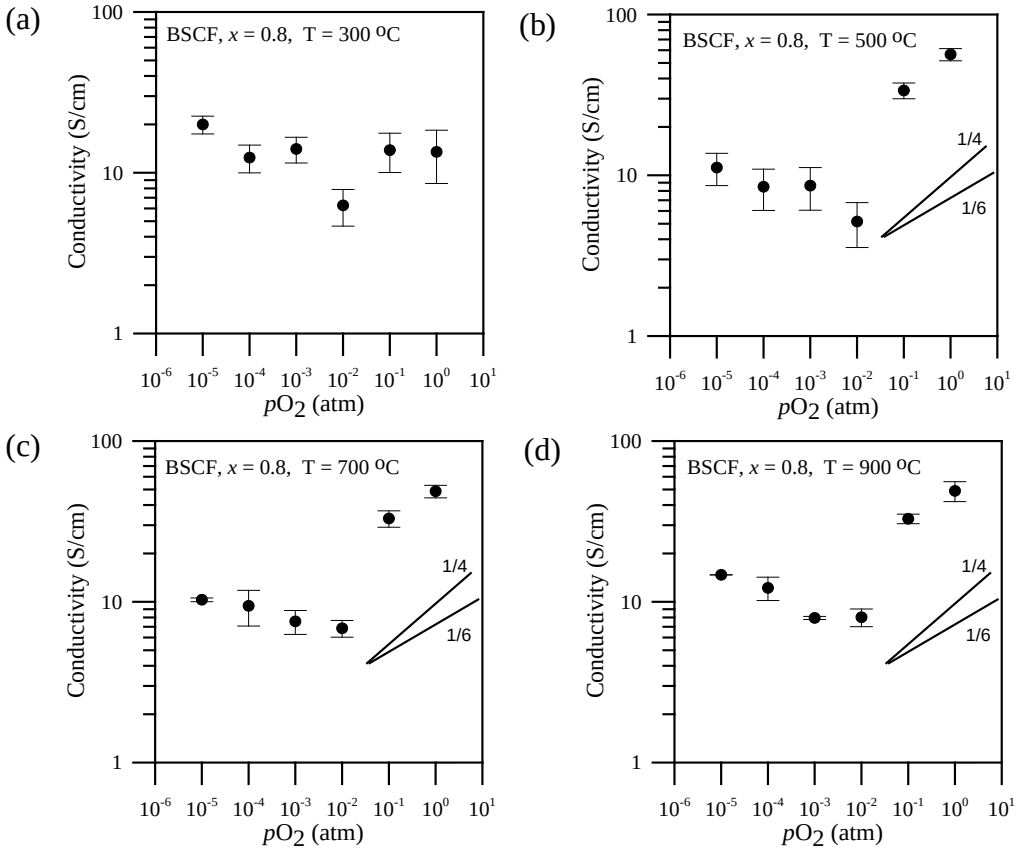

Figure 15. Log (σ) versus log (pO_2) for $Ba_{0.5}Sr_{0.5}Co_xFe_{1-x}O_{3-\delta}$ (x = 0.8): (a) 300 °C, (b) 500 °C, (c) 700 °C, and (d) 900 °C.

decreasing oxygen partial pressure above 673K. In this low pO_2 region, the temperature dependence of conductivity changes with temperature. Above 823K, the conductivity increases with increasing temperature and has an activation energy of around 0.2eV. Between ~673K and 823K, the conductivity decreases with increasing temperature.

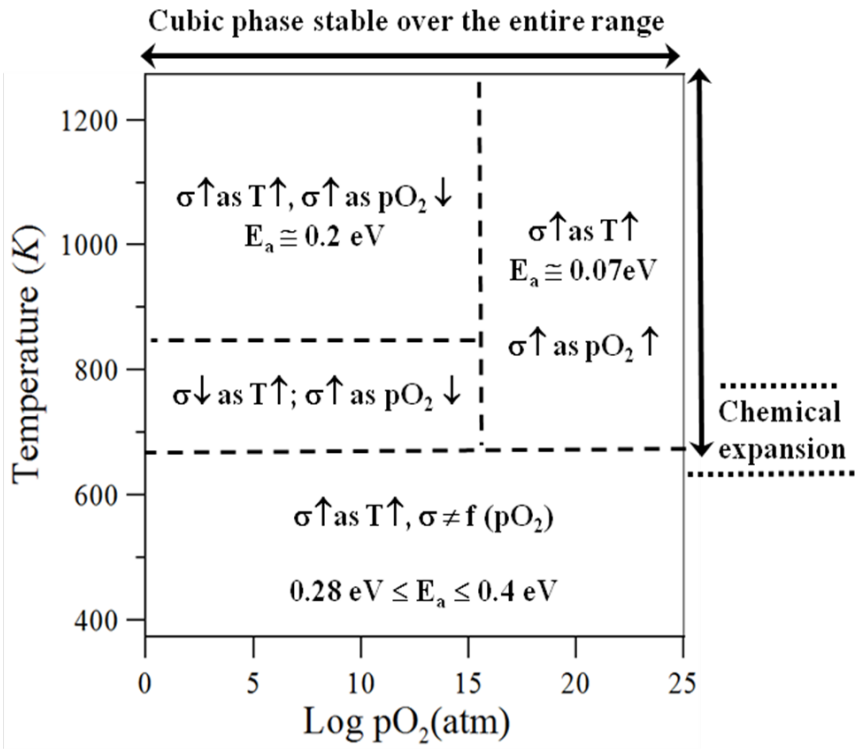

Figure 16. Schematic diagram summarizing DC conductivity trends in $Ba_{0.5}Sr_{0.5}Co_xFe_{1-x}O_{3-\delta}$ (x = 0.8) as a function of pO_2 and temperature.

D. Discussion

The defect chemistry of BSCF is complex. The B-site cations can adopt multiple valences and the defect concentration is sufficient high that the dilute-solution approximations may not be valid. Nevertheless, much of the observed behavior can be explained, at least qualitatively, by first assuming that the stoichiometric cubic perovskite $(Ba,Sr)^{2+}Fe^{4+}O_3$ is the parent structure and that the substitution of trivalent cobalt on tetravalent iron sites introduces oxygen vacancies according to Equation (10)

$$AO + (1-x)FeO_2 + \frac{x}{2}Co_2O_3 \rightarrow A_A + (1-x)Fe_{Fe} + xCo'_{Fe} + \left(3-\frac{x}{2}\right)O_O + \frac{x}{2}V_O^{\bullet\bullet} \qquad (10)$$

where x is the mole fraction of Co on the B site and A denotes the mixed occupancy of by Ba and Sr. As mentioned previously, the observed increase in the unit cell volume

with increasing cobalt concentration suggests that Co is incorporated primarily in its trivalent state.

Interaction with oxygen in the atmosphere alters the concentration of the electronic charge carriers in BSCF. Under high pO_2, the filling of oxygen vacancies produces electronic holes according to Equation (11) which has a corresponding equilibrium constant (K_{ox}):

$$\frac{1}{2}O_2(g) + V_O^{\bullet\bullet} \rightarrow O_O + 2h^{\bullet} \tag{11}$$

$$K_{ox} = \frac{[h]^2}{[V_O^{\bullet\bullet}]pO_2^{1/2}} = \frac{p^2}{[V_O^{\bullet\bullet}]pO_2^{1/2}}$$

Under low pO_2, the formation of additional oxygen vacancies produces electrons according to Equation (12) which has a corresponding equilibrium constant (K_{red}):

$$O_O \rightarrow V_O^{\bullet\bullet} + 2e' + \frac{1}{2}O_2(g) \tag{12}$$

$$K_{red} = [e']^2[V_O^{\bullet\bullet}]pO_2^{1/2}$$

The formation of electronic carriers according to Equation (11) and Equation (12) will alter the valent states of the B-site cations shown in Equation (10). The formation of holes will convert Co^{3+} to Co^{4+}, whereas the formation of electrons will convert Fe^{4+} to Fe^{3+} or possibly convert cobalt and iron to their divalent states. Divalent cobalt may also arise from the thermally induced charge disproportionation of Co^{3+} into Co^{4+} and Co^{2+} as reported for related oxides.[6]

A general defect reaction must include species that can account for the mixed electronic and ionic conductivity of BSCF. In the absence of unambiguous information about the valences of iron and cobalt, it must also allow B-site cations to assume multiple valences depending on oxygen partial pressure and temperature. Equation (13) meets these criteria:

$$AO + (1-v-w)BO_2 + \frac{v}{2}B_2O_3 + wBO \rightarrow A_A + (1-v-w-y)B_{Fe} + (v+y-z)B'_{Fe} + (w+z)B''_{Fe} + \left(3-\frac{v}{2}-w-\frac{y}{2}-\frac{z}{2}\right)O_O + \left(\frac{v}{2}+w+\frac{y}{2}+\frac{z}{2}\right)V_O^{\bullet\bullet} + \frac{y+z}{4}O_2(g) \quad (13)$$

The variables v and w are used to identify the fraction of B site cations in their trivalent and divalent states, respectively, at some standard state, i.e. room temperature and pO_2= 0.21atm. The variables y and z identify the amount of B^{4+} reduced to B^{3+} and the amount of B^{3+} reduced to B^{2+}, respectively, under non-standard conditions. In other words, the values of y and z are zero at 298K and pO_2 = 0.21atm but change with temperature and partial oxygen pressure.

Equations (11) - (13) provide a framework for discussing the electrical behavior of BSF and BSCF as a function of temperature and pO_2. To simplify the discussion, the ionic contribution to the total electrical conductivity is neglected, which is reasonable considering that the measured conductivities are two to three orders of magnitude higher than the ionic conductivities reported by Bucher *et al.*.[7] Because it is unlikely that equilibrium was achieved within the 10 min dwell time used in our measurements, it is important to recognize that the thermal history of the samples may influence some of the observed trends. As a point of reference, Bucher *et al.* reported oxygen chemical diffusion coefficients of $10^{-6}cm^2/s$ for BSCF at 550°C; this would imply a penetration depth of ~0.5mm ($x=(4Dt)^{1/2}$) after 10min whereas the shortest dimension in our samples was several millimeters.

As shown in Figure 15, there is a marked change in the electrical behavior of BSF and BSCF at ~673K, which coincides with changes in weight loss and thermal expansion reported previously by our group.[1] Thermogravimetric analysis of the BSCF samples showed that oxygen vacancies are inactive below 673K. According to Equations (11) - (13), this implies that the carrier concentration is constant and presumably fixed by the valences of B-site cations quenched-in from higher temperatures. If conductivity is thermally activated below 673K but carrier concentration is constant, then carrier mobility must be activated, which is indicative of a polaron hopping mechanism. P-type polaron conduction arises from hopping between B^{3+} and B^{4+} cations whereas n-type arises from hopping between B^{3+} and B^{2+}. We infer that the BSCF samples measured in

air below 673K were p-type conductors because they were quenched in air from higher temperatures where p-type behavior was observed in BSCF5582 (Figure 15(b–d)).

When heated in air, BSCF powders undergo reversible weight loss above 673 K, which is attributed to oxygen vacancy formation. In general, the weight loss increases with increasing iron content, which suggests that it is largely associated with the reduction of iron, presumably from Fe^{4+} to Fe^{3+}. An increase in the concentration of oxygen vacancies effectively reduces the concentration of p-type carriers by producing electrons according to Figure 15, or by increasing the values of y and z according to Figure 16. For the x=0.6 and 0.8 samples (Figure 14(d and e)), the activation energy observed above ~673K results from two thermally activated processes: (1) the formation of oxygen vacancies which decreases the p-type carrier concentration and (2) the hopping of electrons between B^{3+} and B^{4+} sites. For samples with $x \leq 0.4$, the decrease in p-type carrier concentration is sufficient to result in a negative slope in the $\ln \sigma T$ vs. $1/T$ graphs.

The conductivity of BSCF5582 at 300°C (Figure 15 (a)) does not show a discernable dependence on pO_2 because oxygen vacancies are inactive below 673 K. Above 673K and $pO_2 \geq 0.01$atm, the conductivity increases with increasing pO_2 (Figure 15(b-d)), because oxygen vacancies are being filled and p-type carriers are being produced according to Figure 14. According to a simple analysis of Equation (11), the slope $\log(\sigma)$ vs. $\log pO_2$ will be in the range $1/6 \leq m \leq 1/4$, depending on the electroneutrality conditions used. At $pO_2 \geq 0.1$atm, the slope of the collected data ranges from 0.17 to 0.22 for three different temperatures. When pO_2 decreases from 0.1 to 0.01atm, the conductivity drops to a value considerably lower than expected based on the high pO_2 data (Figure 15 (b–d)). A similar trend was reported by Grunbaum *et al.* for SCF below 973K[4] and was attributed to the transition from a cubic perovskite structure to an orthorhombic Brownmillerite structure.[8] However, a similar phase transition has not been observed in BSCF5582.[1]

Above 673K and at $pO_2 \leq 0.01$atm, the conductivity of BSCF5582 increases slightly with decreasing pO_2 which suggests n-type behavior. The slopes in the logs vs. $\log pO_2$ graphs are much more shallow than the slope expected ($m = -1/6$) for a simple analysis of Figure 15. The observed slopes may result from a broad shallow minimum in the $\log \sigma$ vs. $\log pO_2$ data or from non-idealities typical of systems with high defect

concentrations. While measuring the conductivity of BSCF at $pO_2 \leq 10^{-5}$ would be informative, it cannot be accomplished with the CO/CO_2 mixtures typically used in such studies because BSCF readily reacts with CO_2. At high temperature (≥ 823K) and low pO_2 ($pO_2 \leq 0.01$atm), the conductivity of BSCF is thermally activated (E_a= 0.2eV), which may be due to hopping between B^{3+} and B^{2+} cations. However, further evidence of n-type behavior is needed. At intermediate temperatures (673–823K) and low pO_2, the conductivity decreases slightly with increasing temperature. The decrease in conductivity is not well understood, but may depend on the thermal history of the samples.

E. Conclusions

The phase stability of BSCF $Ba_{0.5}Sr_{0.5}Fe_{1-x}Co_xO_{3-\delta}$ (x = 0-1) has been investigated using high temperature X-ray diffraction and TG/DTA. All BSCF compositions and the end member BSF were stable down to 10^{-5}atm pO_2 to 1000°C. The electrical conductivity of $Ba_{0.5}Sr_{0.5}Co_{1-x}Fe_xO_{3-\delta}$ ($0 \leq x \leq 1$) was measured as a function of temperature, and the conductivity of BSCF5582 was measured as a function of pO_2 as well. The electrical conductivity of BSCF below ~673K is thermally activated ($0.2 \leq E_a \leq 0.4$eV) and is dominated by p-type polaron hopping between B^{3+} and B^{4+} cations. Above ~673K and pO_2>0.01 atm, the formation of oxygen vacancies results in a decrease in carrier concentration in BSCF5582, but conduction is still dominated by hopping between B^{3+} and B^{4+} cations. At $pO_2 \leq 0.01$atm above ~673K, n-type conduction is observed, presumably due to hopping between B^{3+} and B^{2+} cations with an activation energy of ~ 0.2eV.

F. References

1. J. Ovenstone, J. Jung, J. White, D. Edwards, and S. Misture, "Phase Stability of BSCF in Low Oxygen Partial Pressures," *J. Solid State Chem.,* **181** [3] 576-86 (2008).

2. R. Shannon, "Revised Effective Ionic Radii and Systematic Studies of Interatomic Distances in Halides and Chalcogenides," *Acta Crystallogr., Sect. A: Cryst. Phys., Diffr., Theor. Gen. Crystallogr.,* **32** [5] 751-67 (1976).

3. P. Zeng, Z. Chen, W. Zhou, H. Gu, Z. Shao, and S. Liu, "Re-Evaluation of $Ba_{0.5}Sr_{0.5}Co_{0.8}Fe_{0.2}O_{3-\Delta}$ Perovskite as Oxygen Semi-Permeable Membrane," *J. Membr. Sci.*, **291** [1-2] 148-56 (2007).

4. N. Grunbaum, L. Mogni, F. Prado, and A. Caneiro, "Phase Equilibrium and Electrical Conductivity of $SrCo_{0.8}Fe_{0.2}O_{3-\delta}$," *J. Solid State Chem.*, **177** [7] 2350-7 (2004).

5. B. Wei, Z. Lü, X. Huang, J. Miao, X. Sha, X. Xin, and W. Su, "Crystal Structure, Thermal Expansion and Electrical Conductivity of Perovskite Oxides $Ba_xSr_{1-x}Co_{0.8}Fe_{0.2}O_{3-\delta}(0.3 \leq x \leq 0.7)$," *J. Eur. Ceram. Soc.*, **26** [13] 2827-32 (2006).

6. L. W. Tai, M. M. Nasrallah, H. U. Anderson, D. M. Sparlin, and S. R. Sehlin, "Structure and Electrical Properties of $La_{1-x}Sr_xCo_{1-y}Fe_yO_3$. Part 1. The System $La_{0.8}Sr_{0.2}Co_{1-y}Fe_yO_3$," *Solid State Ionics*, **76** [3-4] 259-71 (1995).

7. E. Bucher, A. Egger, P. Ried, W. Sitte, and P. Holtappels, "Oxygen Nonstoichiometry and Exchange Kinetics of $Ba_{0.5}Sr_{0.5}Co_{0.8}Fe_{0.2}O_{3-\Delta}$," *Solid State Ionics*, **179** [21-26] 1032-5 (2008).

8. S. McIntosh, J. Vente, W. Haije, D. Blank, and H. Bouwmeester, "Structure and Oxygen Stoichiometry of $SrCo_{0.8}Fe_{0.2}O_{3-\delta}$ and $Ba_{0.5}Sr_{0.5}Co_{0.8}Fe_{0.2}O_{3-\Delta}$," *Solid State Ionics*, **177** [19-25] 1737-42 (2006).

V. OXYGEN STOICHIOMETRY, ELECTRICAL CONDUCTIVITY, AND THERMOPOWER MEASUREMENTS OF BSCF

A. Introduction

The DC electrical conductivity and Seebeck coefficient of sintered BSCF ceramics ($Ba_{0.5}Sr_{0.5}Co_xFe_{1-x}O_{3-\delta}$, $0 \leq x \leq 0.8$) were simultaneously measured from 200 - 900°C in air. Oxygen stoichiometry (3-δ) was determined from iodometry at room temperature and thermogravimetry analysis to 900°C. The electrical conductivity was thermally activated at low temperatures, exhibiting a maximum of 32 ± 4S/cm at ~ 400°C and then decreasing with increasing temperature above 400°C. The Seebeck coefficient ranged from a minimum of 37 ± 10μV/K for all compositions at ~ 300 °C to 150μV/K for x = 0 and 67μV/K for x = 0.8 at 900°C. Oxygen stoichiometry ranged from 2.65 for x = 0 and 2.54 for x = 0.8 at 100°C to 2.55 for x = 0 and 2.36 for x = 0.8 at 900°C. A simple p-type polaron hopping model, assuming negligible contribution from n-type or ionic carriers, was used to extract the carrier concentration and mobilities from the measured data. The calculated mobilities were < $0.1 cm^2/V\text{-}s$, supporting the p-type polaron-hopping model. For a given composition, the activation energy for conduction below ~350°C was identical to that of the carrier mobility, ranging from 0.2eV for x = 0 to 0.6eV for x = 0.8. Above 350°C, the activation energy for carrier mobility decreased dramatically, ranging from 0.05eV for x = 0.2 to 0.1eV for x = 0.8. Unlike the carrier mobilities of the $x \geq 0.2$ samples, the carrier mobility for the x = 0 sample did not appear to be thermally activated above 350°C.

The DC electrical conductivity and Seebeck coefficient (Q) of sintered BSCF ceramics ($Ba_{0.5}Sr_{0.5}Co_xFe_{1-x}O_{3-\delta}$, $0 \leq x \leq 0.8$) were simultaneously measured as a function of pO_2(atm) ($10^{-5} \leq pO_2 \leq 1$) at temperatures of 500°C, 700°C and 900°C. The positive Seebeck coefficients across the compositional range signify that BSCF is predominated by p-type conduction. BSF(x=0) at 900°C in the range of $\sim 10^{-3} \leq pO_2 \leq 1$ shows that the slopes of conductivity vs. pO_2 and $Q/(k/e)$ vs. $\ln pO_2$ approach to ideal values of ¼ and

-¼, respectively, which means that conduction is almost purely dominated by *p*-type polaron hopping without any effect of oxygen vacancy on electrical properties. However, the simultaneous increase of cobalt concentration (x) and temperature cause both the slopes of conductivity vs. pO_2 and $Q/(k/e)$ vs. $\ln pO_2$ to deviate systematically from ideal values, which is understood to come from the increase of Co^{+2} with increasing cobalt concentration. At $10^{-5} \leq pO_2 \leq \sim 10^{-3}$, the slopes are bent down due to the reduction of Fe^{+3} to Fe^{+2}, which contributes to the disruption of conduction chains in Fe^{+4}-O^{-2}-Fe^{+3} and explains the relatively low increase of mobility vs. pO_2. When the whole data of Q were plotted vs. $\ln pO_2$ as Jonker plots, x=0.2 and 0 are -74.9μV/K and -68.7μV/K, respectively, and x=0.8 is -11.94μV/K at 900°C in the range of $\sim 10^{-3} \leq pO_2 \leq 1$.

B. Results

Figure 17 shows the oxygen stoichiometry (3-δ) of samples prepared as $Ba_{0.5}Sr_{0.5}Co_xFe_{1-x}O_{3-\delta}$ ($0 \leq x \leq 0.8$)), where room-temperature values were determined by iodometric titration and higher-temperature values were calculated from thermogravimetric analysis. The oxygen stoichiometries measured in this work lie within the range reported in the literature. The oxygen content is nearly constant at temperatures lower than 200°C, and then decreases with increasing temperature at higher temperatures. Previous thermogravimetric data reported by our group for BSCF5582 and BSCF5528 showed the onset of weight loss at ~400°C, when using a faster heating rate of 5-10 K/min with no equilibrium time. The difference in the two sets of data likely results from the sluggish kinetics of the system at low temperature.

Also shown in Figure 17, is the mean oxidation state of the transition metal cations (B = Co and Fe) assuming that the oxidation state of barium/strontium is +2 and that of oxygen is -2. At 400 to 500°C, depending on composition, the oxygen content in the formula unit $ABO_{3-\delta}$ is 2.5, indicating that the transition metal cations have a mean oxidation state of +3. At lower temperatures where the oxygen content is greater than 2.5, a mixture of B^{3+} and B^{4+} predominates. At higher temperatures, a significant amount of divalent B^{2+} must be present to account for a mean oxidation state less than 3.

Assuming that the mean oxidation of iron is independent of the Co/Fe ratio, i.e. assuming that iron maintains the mean oxidation state of the x = 0 sample, the mean

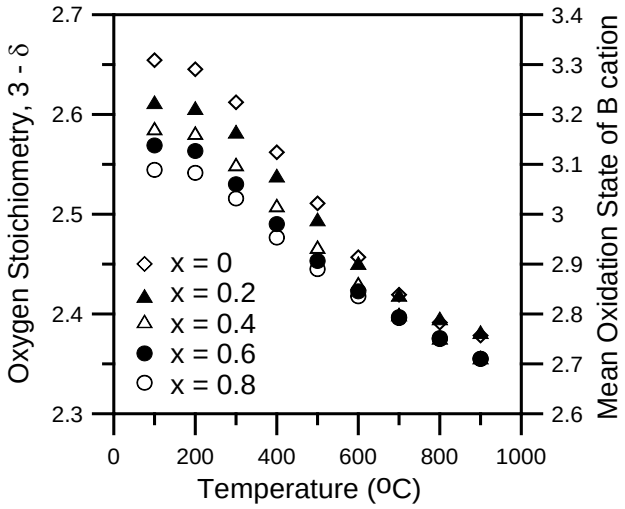

Figure 17. The oxygen content (3-δ) as a function of temperature in $Ba_{0.5}Sr_{0.5}Co_xFe_{1-x}O_{3-\delta}$ ($0 \leq x \leq 0.8$) determined from iodometric titration (room temperature, not shown) and thermogravimetric analysis from room temperature to 900°C. The mean oxidation state of transition metal cation (B) calculated assuming that Ba^{2+}, Sr^{2+}, and O^{2-} have constant oxidation states.

oxidation state of cobalt in the $0.2 \leq x \leq 0.8$ samples can be calculated using Equation (14):

$$Z_{Co} = \frac{Z_B - (1-x)Z_{Fe}}{x} \tag{14}$$

where x is the fraction of cobalt on the B site and Z_i (i = Co, Fe) is the mean oxidation state of Co, Fe and combined B-site cations. As shown in Figure 18, the calculated oxidation state of cobalt for the $x \geq 0.4$ compositions decreases steadily with increasing temperature from 3.01 ± 0.04 at 100°C to 2.68 ± 0.03 at 900°C.

It is important to recognize that the uncertainty in the absolute values of the mean oxidation state derived from iodometry data is quite high (ca. ±0.2), whereas the uncertainty in the change in oxidation state calculated from TGA data is quite low (ca. ±0.005). Nevertheless, the mean oxidation state of cobalt calculated by this method is comparable to that reported by Mueller *el al.* for BSCF1982 based on XANES spectroscopy, i.e. 2.8 for BSCF5582 at 600°C compared to 2.74 for BSCF1982 at 603°C.

On the other hand, the mean oxidation state of iron derived from the current analysis is considerably higher than that reported by Mueller, i.e. 2.9 for BSCF5582 at 600^{o}C compared to 2.71 for BSCF1982 at 603^{o}C.

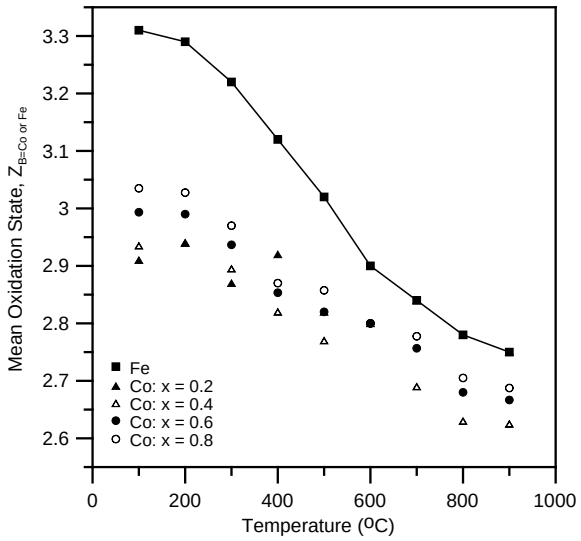

Figure 18. Mean oxidation state of iron and cobalt in $Ba_{0.5}Sr_{0.5}Co_xFe_{1-x}O_{3-\delta}$ ($0 \leq x \leq 0.8$) calculated from room temperature iodometry and thermogravimetric data and assuming that the mean oxidation state of iron was independent of Co/Fe ratio.

Figure 19(a) shows the DC conductivity of BSCF samples measured in the air. For all the samples, conductivity increases up to 32 ± 4S/cm with increasing temperature to ~350°C, then the magnitude and temperature-dependence of the conductivity are similar to that reported by us and others previously.[1-2] In Figure 19(b), the electrical conductivity is plotted as a function of reciprocal temperature according to Equation (15), which assumes conduction via adiabatic polaron hopping:

$$\sigma = \frac{A}{T} e^{-\frac{E_a}{kT}} \tag{15}$$

where E_a is activation energy, T is temperature in Kelvin, k is Boltzmann's constant. The pre-exponential factor, A, is partly dependent on the site fraction of charge carriers and

the probability that neighboring ions are available to participate the hopping mechanism. The slopes of the data (lnσT vs. 1/T) show systematic variation with cobalt

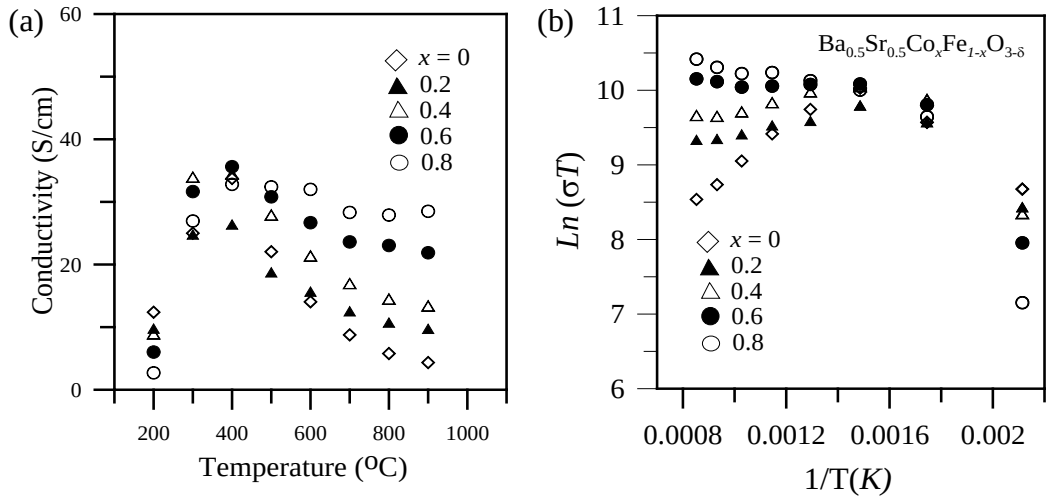

Figure 19. The DC electrical conductivity of $Ba_{0.5}Sr_{0.5}Co_xFe_{1-x}O_{3-\delta}$ ($0 \leq x \leq 0.8$) in air: (a) conductivity vs. T (°C) and (b) ln (σT) vs. 1/K.

concentration. The conductivity is thermally activated below ~350°C, with activation energies (E_a) ranging from 0.2eV to 0.6eV as the cobalt concentration increases, as shown in Table V. Above 400°C, the slopes of lnσT vs. 1/T range from positive for $x \leq 0.4$ to negative for $x \geq 0.6$. The activation energies (E_a) for the $x \geq 0.6$ samples are less than 0.1eV.

The uncertainty in the reported low-temperature activation energies, E_A, is quite high because they were determined from only two data points. Nevertheless, the values are similar to those reported previously. Our group reported values ranging from 0.21eV for $x = 0$ to 0.4eV for $x = 0.8$.[2] Harvey *et al.* reported values of 0.25eV for $x = 0.2$ and 0.34eV for $x = 0.8$.[3]

Figure 20 shows the Seebeck coefficient of the BSCF samples measured in air. The Seebeck coefficient is positive for all samples ($0 \leq x \leq 0.8$), which means that conduction is dominated by *p*-type carriers. Below 600°C, the Seebeck coefficient shows relatively small differences with composition and generally increases with increasing temperature. Above 600°C, the temperature dependence of the Seebeck coefficient

varies significantly with composition. For x = 0, the Seebeck coefficient continues to increase with increasing temperature. For x = 0.8, the Seebeck coefficient levels off at around 70μV/K. As a point of comparison, the thermopower of $Ba_{0.5}Sr_{0.5}FeO_{3-\delta}$ is comparable to that reported for $BaFeO_{3-\delta}$ and $SrFeO_{3-\delta}$, e.g. ~25μV/K vs. 10μV/K at 400°C and ~35μV/K compared to 45μV/K at 6000°C.[4]

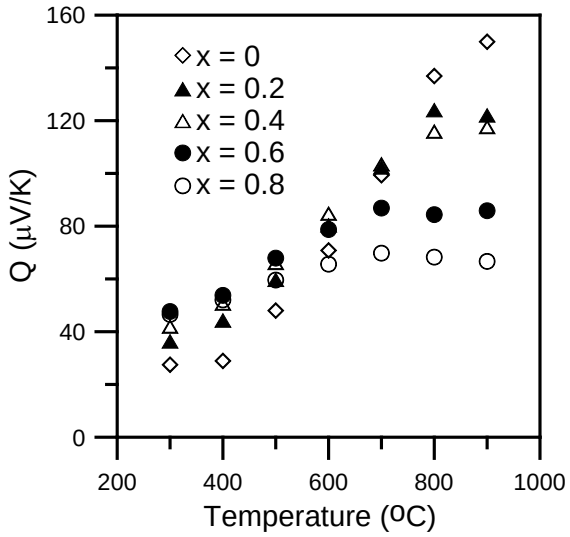

Figure 20. Seebeck coefficient, Q, of $Ba_{0.5}Sr_{0.5}Co_xFe_{1-x}O_{3-\delta}$ ($0 \leq x \leq 0.8$) as a function of temperature in air.

Figure 21 shows the DC conductivity vs. pO_2(atm) at the temperatures of (a) 500°C, (b) 700°C, and (c) 900°C across the compositional range of BSCF ($Ba_{0.5}Sr_{0.5}Co_xFe_{1-x}O_{3-\delta}$, $0 \leq x \leq 0.8$) ceramics. The positive slopes of conductivity vs. pO_2 at 500°C are nearly linear, and they slightly decrease from 1/3.9 to 1/5.3 with increasing cobalt concentration, as shown in Figure 21(a). Figure 21(b) shows that the slopes of conductivity vs. pO_2 are no longer linear at 700°C, but start slightly bending up at around 10^{-3} atm. The slopes at ~ $10^{-3} \leq pO_2 \leq 1$ decrease from 1/ 2.8 to 1/ 6.9 and the slopes at $10^{-5} \leq pO_2 \leq 10^{-3}$ decrease from 1/5.1 to 1/11.3 with increasing cobalt concentration, as summarized in Table II.

It is noticeable that, with decreasing cobalt concentration and increasing temperature, the conductivity decreases, and the slope increases and approaches to ¼ at

$\sim 10^{-3} \leq pO_2 \leq 1$. This eventually results in the higher conductivity differences between x=0.8 and x=0 ($\Delta\sigma_{x=0\sim0.8}$). Figure 21(c) shows conductivity vs. pO_2 at 900°C, where, $\Delta\sigma_{x=0\sim0.8}$ at $pO_2 = 10^{-5}$ is 13.1 S/cm, and $\Delta\sigma_{x=0\sim0.8}$ at $pO_2 = 1$ is 30.0S/cm, which are significantly higher than at 500°C, where $\Delta\sigma_{x=0\sim0.8}$ at $pO_2 = 10^{-5}$ is 3.2S/cm and $\Delta\sigma_{x=0\sim0.8}$ at $pO_2 = 1$ is 16.3S/cm. In Figure 21(c), with increasing cobalt concentration, the slopes at $10^{-5} \leq pO_2 \leq 10^{-3}$ decrease from 1/11.4 to 1/32.5 and the slopes at $\sim 10^{-3} \leq pO_2 \leq 1$ decrease from 1/3.7 to 1/8.3, showing that the positive slope of conductivity vs. pO_2 at BSF (x=0) approximate to 1/4, as summarized in Table II.

Table II. A Summary of the Slopes (1/n) of DC Conductivity vs. pO_2 for $Ba_{0.5}Sr_{0.5}Co_xFe_{1-x}O_{3-\delta}$ ($0 \leq x \leq 0.8$) at Temperatures of 500°C, 700°C and 900°C

n	$10^{-5} \leq pO_2(atm) \leq \sim 0.01$			$\sim 0.01 \leq pO_2(atm) \leq 1$		
	500 °C	700 °C	900 °C	500 °C	700 °C	900 °C
x = 0	4.8	5.1	11.4	3.9	2.8	3.7
0.2	5.6	9.6	18	3.6	4.2	5.6
0.4	5.4	11.6	20.2	4.3	4	5.1
0.6	6.6	14.3	24.8	4.2	4.9	7
0.8	5.8	11.3	32.5	5.3	6.9	8.3

When we consider the defect chemistry of *p*-type conduction, as shown in Equation (16), the ideal slope of charge carrier concentration vs. pO_2 is ¼, on the assumption that oxygen vacancy itself does not affect conduction.

$$O_O + 2h^{\bullet} = \frac{1}{2}O_2(g) + V_O^{\bullet\bullet}$$

$$K = \frac{[V_O^{\bullet\bullet}]pO_2^{1/2}}{p^2} \qquad (16)$$

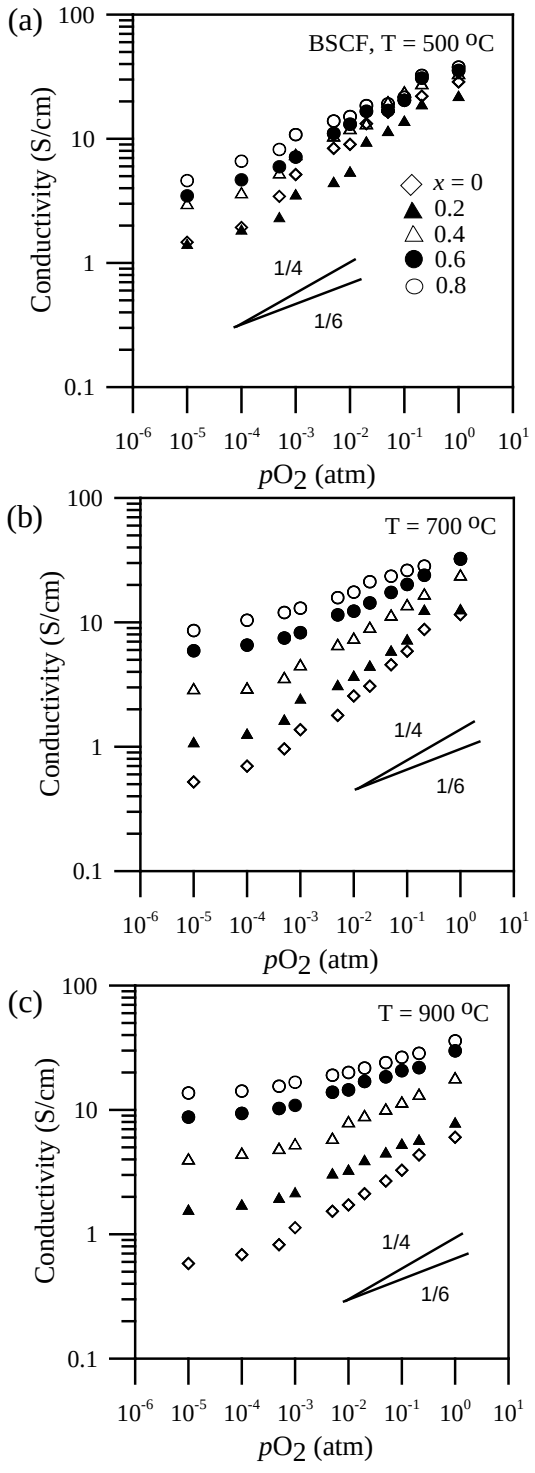

Figure 21. DC conductivity (S/cm) vs. pO_2 (atm) for $Ba_{0.5}Sr_{0.5}Co_xFe_{1-x}O_{3-\delta}$ ($0 \leq x \leq 0.8$) at temperatures of (a) 500°C, (b) 700°C and (c) 900°C in air using thermoelectric power method.

where, p denotes [$\dot{h}$], the charge carrier concentration. The measured positive does not so much contribute to conductivity (σ), but p is determinant in $\sigma = pe\mu$. Figure 22 shows Seebeck coefficients(Q) vs. pO_2 at the temperatures of (a) 500°C, (b) 700°C, and (c) 900°C across the compositional range of BSCF ($Ba_{0.5}Sr_{0.5}Co_xFe_{1-x}O_{3-\delta}$, $0 \le x \le 0.8$) ceramics. The Seebeck coefficients are positive over the whole range of $10^{-5} \le pO_2 \le 1$, which suggests that *p*-type electronic conduction is predominant in sintered BSCF ceramics.

Figure 22(a) shows that slopes of $Q/(k/e)$ vs. $\ln pO_2$ range between -1/8 and -1/11, and are almost negatively linear, except for slight curvative at $pO_2 = \sim 10^{-3}$ at 500°C for x=0.8. At 700°C, Figure 22(b), the overall slopes start bending down, mostly around $pO_2 = 10^{-3}$ with higher cobalt concentration at slightly higher pO_2, while the negative slopes systematically increase from -1/6 to -1/34 with increasing cobalt concentration.
As temperature increases, the overall critical points, where slopes of $Q/(k/e)$ vs. $\ln pO_2$ are curved down, shift further to the higher pO_2, as shown in Figure 22(c), at 900°C, where the negative slopes increase from -1/5 to -1/54 with increasing cobalt concentration. It is noticeable that negative slopes of $Q/(k/e)$ vs. $\ln pO_2$ approach -1/4, as cobalt concentration and temperature are close to x=0 and T=900°C at $\sim 10^{-3} \le pO_2(\text{atm}) \le 1$, as summarized in Table III.

On the assumption that most charge carriers are in the state as B^{4+}, the Seebeck coefficients can be expressed as Equation (17),

$$Q = \frac{k}{e}\left[\ln\frac{[B^{3+}]}{\beta_p[B^{4+}]} + \frac{S_T}{K}\right] \qquad (17)$$

where, k/e is 86.17μV/K, the second term, S_T/K, is considered to contribute less than $10\mu V/K$ to the thermopower in polaron hopping conduction,[5] and the spin degeneracy, β_p, is assumed to be 6/5 as appropriate, for iron in its high spin state.

Figure 23 shows the plots of μ (cm^2/V-sec) vs. pO_2 calculated simultaneously from the conductivity and Seebeck coefficient (Q) of $Ba_{0.5}Sr_{0.5}Co_xFe_{1-x}O_{3-\delta}$ ($x = 0 \sim 0.8$) at temperatures of (a) 500°C, (b) 700°C and (c) 900°C. The overall μ increases with

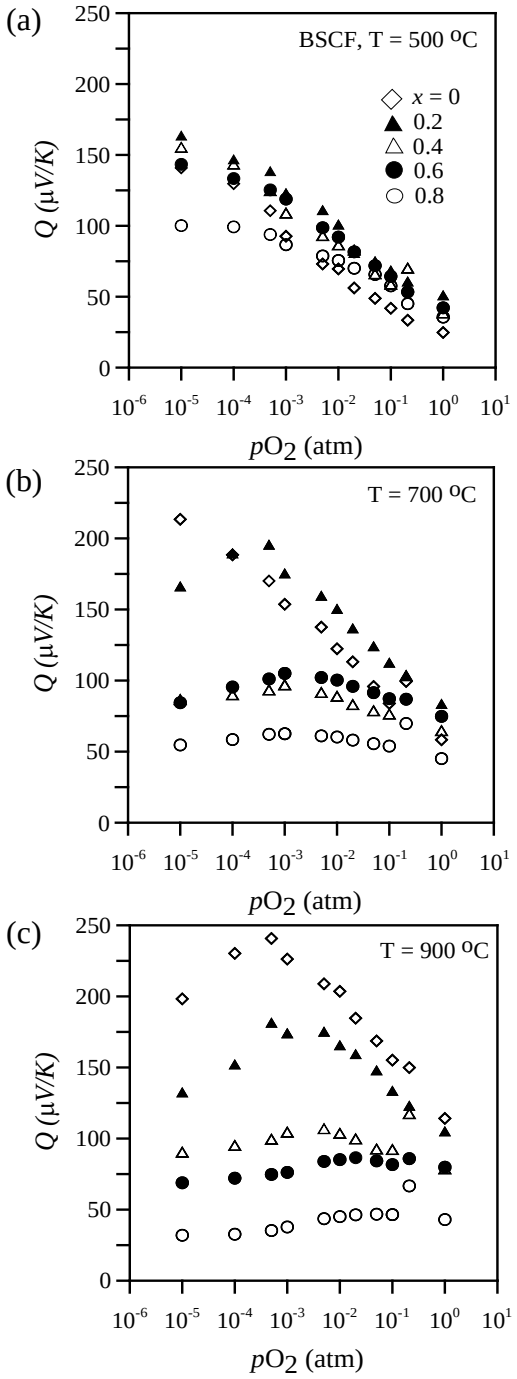

Figure 22. Seebeck coefficient (Q) vs. pO_2 (atm) for $Ba_{0.5}S_{r0.5}Co_xFe_{1-x}O_{3-\delta}$ ($0 \leq x \leq 0.8$) at temperatures of (a) 500°C, (b) 700°C and (c) 900°C using thermoelectric power method.

increasing cobalt concentration and pO_2. Table IV shows that, at $10^{-5} \leq pO_2 \leq \sim 10^{-3}$, the slopes of μ (cm^2/V-sec) vs. pO_2 increase from 1.0×10^{-3} to 1.9×10^{-3} at 500°C, and from 0.8×10^{-3} to 0.9×10^{-3} at 900°C, with increasing cobalt concentration; whereas, at

Table III. The Slopes (1/m) of Seebeck Coefficient (Q) vs. lnpO_2 for $Ba_{0.5}Sr_{0.5}Co_xFe_{1-x}O_{3-\delta}$ ($0 \leq x \leq 0.8$) at Temperatures of 500°C, 700°C and 900°C

m	$10^{-5} \leq pO_2$(atm) $\leq \sim 0.01$			$\sim 0.01 \leq pO_2$(atm) ≤ 1		
	500°C	700°C	900°C	500°C	700°C	900°C
x = 0	9	8	-8	8	6	5
0.2	11	-11	-8	8	6	8
0.4	9	-41	-30	9	21	19
0.6	17	-20	-35	8	19	57
0.8	33	-48	-44	11	34	54

$\sim 10^{-3} \leq pO_2 \leq 1$, the slopes increase from 2.9×10^{-3} to 3.5×10^{-3} at 500°C, and from 0.7×10^{-3} to 3.5×10^{-3} at 900°C. In summary, the slope increases more noticeably with

Table IV. The Summarized Slopes (1/s) of σ (cm^2/V-sec) vs. lnpO_2(atm) for $Ba_{0.5}S_{r0.5}Co_xFe_{1-x}O_{3-\delta}$ ($0 \leq x \leq 0.8$) at Temperatures of 500°C, 700°C and 900°C

s	$10^{-5} \leq pO_2$(atm) $\leq \sim 0.01$			$\sim 0.01 \leq pO_2$(atm) ≤ 1		
	500 °C	700 °C	900 °C	500 °C	700 °C	900 °C
x = 0	1.0×10^{-3}	0.3×10^{-3}	0.9×10^{-3}	2.9×10^{-3}	1.7×10^{-3}	0.7×10^{-3}
0.2	0.5×10^{-3}	0.9×10^{-3}	0.9×10^{-3}	2.7×10^{-3}	1.7×10^{-3}	0.7×10^{-3}
0.4	1.1×10^{-3}	0.7×10^{-3}	0.8×10^{-3}	3.9×10^{-3}	3.8×10^{-3}	2.8×10^{-3}
0.6	1.3×10^{-3}	1.2×10^{-3}	0.8×10^{-3}	3.7×10^{-3}	4.2×10^{-3}	3.5×10^{-3}
0.8	1.9×10^{-3}	1.5×10^{-3}	0.8×10^{-3}	3.5×10^{-3}	3.5×10^{-3}	3.5×10^{-3}

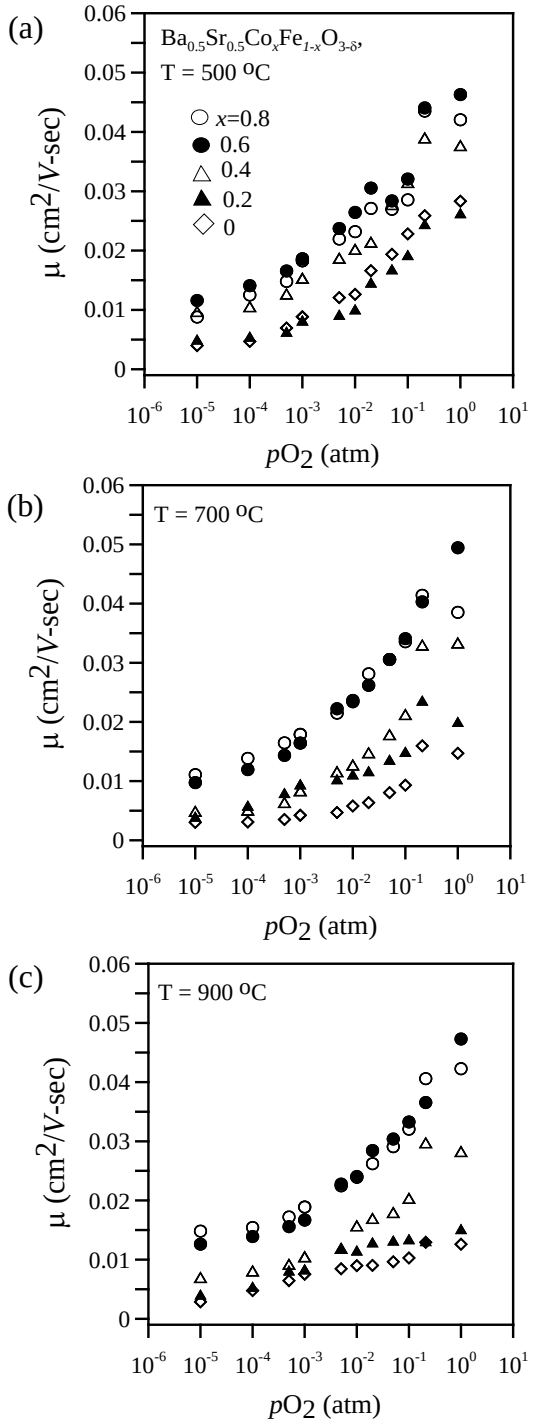

Figure 23. μ (cm^2/V-sec) vs. pO_2 (atm) calculated from conductivity (σ) and Seebeck coefficient (Q) for $Ba_{0.5}Sr_{0.5}Co_xFe_{1-x}O_{3-\delta}$ ($0 \leq x \leq 0.8$) at temperatures of (a) 500°C, (b) 700°C and (c) 900°C.

increasing cobalt concentration at ~ $10^{-3} \leq pO_2 \leq 1$ than at $10^{-5} \leq pO_2 \leq \sim 10^{-3}$, and the trend of which get more dramatic as temperature increases. Particularly, Figure 23 shows that, at x = 0 and x = 0.2, the slopes μ (cm^2/V-sec) vs. pO_2 of 900°C are 0.7×10^{-3} above $pO_2 = \sim 10^{-3}$, and the slopes below $pO_2 = \sim 10^{-3}$ are 0.9×10^{-3}, slightly bending at $pO_2 = \sim 10^{-3}$. It implies that μ is nearly independent of oxygen vacancy formation above $pO_2 = \sim 10^{-3}$, and comparatively drops below $pO_2 = \sim 10^{-3}$, resulting from the disrupted conduction chains of Fe^{4+}–O^{2-}–Fe^{3+} in the hole mobility.[6-7] The abrupt slope decreases of mobility vs. pO_2 at $pO_2 = \sim 10^{-3}$ of 700°C and 900°C are expected to come from the decrease of $[Fe^{3+}]$.

C. Model to Describe Electrical Behavior

For a mixed ionic electronic conductor, the Seebeck coefficient (Q) can be expressed in terms of the contribution of different types of carriers, according to Equation (18) :

$$Q = \frac{\sigma_p Q_p + \sigma_n Q_n + \sigma_i Q_i}{\sigma_p + \sigma_n + \sigma_i} \tag{18}$$

where σ is conductivity and the subscripts refer to holes (p), electrons (n), and ionic carriers(i). Because the ionic conductivity of BSCF has been reported to be on the order of ~0.1S/cm, the contribution of the ionic species to the thermopower will be ignored in the subsequent analysis. Assuming polaron-type transport, the p-type and n-type contributions to the Seebeck coefficient can be expressed as Equations (19) and (20),

$$Q_p = \frac{k}{e}\left[\ln\frac{[B^{3+}]}{\beta_p[B^{4+}]} + \frac{S_T}{k}\right] \tag{19}$$

$$Q_n = \frac{k}{e}\left[\ln\frac{\beta_n[B^{3+}]}{[B^{2+}]} + \frac{S_T}{k}\right] \tag{20}$$

where, k/e is 86.17μV/K, β_p and β_n account for the spin degeneracy of the different cations, S_T is the vibrational entropy associated with ions surrounding the polaron on a given site, and $[M^{n+}]$ is the fractional occupancy of the different species on the B-cation site. The vibrational entropy is often cited as contributing substantially less than 10 μV/K to the measured thermopower and is neglected in the following analysis.[8] Because p-type conduction dominates over the entire temperature range, even when the stoichiometry suggests a significant fraction of B^{2+} species is present, the contribution of n-type carriers to the thermopower will be ignored. Neglecting the contribution of n-type carriers is readily justified if the mobility of the n-type carriers is substantially lower than that of p-type carriers, which is expected for two reasons. First, the larger size of the 2+ cations is expected to result in a higher energy barrier for mobility, and second, the increase in oxygen vacancies when the population of n-type carriers is significant is expected to further decrease mobility by disrupting the B^{2+}-O-B^{3+} chains.[6-7,9]

The fractional concentration of the different species of iron in $Ba_{0.5}Sr_{0.5}FeO_{3-\delta}$ was determined by using Equation (19) along with Equations (21) and (22) below. Equation (21) simply states that the sum of the fractional concentrations of different iron species must equal unity, and Equation (22) describes the contribution of each species to the mean B-site oxidation state (Z_{Fe}, in Figure 18):

$$[Fe^{4+}] + [Fe^{3+}] + [Fe^{2+}] = 1 \tag{21}$$

$$4[Fe^{4+}] + 3[Fe^{3+}] + 2[Fe^{2+}] = Z_B \tag{22}$$

The spin degeneracy factor (β_p) was assumed to be 6/5 as is appropriate for iron in its high spin state. As shown in Figure 24, the fractional concentration of Fe^{4+} decreases with increasing temperature whereas the concentration of Fe^{2+} increases. The concentration of Fe^{3+} remains fairly constant at 0.55 $\pm$ 0.05 over the measured temperature range.

It is important to recognize that uncertainty in the absolute value of the mean oxidation state is quite high, which in turn will affect the calculated values for $[Fe^{n+}]$ shown in Figure 24. As an example, a 2% increase in mean oxidation state of iron results in a decrease in the $[Fe^{2+}]$ concentration at 200°C from ~ 0.06 to its lowest possible value

of zero, but the trends for all [Fe^{n+}] are similar, i.e. the concentration of [Fe^{3+}] remains relatively constant whereas [Fe^{2+}] increases and [Fe^{4+}] decreases with increasing temperature.

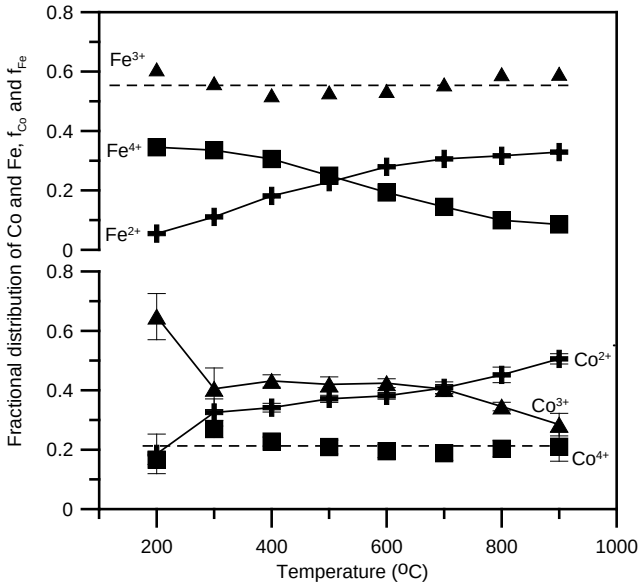

Figure 24. Fraction distribution of iron and cobalt species in $Ba_{0.5}Sr_{0.5}Co_xFe_{1-x}O_{3-\delta}$ deduced from thermopower and oxygen stoichiometry data. See text for details regarding assumptions and calculations.

If one assumes that the relative abundance of iron and cobalt in their different oxidation states, $f_{Fe,n+}$ and $f_{Co,n+}$, does not depend on the Co/Fe ratio, a system of three equations can be developed to calculate the fractional concentration of different cobalt species on the B-site for each BSCF composition. First, Equation (23) expresses the measured Seebeck coefficient in terms of the trivalent and tetravalent species on the B site:

$$Q = \frac{k}{e}\left[\ln\frac{(1-x)f_{Fe,3+} + xf_{Co,3+}}{(1-x)f_{Fe,4+} + xf_{Co,4+}}\right] \tag{23}$$

As before, Equation (23) neglects the entropy of transport term and assumes that B^{3+}-B^{2+} hopping and ionic transport do not contribute significantly to the measured thermopower. For simplicity, Equation (23) assumes that β_p is unity, which is a reasonable approximation considering that the values for high spin iron and cobalt are 6/5 and 5/6, respectively. Second, Equation (24) indicates that the sum of the fractional abundance of the different cobalt species must equal unity:

$$f_{Co,4+} + f_{Co,3+} + f_{Co,2+} = 1 \tag{24}$$

Third, Equation (25) shows the relationship between the fractional abundance of different cobalt species to the mean oxidation state of cobalt, Z_{Co}, shown in Figure 18.

$$4 f_{Co,4+} + 3 f_{Co,3+} + 2 f_{Co,2+} = Z_{Co} \tag{25}$$

It is important to distinguish between $[Co^{n+}]$, which is the fraction of Co^{n+} on the B site, and $f_{Co,n+}$, which is the fraction of cobalt that assumes a n+ oxidation state. The two quantities are related according to $[Co^{n+}] = x\, f_{Co,n+}$. A similar relationship can be developed for iron, where $[Fe^{n+}] = (1-x) f_{Fe,n+}$.

Figure 24 shows the average and standard deviation (error bars) of the four calculated values of $f_{Co,n+}$ as a function of temperature. The fraction of Co^{3+} decreases steadily with increasing temperature whereas the fraction of Co^{2+} increases. The fraction of Co^{4+} remains fairly constant at 0.22 ± 0.03 over the temperature range examined. As mentioned earlier, values for $f_{Co,n+}$ were calculated assuming that the distributions of iron and cobalt were independent of composition. Because the calculated values of $f_{Co,n+}$ varied systematically with composition, the assumption has obvious limitations. Nevertheless, the relatively small standard deviations (error bars) indicate that the assumption yields a reasonable approximation of the redox behavior of Co in the BSCF system.

Carrier mobility (μ) as a function of temperature and composition was calculated using Equation (26):

$$\sigma = pe\mu = \frac{N_a\left([Co^{4+}]+[Fe^{4+}]\right)}{V_m}e\mu \tag{26}$$

where σ is conductivity, p is the p-type carrier concentration in #/cm^3, e is electron charge, N_a is Avogadro's number, and V_m is the molar volume calculated from lattice parameter reported previously. As shown in Figure 25a, the highest mobility values are lower than 0.1 cm^2/V-sec, which is often cited as the upper limit of mobility for polaron hopping.

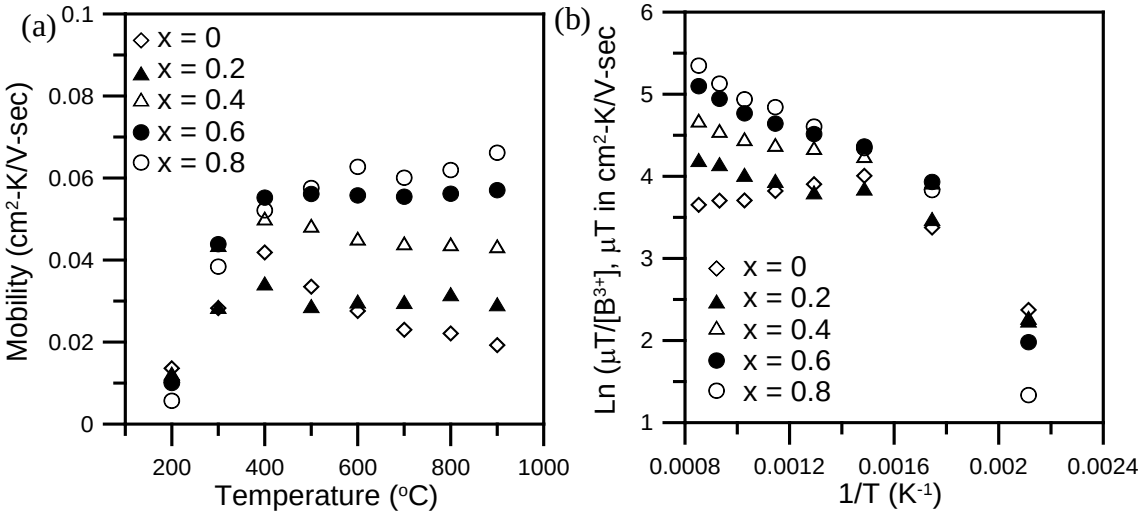

Figure 25. The mobility of $Ba_{0.5}Sr_{0.5}Co_xFe_{1-x}O_{3-\delta}$($0 < x < 0.8$) in air: (a) mobility as a function of temperature, and (b) Ln ($\mu T/[B^{3+}]$) vs. 1/T. Mobility calculated from electrical conductivity and carrier concentration, $[B^{4+}]$, which was inferred from a combination of thermopower and oxygen stoichiometry data.

For adiabatic p-type hopping, mobility can be expressed as Equation (27)

$$\mu = \frac{[B^{3+}]ea^2\nu}{kT}\, e^{-\frac{E_H}{kT}} \tag{27}$$

where e is electron charge, ν is attempt frequency (optical mode phonon frequency), a is jump distance, k is Boltzmann's constant, and E_H is the activation energy for hopping. The concentration of trivalent B cations, $[B^{3+}]$, represents the probability that a B-cation adjacent to the B^{4+} carrier is receptive to the hopping carrier. When plotted in an Arrhenius format, as shown in Figure 25 (b), two regimes are evident – a low temperature regime where the activation energy ranges from 0.2 to 0.6eV and a high temperature regime where the activation energy of the $x \geq 0.2$ samples ranges from 0.05 to 0.1eV, as summarized in Table V. As a point of comparison, Hombo *et al.* reported E_H values of 0.07 eV and 0.3 eV for $SrFeO_{3-\delta}$ and $BaFeO_{3-\delta}$, respectively, in air at 250-350°C.[4] Kozhevnikov *et al.* reported a value of ~0.03eV for p-type carriers in $La_{0.7}Sr_{0.3}CoO_{3-\delta}$ measured at 600-925°C.[9]

Table V. Activation Energies for Conduction and Hopping for $Ba_{0.5}Sr_{0.5}Co_xFe_{1-x}O_{3-\delta}$ ($0 \leq x \leq 0.8$)

Composition	Low Temperature T < 350°C		High Temperature T > 350°C
x	E_A (eV)	E_H (eV)	E_H (eV)
0	0.21	0.23	---
0.2	0.27	0.29	0.053
0.4	0.36	0.38	0.054
0.6	0.43	0.46	0.1
0.8	0.58	0.58	0.13

The positive slope of ln (μT)-vs-1/T for the x = 0 composition precludes the calculation of an activation energy. As a point of comparison, Hobmo *et al.* reported E_H values of 0.07eV and 0.3eV for $SrFeO_{3-\delta}$ and $BaFeO_{3-\delta}$, respectively, in air at 250-350°C.[4] Kozhevnikov *et al.* reported a value of ~0.03eV for p-type carriers in $La_{0.7}Sr_{0.3}CoO_{3-\delta}$ measured at 600 – 925°C.[9]

In the simple ABO_3- perovskites, adjacent B sites are located along the [100] directions and are separated by a distance equal to the lattice parameter, which ranges from 3.932Å for x = 0 to 3.986Å for x = 0.8.[10] When these values are inserted in

Equation (27), the frequency factor is calculated to be on the order of $10^{13}sec^{-1}$, which is expected for optical phonon frequencies and further supports the use of adiabatic polaron model.

As shown in Figure 26, the low-temperature activation energy for mobility is similar to that for conductivity, indicating that changes in mobility rather than changes in carrier concentration dominate the low-temperature behavior of BSCF, as suggested previously. The low-temperature activation energies increase with increasing cobalt concentration. One possible reason for this trend is that oxygen vacancies, which increase with increasing cobalt concentration at a given temperature, disrupt the B^{3+}-O-B^{4+} chains which are instrumental in charge transfer.

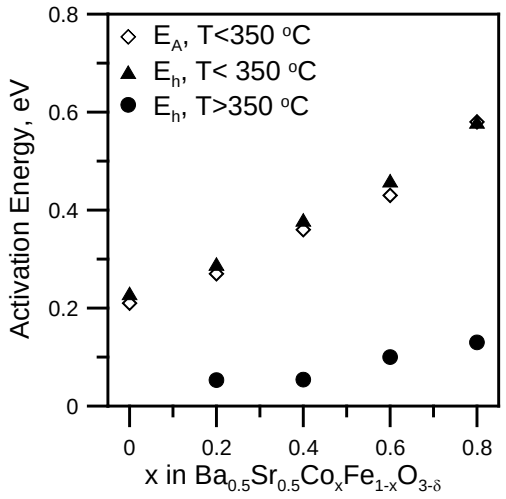

Figure 26. Activation energy for conduction (E_A) and mobility (E_H) as a function of composition.

The high-temperature activation energy also increases with increasing cobalt concentration for $x \geq 0.2$. Again, increases in oxygen vacancy concentration with increasing x can account for the increase in E_H. Because the range of oxygen stoichiometry values among samples with $0.2 \leq x \leq 0.8$ decreases as temperature increases, the range of E_H values (0.05 to 0.13eV) at high temperatures is significantly smaller than the range of E_H values at low temperatures (0.23 – 0.58eV).

The high-temperature activation energies E_H are significantly lower than the low-temperature activation energies. While the change in E_H values corresponds to the onset of oxygen vacancy mobility, the dramatic decrease with increasing temperature is not well understood.

For a mixed ionic and electronic conductor, the Seebeck coefficient (Q) can be expressed in terms of the contribution of different types of carriers, according to Equation (18)

$$Q = \frac{\sigma_p Q_p + \sigma_n Q_n + \sigma_i Q_i}{\sigma_p + \sigma_n + \sigma_i} \tag{18}$$

where σ is conductivity and the subscripts refer to holes (p), electrons (n) and ionic carriers (i).

$$\begin{aligned} Q &= \frac{\sigma_p}{\sigma_p + \sigma_n} Q_p + \frac{\sigma_n}{\sigma_p + \sigma_n} Q_n \\ &= \frac{\sigma_p}{\sigma_p + \sigma_n} \frac{k}{e} \left[\ln \frac{\left[B^{3+}\right]}{\beta_p \left[B^{4+}\right]} \right] + \frac{\sigma_n}{\sigma_p + \sigma_n} \frac{k}{e} \left[\ln \frac{\beta_n \left[B^{3+}\right]}{\left[B^{2+}\right]} \right] \\ &= \frac{\sigma_p}{\sigma_p + \sigma_n} \frac{k}{e} \ln \frac{\left(\left[Fe^{3+}\right] + \left[Co^{3+}\right]\right)}{\beta_p \left(\left[Fe^{4+}\right] + \left[Co^{4+}\right]\right)} - \frac{\sigma_n}{\sigma_p + \sigma_n} \frac{k}{e} \ln \frac{\beta_n \left(\left[Fe^{3+}\right] + \left[Co^{3+}\right]\right)}{\left(\left[Fe^{2+}\right] + \left[Co^{2+}\right]\right)} \end{aligned} \tag{28}$$

where, β_p and β_n account for the spin degeneracy of the different cations with 6/5 and 5/6, respectively, and $[B^{n+}]$ is expected to come from both $[Fe^{n+}]$ and $[Co^{n+}]$. Considering that the contribution of n-type carriers is negligible ($\sigma_p >> \sigma_n$) when the mobility of n-type carriers is substantially lower than p-type carriers, we can also exclude the 2nd term of Equation (29)in the future discussion. Our group reported that, as temperature increases from 200°C to 900°C, $[Co^{4+}]$ and $[Fe^{3+}]$ stay almost unchanged, while $[Fe^{4+}]$ and $[Co^{3+}]$ decrease, and $[Fe^{2+}]$ and $[Co^{2+}]$ increase consistently.[11] This matches well with the

Muller *et al.*'s report that the mean oxidation state of Fe is between +3 and +4 and the mean oxidation state of Co is between +2 and +3 between 510°C and 645°C.[12] Here, we summarize that [Co^{4+}] is originally deficient, and [Fe^{4+}] gets reduced to [Fe^{2+}] by way of [Fe^{3+}] in BSCF. In order to understand the relation between Seebeck coefficient and pO_2, it is necessary to include Equilibrium constants (K) into Equation (29)

$$K_1 : 2\left(Fe_B^{4+}\right)^X + O_0 = 2\left(Fe_B^{3+}\right) + V_O^{\bullet\bullet} + \frac{1}{2}pO_2 \; ; \; \left(\frac{Fe^{3+}}{Fe^{4+}}\right) = \left[K_1\left(\frac{O_O}{V_O^{\bullet\bullet}}\right)\right]^{1/2} pO_2{}^{-1/4}$$

$$K_2 : 2\left(Co_B^{3+}\right)^X + O_0 = 2\left(Co_B^{2+}\right) + V_O^{\bullet\bullet} + \frac{1}{2}pO_2 ; \; \left(\frac{Co^{3+}}{Co^{2+}}\right) = \left[K_2\left(\frac{V_O^{\bullet\bullet}}{O_O}\right)\right]^{1/2} pO_2{}^{1/4}$$

When there is no cobalt concentration, x = 0, Equation 28 can be simplified into Equation (29)

$$Q = \frac{k}{e}\ln\frac{\left(\left[Fe^{3+}\right]\right)}{\beta_p\left(\left[Fe^{4+}\right]\right)} = \frac{k}{e}\ln\frac{1}{\beta_p}\left(\left[K_1\left(\frac{O_O}{V_O^{\bullet\bullet}}\right)\right]^{1/2} pO_2{}^{-1/4}\right) \qquad (29)$$

where, the slope of $Q/(k/e)$ vs. $\ln pO_2$ is -1/4, in which the conduction is expected to be wholly dominated by polaron hopping mechanism, and neither oxygen vacancy nor [B^{2+}] have any effect in Seebeck coefficient.

This calculation is consistent with the result in Figure 22 and Table III, where, as the temperature and cobalt concentration approach to T = 900°C and x = 0 at ~ $10^{-3} \leq pO_2(\text{atm}) \leq 1$, the slope of $Q/(k/e)$ vs. $\ln pO_2$ is near -1/4. On the other hand, the sudden drop of Q at pO_2 = ~ 10^{-3} (sudden change in slope) as pO_2 decreases is understood to come from the initiation of [Fe^{3+}] decrease, when there is no more available [Fe^{4+}] for reduction.

As cobalt concentration(x) is added in BSCF, Q can be rewritten into Equation (30).

$$Q = \frac{k}{e}\ln\frac{\left(\left[Fe^{3+}\right]+\left[Co^{3+}\right]\right)}{\beta_p\left[Fe^{4+}\right]} = \frac{k}{e}\ln\left[\frac{1}{\beta_p}\left[K_1\left(\frac{O_O}{V_O^{\bullet\bullet}}\right)\right]^{1/2} pO_2^{-1/4} + \frac{K_1K_2}{\beta_p}\frac{\left[Co^{2+}\right]}{\left[Fe^{3+}\right]}\right]$$

$$\propto \frac{k}{e}\ln\left[pO_2^{-1/m}\right] \qquad (30)$$

where, -1/m is dependent on $pO_2^{-¼}$ and $[Co^{2+}]$. $[Fe^{3+}]$ is considered to be constant above $pO_2 = \sim 10^{-3}$ as has been discussed with respect to Equation (29). As the cobalt concentration increases, $[Co^{2+}]$ increases and -1/m eventually increases, which matches with the result in Figure 22 and, where the negative slopes of $Q/(k/e)$ vs. $\ln pO_2$ increase from -1/5 to -1/54 with increasing cobalt concentration at 900°C. It implies that the conduction mechanism which is originally dominated by p-type conduction carriers gets affected by the *n*-type charge carrier, mainly by $[Co^{2+}]$, as the cobalt concentration increases.

Figure 27 shows that the whole data of *Q* are plotted vs. lnσ as Jonker plots at temperatures of (a) 500°C, (b) 700°C, and (c) 900°C. At 500°C, the negative slopes of *Q* vs. lnσ are almost linear ranging between -38.9 and -44.3μV/K, as shown in Figure 27(a). As temperature increases, the slopes are no longer linear, and while the negative slopes of high x (x = 0.8) increase, the slopes of low x (x = 0) decrease, approaching to the ideal value, -k/e (86.17 μV/K). Figure 27(c) and Table VI show that, at 900°C, the negative slopes of x = 0.2 and x = 0 are -74.9 and -68.7μV/K, respectively, whereas, in x=0.8, the negative slope is -11.9μV/K with the peak itself located at the lowest Seebeck coefficient and highest conductivity among other concentrations as *Q* = 46.76 and lnσ = 2.95. The increasing cobalt concentration at high temperature accounts for the increase of site occupancy (c) in *p*-type conduction. *n*-type conduction is also considered to take part in the hopping through ($[Co^{+3}]$, $[Fe^{+3}]$) and $[Co^{+2}]$. With increasing cobalt concentration, the number of data points on negative slopes decreases and those on positive slopes have fewer data points above $pO_2 = \sim 10^{-3}$. This trend is consistent with the shift of critical points to higher pO_2 in conductivity and *Q*, as shown in Figure 21 and Figure 22.

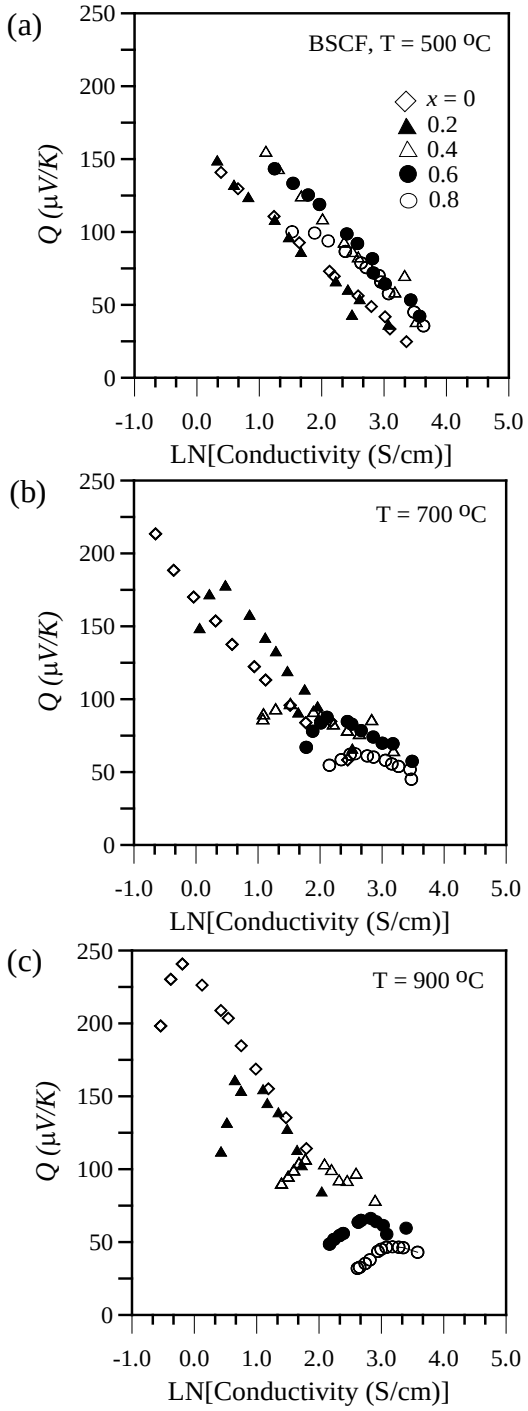

Figure 27. Jonker plots of Seebeck coefficient (Q) vs. ln[σ_{dc}] for $Ba_{0.5}Sr_{0.5}Co_xFe_{1-x}O_{3-\delta}$ (x = 0 ~ 0.8) at temperatures of (a) 500°C, (b) 700°C and (c) 900°C in air using thermoelectric power method.

We suggest that this trend comes from a higher portion of cobalt concentration with a lower valence and more oxygen vacancies, so that Fe can be more easily reduced from +3 into +2, according to Muller *et al.*'s report that, as pO_2 decrease at lower pO_2 (below pO_2 = 1atm), the further reduction causes the preferential reduction of Fe and the additional electrons to preferentially share with Co rather than with Fe.[12]

Table VI. A Summary of the Slopes (*w*) of Seebeck Coefficient (*Q*) vs. $\ln(\sigma_{dc})$ in Jonker Plots For $Ba_{0.5}Sr_{0.5}Co_xFe_{1-x}O_{3-\delta}$ ($x = 0 \sim 0.8$) at Temperatures of 500°C, 700°C and 900°C

w	Positive slopes		Negative slopes		
	700°C	900°C	500°C	700°C	900°C
x = 0	-	120.6	-38.89	-46.66	-68.74
0.2	65.6	142	-41.64	-56.82	-74.9
0.4	20.3	45.2	-43.93	-16.25	-23.27
0.6	59.2	31.5	-44.29	-24.69	-12.08
0.8	22.3	33.8	-40.93	-18.78	-11.94

D. Conclusions

The concentrations of different iron and cobalt species were extracted from thermopower and oxygen stoichiometry data using a simple p-type polaron hopping model. Although the model was built upon several simplifying assumptions, it produced plausible and self-consistent results with respect to the concentration of the different cobalt and iron species. The complex temperature-dependence of the thermopower was explained in terms of p-type polaron hopping between $(Co,Fe)^{4+}$ and $(Co,Fe)^{3+}$ cations with negligible contributions from either n-type or ionic carriers. Derived $(Co,Fe)^{4+}$ and $(Co,Fe)^{3+}$ concentrations were used in conjunction with conductivity measurements to calculate carrier mobility and activation energies. The calculated mobilities were < $0.1 cm^2/V\text{-}s$, further supporting the p-type polaron-hopping model. At temperatures below ~350°C, the activation energy for conduction and for carrier mobility were

essentially identical for a given compositions, ranging from 0.2eV for x = 0 and 0.6eV for x = 0.8. Above 350°C, the activation energy for carrier mobility decreased dramatically, ranging from 0.05eV for x = 0.2 to 0.1eV for x = 0.8. Unlike the carrier mobility of the $x \geq 0.2$ samples, the carrier mobility for the x = 0 sample did not appear to be thermally activated above 350°C.

The increasing cobalt concentration at high temperature accounts for the increase of site occupancy (c) in *p*-type conduction. *n*-type conduction also take part in the hopping through ($[Co^{+3}]$, $[Fe^{+3}]$) and ($[Co^{+2}]$, $[Fe^{+2}]$), which would help oxygen anions to conduct through oxygen vacancy, because a significant amount of oxygen ionic charge carrier concentration within BSCF should be taken into account, which is almost equal to p-type carrier concentration. And the participation of Q_n, which is negative, signifies the decrease of Q, as shown in Equation (18)

As the cobalt concentration increases, more data are located at the positive slopes, while the overall positive slopes decrease, the range of which belongs to $pO_2 \leq \sim 10^{-3}$. A higher portion of Co with lower valence, especially with more oxygen vacancies, can cause Fe to be reduced to +3 more easily, as the critical points shift to a higher pO_2. According to D. N . Muller *et al.*'s report that, as pO_2 decrease at lower pO_2 (below pO_2 = 1atm), further reduction causes the preferential reduction of Fe, and causes the additional electrons to preferentially share with Co rather than with Fe. This is expected to contribute to an improvement of oxygen ionic conductivity.[12] The contribution of oxygen vacancy to oxygen ionic conduction explains the deviation of the slopes of conduction, Seebeck coefficient and Jonker plot from ideal values; 1/4, -1/4 and -86.17μV/K, respectively, as *x* increases and temperature increases up to 900°C and $pO_2 \geq 10^{-3}$.

E. References

1. Z. Chen, R. Ran, W. Zhou, Z. Shao, and S. Liu, "Assessment of $Ba_{0.5}Sr_{0.5}Co_{1-y}Fe_yO_{3-\delta}$ (Y = 0.0-1.0) for Prospective Application as Cathode for IT-SOFCs or Oxygen Permeating Membrane," *Electrochim. Acta*, **52** [25] 7343-51 (2007).

2. J. Jung, S. Misture, and D. Edwards, "The Electronic Conductivity of $Ba_{0.5}Sr_{0.5}Co_xFe_{1-x}O_{3-\delta}$ (BSCF: X= 0 1.0) under Different Oxygen Partial Pressures," *J. Electroceram.,* **24** [4] 261-9 (2009).

3. A. S. Harvey, Z. Yang, A. Infortuna, D. Beckel, J. A. Purton, and L. J. Gauckler, "Development of Electron Holes across the Temperature-Induced Semiconductor-Metal Transition in $Ba_{1-x}Sr_xCo_{1-y}Fe_yO_{3-d}$ (X, Y = 0.2-0.8) : A Soft X-Ray Absorption Spectroscopy Study," *J. Phys.: Condens. Matter,* **21** [1] 015801 10pp. (2009).

4. J. Hombo, Y. Matsumoto, and T. Kawano, "Electrical Conductivities of $SrFeO_{3-\delta}$ and $BaFeO_{3-\Delta}$ Perovskites," *J. Solid State Chem.,* **84** [1] 138-43 (1990).

5. C. Wu, S. Kumarakrishnan, and T. Mason, "Thermopower Composition Dependence in Ferrospinels," *J. Solid State Chem.,* **37** [2] 144-50 (1981).

6. M. V. Patrakeev, J. A. Bahteeva, E. B. Mitberg, I. A. Leonidov, V. L. Kozhevnikov, and K. R. Poeppelmeier, "Electron/Hole and Ion Transport in $La_{1-x}Sr_xFeO_{3-\delta}$," *J. Solid State Chem.,* **172** [1] 219-31 (2003).

7. M. V. Patrakeev, I. A. Leonidov, V. L. Kozhevnikov, and K. R. Poeppelmeier, "P-Type Electron Transport in $La_{1-x}Sr_xFeO_{3-\delta}$ at High Temperatures," *J. Solid State Chem.,* **178** [3] 921-7 (2005).

8. S. Dorris and T. Mason, "Electrical Properties and Cation Valencies in Mn_3O_4," *J. Am. Ceram. Soc.,* **71** [5] 379-85 (1988).

9. V. Kozhevnikov, I. Leonidov, E. Mitberg, M. Patrakeev, A. Petrov, and K. Poeppelmeierc, "Conductivity and Carrier Traps in $La_{1-x}Sr_xCo_{1-z}Mn_zO_{3-\delta}$ (X = 0.3; Z = 0 and 0.25)," *J. Solid State Chem.,* **172** 296-304 (2003).

10. J. Ovenstone, J. Jung, J. White, D. Edwards, and S. Misture, "Phase Stability of BSCF in Low Oxygen Partial Pressures," *J. Solid State Chem.,* **181** [3] 576-86 (2008).

11. J. I. Jung, S. T. Misture, and D. D. Edwards, "Oxygen Stoichiometry, Electrical Conductivity, and Thermopower Measurements of $Ba_{0.5}Sr_{0.5}Co_xFe_{1-x}O_{3-\delta}$ (BSCF : X = 0 ~ 0.8) in Air," Solid State Ionics, 2010 (submitted for publication).

12. D. Müller, J. Brendt, D. Samuelis, and M. Martin, "Oxidation States of the Transition Metal Cations in the Highly Nonstoichiometric Perovskite-Type Oxide $Ba_{0.1}Sr_{0.9}Co_{0.8}Fe_{0.2}O_3$," *J. Mater. Chem.,* **19** [14] 1960-3 (2009).

VI. CONCLUSION AND RECOMMENDATIONS

The main objective of the current study was to understand the conduction mechanism of BSCF perovskite structure ceramics.

This was accomplished mostly through thermo-power measurements as B-site cation ratio changes between cobalt and iron in BSCF. Particularly, as oxygen partial pressure and temperature change, the valence states of B-site cations as well as oxygen vacancy can change significantly, showing that there are transitional points at ~350°C and $pO_2 = 10^{-3}$atm.

XRD analysis indicated that the structural stability of BSCF ceramics is within $\sim 10^{-5} \leq pO_2 \leq 1$atm, so electrical measurement was carried out within $pO_2 = \sim 10^{-5}$atm. When the BSCF structure gets decomposed during annealing under 4% H_2-N_2 gas, the initiation of structural degradation at the grain boundary has been observed through SEM analysis.

For 4pt probe DC measurements, we were able to suggest a defect chemistry model, showing that the sources of oxygen vacancy formation can be understood separately between dopant and temperature effects. And, we quantified the charge carrier concentration by measuring Seebeck coefficient (Q), simultaneously with DC measurement through thermo-power.

Oxygen stoichiometry (3-δ) ranged from 2.65 for x = 0 and 2.54 for x = 0.8 at 100°C to 2.55 for x = 0 and 2.36 for x = 0.8 at 900°C in air. At higher temperatures, the conductivity decreased with increasing temperature and was highly dependent on composition. The Seebeck coefficient was positive for all samples over the entire temperature range measured and exhibited a minimum of $37 \pm 10\mu V/K$ at ~ 300°C. At higher temperatures, the Seebeck coefficient increased with increasing temperature to values ranging from 150μV/K for x = 0 to 67μV/K for x = 0.8.

The calculated mobilities were < $0.1 cm^2/V\text{-}s$, further supporting the p-type polaron-hopping model. At temperatures below ~350°C, the activation energy for conduction and for carrier mobility were essentially identical for all given compositions,

ranging from 0.2eV for x = 0 and 0.6eV for x = 0.8. Above 350°C, the activation energy for carrier mobility decreased dramatically, ranging from 0.05eV for x = 0.2 to 0.1eV for x = 0.8.

With increasing cobalt concentration, more data points are located at the positive slopes, while the positive slopes themselves decrease, the region of which belong to $10^{-5} \leq pO_2 \leq \sim 10^{-3}$atm. Higher concentration of Co with lower valence can cause Fe to be reduced into +3 more easily, as observed in the critical points shifting to a higher pO_2. The contribution of oxygen vacancy to oxygen ionic conduction can possibly explain why the slopes of conduction, Seebeck coefficient and Jonker plot deviate from ideal values; 1/4, -1/4 and -86.17μV/K, respectively, as *x* increases and temperature increases up to 900°C at $pO_2 \geq 10^{-3}$.

The increasing cobalt concentration at high temperature is considered to give rise to *n*-type conduction in the hopping through ($[Co^{+3}]$, $[Fe^{+3}]$) and ($[Co^{+2}]$, $[Fe^{+2}]$). The contribution of Q_n, which is negative, signifies the decrease of *Q*, as shown in Equation (18). On the other hand, because a significant concentration of oxygen ionic charge carriers is included within BSCF, almost equal to that of *p*-type carrier, the contribution of oxygen anionic conduction should be taken into account in Equation (18). Particularly, oxygen anionic conduction is closely related with oxygen vacancy, so that it is necessary to consider the conduction mechanism of BSCF from diverse viewpoints.

Kozhevnikov *et al.* suggested the assumption that some amount of *n*-type carriers and oxygen vacancies may form quasi-neutral associates as ($Co_{Co}^{/}$-$V_o^{\bullet\bullet}$-$Co_{Co}^{/}$) where electrons are strongly localized in $La_{1-x}Sr_xCo_{1-z}Mn_zO_{3-\delta}$.[1] Tuller *et al.* reported that the high hopping energy (E_H) of CeO_{2-x} could be attributed to short ordering within the structure as x increases.[2] Mogni *et al*. reported that the slope deviation from 1/4 in the conductivity plot vs. pO_2 in $Sr_3Fe_2O_{6+\delta}$ is attributed to the occupancy of localized carrier in the neighboring site and associated defects.[3]

Considering our work in combination with other opinions, we suggest the hypothesis that *n*-type polaron hopping is accompanied by the oxygen anion migration through oxygen vacancy near Co^{2+}. But, we need more substantial results to support this idea in BSCF.

A. References

1. V. Kozhevnikov, I. Leonidov, E. Mitberg, M. Patrakeev, A. Petrov, and K. Poeppelmeierc, "Conductivity and Carrier Traps in $La_{1-x}Sr_xCo_{1-z}Mn_zO_{3-\delta}$ (X = 0.3; Z = 0 and 0.25)," *J. Solid State Chem.*, **172** 296-304 (2003).

2. H. L. Tuller and A. S. Nowick, "Small Polaron Electron Transport in Reduced CeO_2 Single Crystals," *J. Phys. Chem. Solids*, **38** [8] 859-67 (1977).

3. L. Mogni, J. Fouletier, F. Prado, and A. Caneiro, "High-Temperature Thermodynamic and Transport Properties of the $Sr_3Fe_2O_{6+\delta}$ Mixed Conductor," *J. Solid State Chem.*, **178** [9] 2715-23 (2005).

VII. APPENDIX : X-RAY PHOTOELECTRON(XPS) STUDY OF BSCF CERAMICS

B. Introduction

The X-ray photoelectron (XPS) of sintered BSCF ceramics ($Ba_{0.5}Sr_{0.5}Co_xFe_{1-x}O_{3-\delta}$, $0 \leq_X \leq 0.8$) was measured. XPS analysis in this study was expected to provide the information on valence states of cations originally, but there was no specific binding energies (BE) observed, which indicate valence changes according to the changes of composition, temperature and oxygen partial pressure. With increasing cobalt concentration, the peak areas of Fe_{2p1}, Fe_{2p3}, Fe_{3p} and Co_{3p} increased systematically, while their Binding Energies (BE) stayed in their typical positions, 723.3, 710.0, 55.0 and 60.9eV, respectively. On the other hand, BE of lattice oxygen in O_{1s}, ~528eV, increased systematically from 528.0 to 528.3eV, and a BE of Ba_{4d}, ~87.9eV, increased from 86.9 to 88.65eV. This supports the idea that unit cell expansion of BSCF intimately affects the bonding state between barium cation and oxygen anion. The shoulder peak of Ba_{3d}/Co_{2p}, ~778eV, systematically increased from 778.0 to 778.7eV, which implies that ~778eV is attributable to another typical Ba XPS peak (named as Ba_{2nd} in this study) coming from the overlapped area between barium cation and oxygen anion. The overall Ba and O XPS peak areas decreased up to x = 0.4, and then increased, which is consistent with the behavior of Diffuse Reflectance Infrared Fourier Transformation (DRIFT) peaks representing CO_3^- and $BaCO_3$ bonds, 800~1200cm^{-1} and 862/1433cm^{-1}, respectively.

C. Results

Figure 28(a) shows the XPS spectra of Fe_{2p} level for the fractured surface of cleaved samples. The peak intensities and areas systematically decrease with increasing cobalt concentration in BSCF (x in $Ba_{0.5}Sr_{0.5}Co_xFe_{1-x}O_{3-\delta}$). The peaks of the $Fe_{2p3/2}$ level become broader and more asymmetric toward the high BE, as x increases. The BE locations of the $Fe_{2p3/2}$ peaks don't change as x changes. The peak BEs at 710.0eV and 723.3eV are assigned to $Fe_{2p3/2}$ and $Fe_{2p1/2}$, respectively, which represent Fe^{+3} species.

Satellite peaks at 717.3eV are also observed to decrease with increasing x. The satellite peak occurring at approximately 8.0eV above the $Fe_{2p3/2}$ is also characteristic of Fe^{+3} species.[1] However, it is difficult to distinguish between Fe^{3+} and Fe^{4+}.[2] Mori *et al.* reported that Fe^{+3} coexists with Fe^{+4} at R.T. with oxygen deficiency in $BaFeO_{3-\delta}$.[3] Falcon *et al.* reported that the bonding strength of Fe^{3+}-O^{2-} and Fe^{4+}-O^{2-} are almost identical.[4]

We therefore conclude that the valence of Fe stays as a mixture of +4 and +3 oxidation states, while Fe ions are primarily in the 4+ oxidation state with lower valence of Co ions in the 3+ oxidation state in $Ba_{0.5}Sr_{0.5}Co_xFe_{1-x}O_{3-\delta}$.[1,5] Figure 28(b) shows the main peaks of the Fe_{3p} and Co_{3p} spectra at 55.0eV and 60.9eV, respectively. All the peaks are quite symmetric within the deviation of ± 0.2eV and increase systematically in their areas and intensities according to increasing x in BSCF.

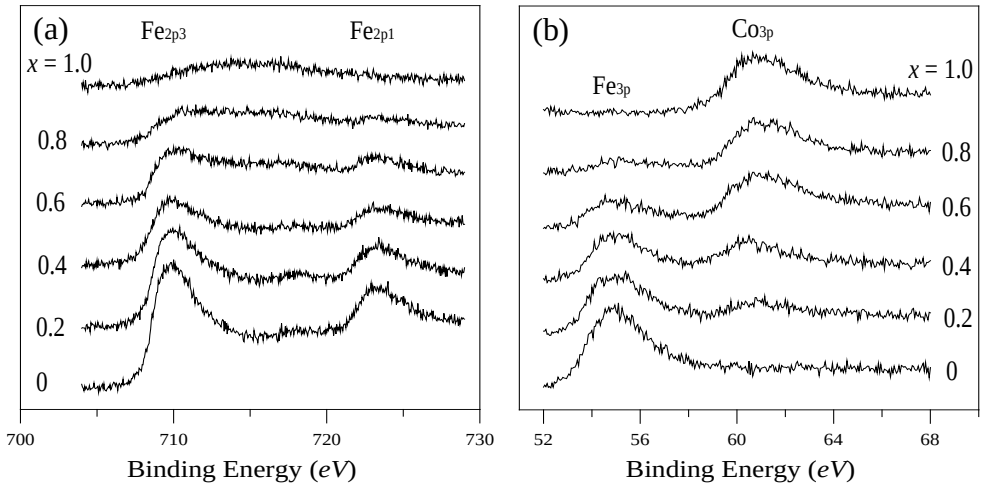

Figure 28. The XPS spectra of (a**)** Fe_{2p} and (b) Co_{3p}/Fe_{3p} for the fractured surfaces of sintered $Ba_{0.5}Sr_{0.5}Co_xFe_{1-x}O_{3-\delta}$ samples.

The peaks at 780.1eV in Figure 29(a) are assigned to both $Co_{2p3/2}$ and $Ba_{3d5/2}$ simultaneously, the peaks of which are indistinguishable from each other. The peak around 780eV in the $Co_{2p3/2}$ typically represents Co^{3+}. The additional peak of the Co^{4+} state, generally located at 2eV higher BE, is not observed in this study.[6] These main peaks at 780.1eV for Co_{2p} / Ba_{3d} represent Co and Ba in the perovskite structure of BSCF,[7] the locations of which peaks stay within the range of ±0.24eV deviation as the

cobalt concentration increases. On the other hand at ~778eV, there are satellite peaks which Falco *et al.* suggest to be due to oxygen deficiency within the perovskite structure.[4] Figure 29(a) shows that, as x increases, the location of satellite peak shifts to higher BE and is eventually absorbed into one large peak at x = 1.0, as summarized Table VII. The normalized area was calculated as a percentage from the real area values.

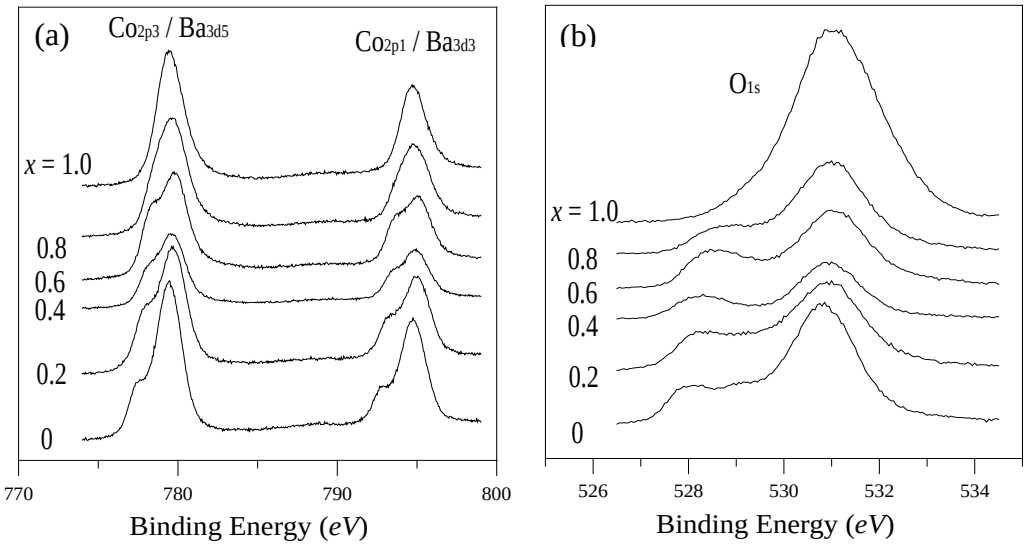

Figure 29. The XPS spectra of (a) Co_{2p}/Ba_{3d} and (b) O_{1s} for the fractured surfaces of sintered $Ba_{0.5}Sr_{0.5}Co_xFe_{1-x}O_{3-\delta}$ samples.

Table VII. Deconvoluted Results of Co_{2p}/Ba_{3d} for $Ba_{0.5}Sr_{0.5}Co_xFe_{1-x}O_{3-\delta}$ XPS Spectra

x	BE		Area		Normalized Area	
	~778eV	780.1eV	~ 778eV	780.1eV	~ 778eV	780.1eV
0.0	777.4	779.4	2900	15055	0.16	0.84
0.2	777.8	779.7	3642	12384	0.23	0.77
0.4	778.4	780.2	1404	7696	0.15	0.85
0.6	778.1	779.7	2577	10939	0.19	0.81
0.8	778.3	779.6	693	13579	0.05	0.95
1.0	779.2	779.7	3216	10977	0.23	0.77

Figure 29(b) show the O_{1s} spectra for BSCF. The O_{1s} spectrum at BSF(x = 0) presents three peaks, with BE values at 528.1, 529.2 and 531.0eV. The lowest binding energy

peak may be ascribed to the lattice oxygen species, O^{2-}, which area systematically decreases with increasing cobalt concentration, as shown in Table VIII. The peak location also shifts to higher BE as *x* increases, similar to the behavior of the Co_{2p}/Ba_{3d} peak in Figure 29 (a). The middle peak, 529.2eV, is assigned to less adsorbed oxygen species, O_2^{2-}/O^-, which is referred to as electrophilic oxygen and known to actively degrade carbon skeleton.[8] The decomposed carbonate (CO_3^{2-}) is expected to adsorb on the surface of BSCF ceramics. The noticeable peak area at 529.4eV of x = 0 (BSF) decreases from 1175 (0.13 as normalized area) to 446 (0.11) up to x = 0.4 and get mixed with the peaks of O^{2-} above x = 0.4. The area of highest BE peak, 531.0eV, which corresponds to CO_3^{2-} or OH^- (CO_3^{2-}/OH^-)[8-9] decreases up to x = 0.4, and then increases above x=0.4. It is noticeable that, as x increases up to x = 0.4, the peak area changes at the middle and highest BE peaks are nearly simultaneous, as summarized in Table VIII.

Table VIII. Deconvoluted Results of O_{1s} for $Ba_{0.5}Sr_{0.5}Co_xFe_{1-x}O_{3-\delta}$ XPS Spectra

x	BE			Area			Normalized Area		
	~528eV	529.4eV	531eV	~528eV	529.4eV	531eV	~528eV	529.4eV	531eV
0.0	528	529	530.8	904	1175	7195	0.10	0.13	0.78
0.2	528.1	529	530.9	722	1382	5460	0.10	0.18	0.72
0.4	528.1	528.7	530.9	330	446	3133	0.08	0.11	0.80
0.6	528.3	529.1	531	913	820	4952	0.14	0.12	0.74
0.8	528.5	529.2	531	633	548	5987	0.14	0.08	0.84
1.0	-	529.1	531.1	-	535	14443	-	0.04	0.96

Figure 30 shows the changes in the Ba_{4d} spectra according to the increase of x in BSCF. Each composition has multiple peaks. Miot *et al.* suggested that the peaks at 87.8eV and 90.3eV represent Ba_{4d} of BaO in the perovskite structure, while the peaks at 89.2eV and 92.4eV are assigned to Ba_{4d} of $BaCO_3$.[10-11] The $BaCO_3$ is expected to come from the bonding between Ba cation and degraded carbonate (CO_3^{2-}) at the surface of BSCF, the reaction of which is promoted by the electrophilic oxygen species, O_2^{2-}/O^-, as explained in Figure 29(b) and Table VIII. Table IX summarizes the peak shifts and areas

for the corresponding Ba_{4d} peaks, after the spectra of each composition in Figure 30 are deconvoluted. With increasing x, the overall peak locations shift to the

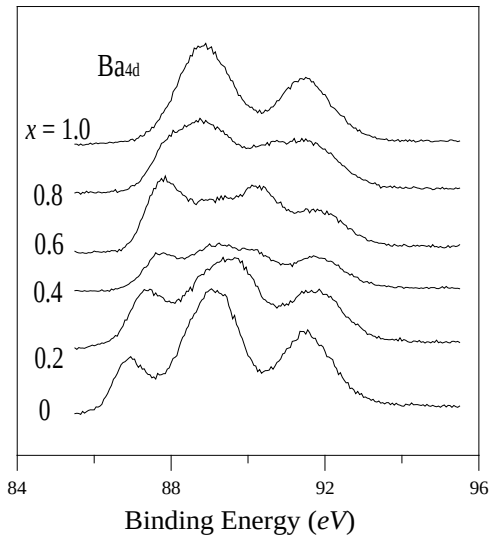

Figure 30. The XPS spectra of the Ba_{4d} for the fractured surfaces of sintered $Ba_{0.5}Sr_{0.5}Co_xFe_{1-x}O_{3-\delta}$ samples.

Table IX. Deconvoluted Results of Ba_{4d} for $Ba_{0.5}Sr_{0.5}Co_xFe_{1-x}O_{3-\delta}$ XPS Spectra

x	Peak Shift				Area				Normalized Area			
	87.9eV	89.2eV	90.2eV	92.4eV	87.9	89.2	90.2	92.4	87.9	89.2	90.2	92.4
0.0	86.9	88.22	89.2	91.48	778	921	2890	2035	0.12	0.14	0.44	0.31
0.2	87.39	88.77	89.75	91.71	1060	1294	1626	1580	0.19	0.23	0.29	0.28
0.4	87.71	89.11	90.23	91.76	593	1173	516	851	0.19	0.37	0.16	0.27
0.6	87.74	88.84	90.2	91.77	1024	1206	1323	1010	0.22	0.26	0.29	0.22
0.8	88.12	89.06	90.5	91.72	1076	1231	1134	1032	0.24	0.28	0.25	0.23
1.0	88.65	89.06	89.62	91.48	1950	364	606	1887	0.41	0.08	0.13	0.39

higher BE, which is quite consistent with the trend for Co_{2p}/Ba_{3p} and O_{1s}. Vasquez *et al.* reported that, as the XPS BE of $Ba_{4d5/2}$ increases from 87.2 to 88.0eV, the Ba-O bond length linearly increases from 2.802 to 2.818Å in Thallium (Tl) – cuprate system.[6] This implies that structural expansion, which is mainly determined by $R_{Ba} + R_O$, does

effectively affect Ba^{2+} cations which are surrounded by oxygen anions such as O^{2-}, O_2^-/O^-, CO_3^{2-}/OH^-, while the BEs of Fe_{2p}, Fe_{3p} and Co_{3p} do not change. On the other hand, the overall peak areas of Ba_{4d} in Figure 30 and Table IX decrease up to x = 0.4 and then increase above x=0.4, both for BaO (87.9eV and 90.2eV) and $BaCO_3$ (89.2eV and 92.4eV).

When the average values of peak area for BaO and $BaCO_3$ are plotted against x in $Ba_{0.5}Sr_{0.5}Co_xFe_{1-x}O_{3-\delta}$, the decreasing and increasing rate of peak area for $BaCO_3$ is greater than for BaO with transitional point of x = 0.4, as summarized in Figure 31. When the peak areas for $BaCO_3$ are substracted by those of BaO, the overall peak areas for $BaCO_3$ increases up to x = 0.4, and then slightly diminish after x = 0.4, as shown in Figure 31.

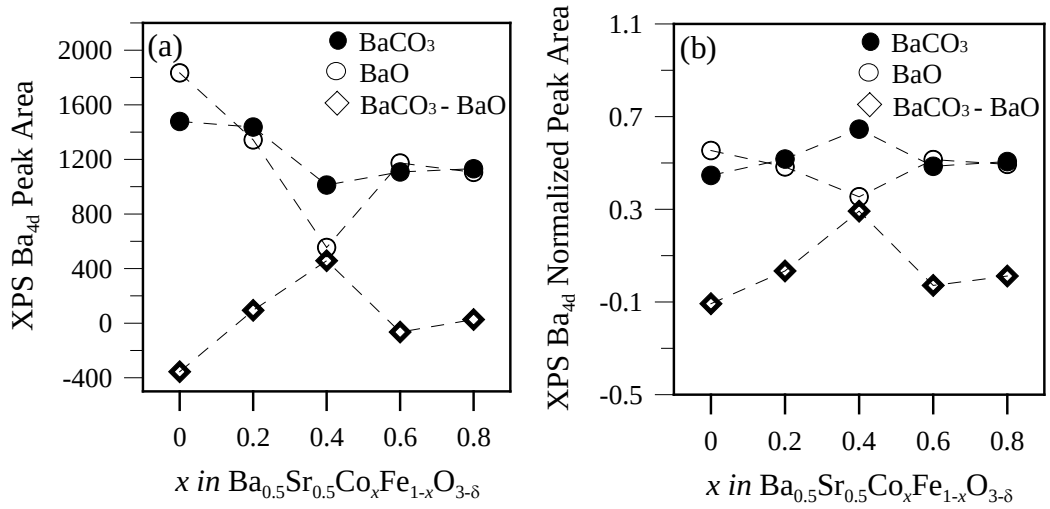

Figure 31. The summary of (a) Ba_{4d} XPS spectra area and (b) Normalized Ba_{4d} XPS spectra area of BaO and $BaCO_3$ for the fractured surfaces of sintered $Ba_{0.5}Sr_{0.5}Co_xFe_{1-x}O_{3-\delta}$ samples.

Figure 32 shows the result of *in situ* DRIFT (Diffuse Reflectance Infrared Fourier Transformation) analysis for the whole compositional range of BSCF, $0 \leq x \leq 1$, as the temperature increases from R.T. to 300°C in air. As x increases up to x = 0.8, the peaks at $758cm^{-1}$ (the wave number marked in Figure 32) representing the $BaCoO_3$ bond on the surface of the perovskite structure get systematically increased, but differently for BSC (x

= 1) with the rhombohedral structure.[12] With increasing x, the peaks from 800 to 1200cm^{-1} (the wave number range marked in Figure 32) representing CO_3^{2-}, decrease up

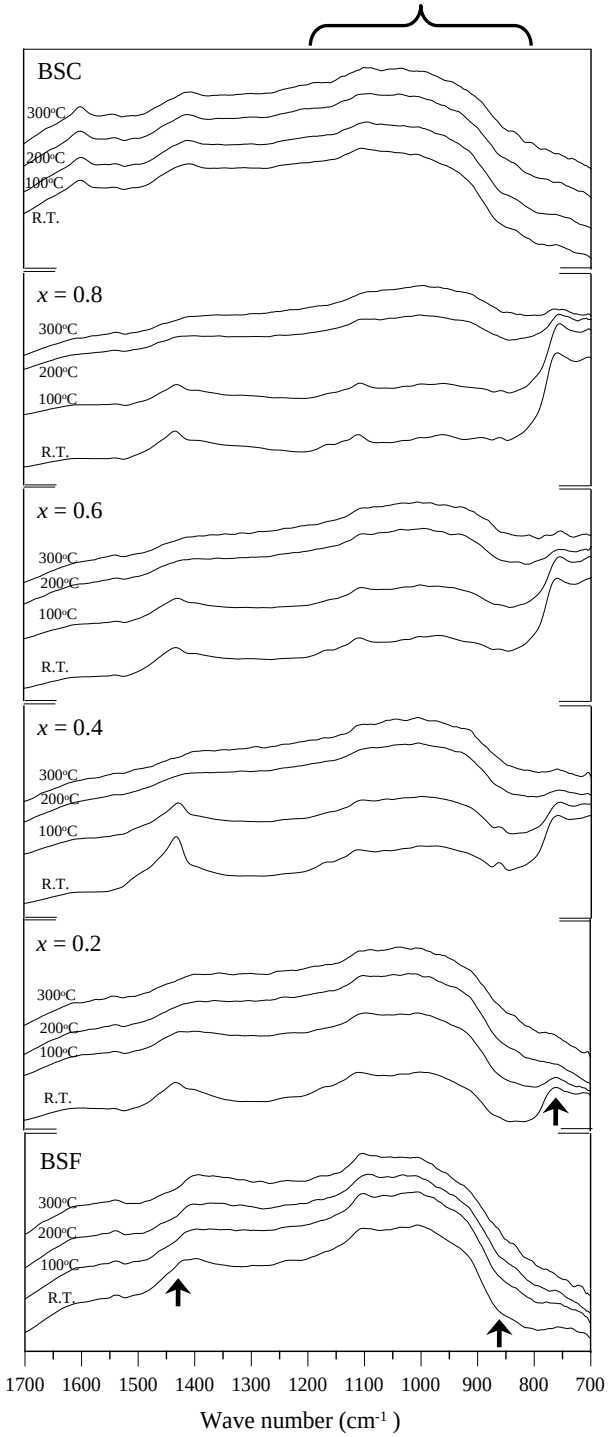

Figure 32. DRIFT (Diffuse Reflectance Infrared Fourier Transformation) spectra of calcined power of $Ba_{0.5}Sr_{0.5}Co_xFe_{1-x}O_{3-\delta}$ samples.

to x = 0.4, and then change little above x=0.4.[13] On the other hand, the DRIFT peaks at 862 and 1433cm^{-1} (the wave numbers marked in Figure 32) for $BaCO_3$ bonding[14] increase up to x = 0.4 and then diminish slightly above x = 0.4, which is consistent with the trend of peak area changes of Ba_{4d} for $BaCO_3$ bonds, as has been explained in Figure 31. We understand that as x increases in $Ba_{0.5}Sr_{0.5}Co_xFe_{1-x}O_{3-\delta}$, the amount of $BaCO_3$ bonds increases at the consumption of CO_3^{2-} up to x = 0.4. On the base of the coincidental trend in the surface analyses of XPS on fractured sintered BSCF samples and DRIFT on the calcined BSCF powders, it is considered that CO_3^{2-} is adsorbed to the surface of BSCF to the maximum at x = 0.4 with increasing x in BSCF.

Figure 33 shows the XRD data for (a) $Ba_{0.5}Sr_{0.5}Co_{0.2}Fe_{0.8}O_{3-\delta}$ (BSCF5528) and (b) $Ba_{0.5}Sr_{0.5}Co_{0.8}Fe_{0.2}O_{3-\delta}$ (BSCF5582) samples which were heat annealed for 48 hours at 700°C and 950°C and cooled down to room temperature under Ar and O_2 gases. When compared with the sintered sample, the overall annealed BSCF5528 samples maintain the cubic perovskite structure, while it significantly expands with 0.8% of expansion rate under Ar, but contracts with 0.45% of contraction rate under O_2, as summarized in Table 1. On the other hand, BSCF5582 expands and contracts relatively at lower rate with 0.2% and 0.17%, respectively, as shown in Figure 33 and Table X.

Table X. Summary of Lattice Parameter and Expansion Rate (%) for $Ba_{0.5}Sr_{0.5}Co_xFe_{1-x}O_{3-\delta}$ (x = 0.2 and 0.8) Samples.

	BSCF5528		BSCF5582	
samples	a(Å)	exp.(%)	a(Å)	exp.(%)
O_2, 950 °C	3.941	-0.51	3.98	-0.15
O_2, 700°C	3.945	-0.4	3.98	-0.2
Sintered samples	3.961	-	3.98	-
Ar, 700°C	3.993	0.81	3.99	0.2
Ar, 950°C	3.994	0.83	3.99	0.2

Particularly, Figure 33 (b) show that BSCF5582 annealed at 700°C under O_2 has a coexistence of cubic and rhombohedral phase at R.T. in air. S. Svarcová *et al.* reported the coexistence of cubic and hexagonal BSCF polymorphs in the region of 850-900°C

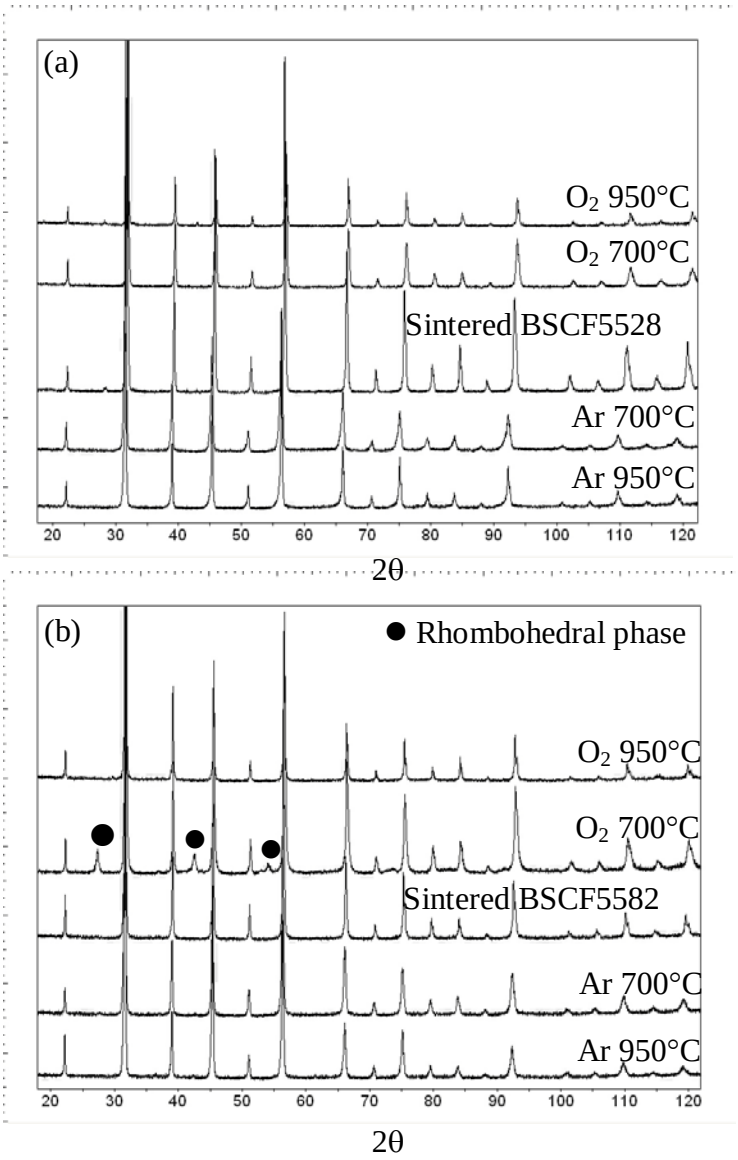

Figure 33. The XRD data of (a) $Ba_{0.5}Sr_{0.5}Co_{0.2}Fe_{0.8}O_{3-\delta}$ (BSCF5528) and (b) $Ba_{0.5}Sr_{0.5}Co_{0.8}Fe_{0.2}O_{3-\delta}$ (BSCF5582) annealed at 700°C and 950°C under O_2 and Ar.

when BSCF5582 is annealed for 10days in air.[15] Kriegel and Preub suggested that higher oxygen partial pressure could favor hexagonal phase formation in BSCF5582 because the hexagonal perovskite very often possesses a higher oxygen stoichiometry than the cubic

phase with the same cationic composition.[16-17] Compared with BSCF5528, BSCF5582 is expected to take in more oxygen within its perovskite structure, because it has a higher concentration of oxygen vacancies.[18] And, as it has relatively higher tolerance factor (t_f) with 1.06, BSCF5582 is more prone to structural distortion with the uptake of oxygen into the perovskite structure under high oxygen pressure, resulting in a phase change to rhombohedral symmetry at 700°C as shown in Figure 33(b).

Figure 34 shows the XPS spectra of Fe_{3p} and Co_{3p} for annealed BSCF5528 and BSCF5582 samples by comparing with the sintered samples in air. The BE of BSCF5528 shows little change in O_2, while there is a significant change in both BEs of Fe_{3p} and Co_{3p} in Ar, especially with the 54.3eV, Fe_{3p} BE at Ar, 950°C. This implies that thermal unit cell expansion can affect the BE of B-site cations in BSCF5528 perovskite structure, but that there is only a slight change in O_2. Figure 34(b) shows BE peak shifts of BSCF5582 according to both annealing conditions (Ar and O_2). Especially, the peak shift for O_2 annealed at 700°C is noticeable, when compared with BSCF5528 in Figure 34 (a).

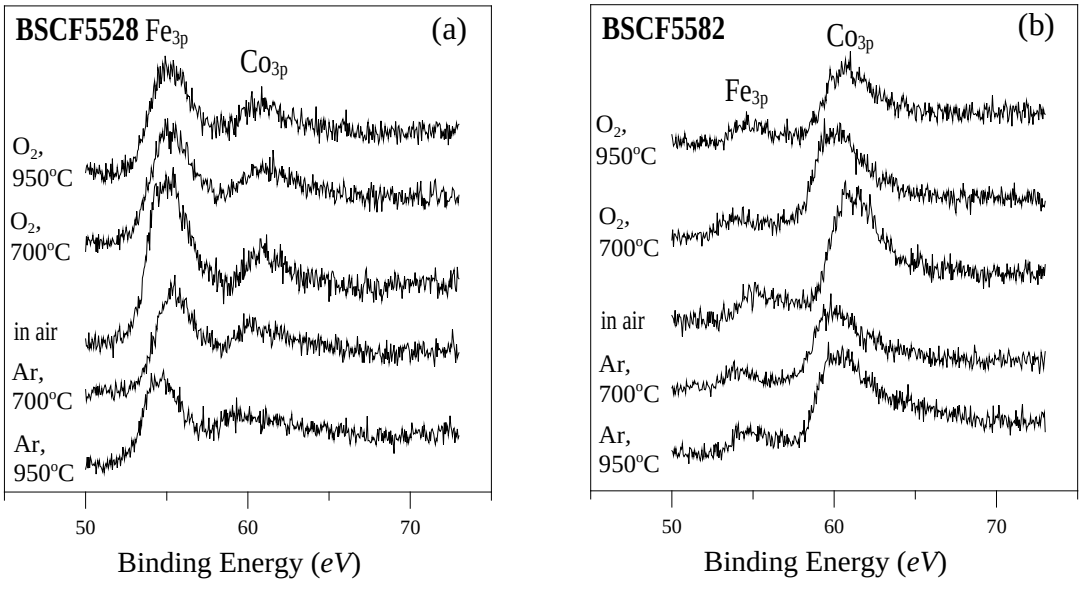

Figure 34. The XPS spectra of Fe_{3p} and Co_{3p} for the fractured surfaces of sintered (a) BSCF5528 and (b) BSCF5582 annealed at 700°C and 950°C under O_2 and Ar.

Figure 35 shows the XPS spectra of O_{1s} for BSCF5528 and BSCF5582. In BSCF5528, the BE of lattice oxygen (O^{2-}) shows systematic increases from 527.9eV, in O_2 at 950°C to 528.3eV, in Ar at 950°C, as shown in Table XI. In Figure 35 and Table XI, the peak areas of BSCF5528 are relatively well distributed in O^{2-} , O_2^-/O^- and CO_3^{2-} /OH^- in O_2. However, the BE of lattice oxygen (O^{2-}) in BSCF5582 changes differently according to annealing conditions, and shows noticeable increase of spectrum in O_2. It indicates that BSCF5582 has a significant amount of oxygen uptake within the lattice under oxidation conditions, enough to lead to structural distortion at 700°C, as shown in the XRD data of Figure 33. The peak areas of O^{2-} in BSCF5528 under Ar are reduced significantly.

The general trend in the peak shifts of Co_{2p}/Ba_{3d} shown in Figure 36 is quite similar to the peaks of O_{1s} in Figure 35. The particular increase of the shoulder peak (~778eV) area of BSCF5582 heat annealed in O_2 shown in Figure 36(b) matches with those peaks (~528eV) in O^{2-} of O_{1s} BSCF5582 shown in Figure 35(b), the trend of which can be more quantitatively compared in Table XI and Table XII. This signifies that the shoulder peak at ~778eV is another type of Ba XPS peak (Ba_{2nd}) which comes from the interrelation between Ba cation and oxygen anion.

Figure 37 shows the XPS spectra of Ba_{4d} for BSCF5528 and BSCF5582. In BSCF5528, the overall peaks shift to higher BE as samples are reduced, which is similar to the behavior of the O_{1s} peak in BSCF5528, as shown in Figure 35(a). When the BaO peaks represented by 89.2/92.2eV and the $BaCO_3$ peak areas represented by 87.9/90.2eV are compared, the peak areas of $BaCO_3$ preferentially decrease in Ar and increase in O_2, as summarized in Table XIII. This implies that BSCF5528 uptakes oxygen preferentially into $BaCO_3$ bonds under oxidation and loses oxygen preferentially from $BaCO_3$ bonds under reduction. The peak changes of BSCF5582 according to oxidation/reduction shown in Figure 37(b) are too irregular and hinder substantial analysis, probably a result of the great intake of oxygen into oxygen lattice sites.

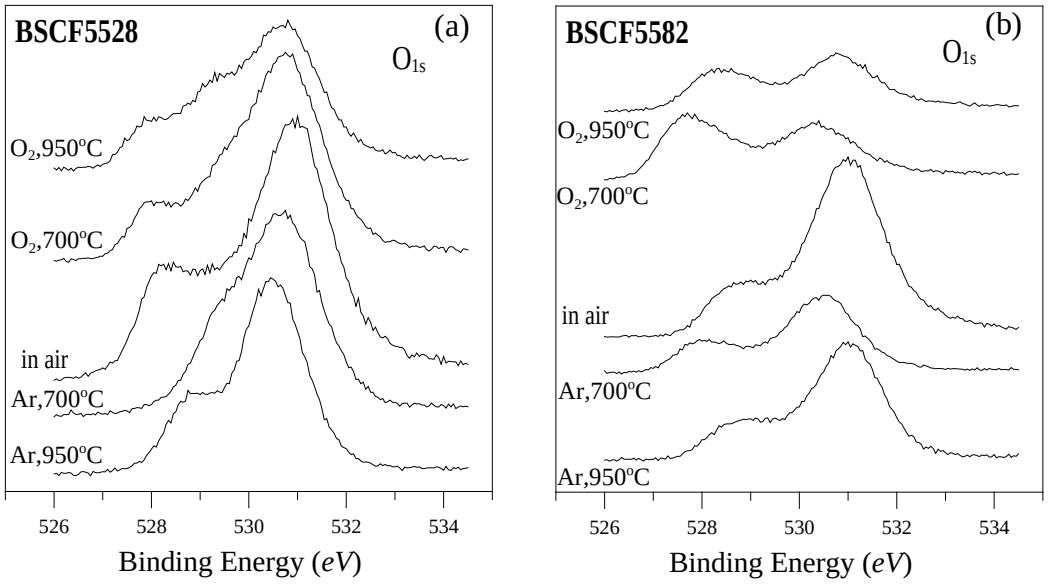

Figure 35. The XPS spectra of O_{1s} for the fractured surfaces of sintered (a) BSCF5528 and (b) BSCF5582 heat annealed at 700°C and 950°C under O_2 and Ar.

Table XI. Deconvoluted Results of O_{1s} for $Ba_{0.5}Sr_{0.5}Co_xFe_{1-x}O_{3-\delta}$ (x = 0.2 and 0.8) XPS Spectra

	BE (eV)			Area			Normalized Area		
	O^{2-}	O_2^-/O^-	CO_3^{2-} /OH^-	O^{2-}	O_2^-/O^-	CO_3^{2-} /OH^-	O^{2-}	O_2^-/O^-	CO_3^{2-} /OH^-
O_2, 950°C	527.9	529.1	530.7	466	992	3233	0.10	0.21	0.69
O_2, 700°C	528.1	529.3	530.85	610	813	4594	0.10	0.14	0.76
As sintered BSCF5528	528.1	529	530.9	722	1382	5460	0.10	0.18	0.72
Ar, 700°C	528.6	529.3	530.66	218	616	4475	0.04	0.12	0.84
Ar, 950°C	528.3	528.9	530.48	214	695	3679	0.05	0.15	0.80
O_2, 950°C	528.3	529	530.81	646	418	1737	0.23	0.15	0.62
O_2, 700°C	527.9	528.8	530.38	841	87	1093	0.42	0.04	0.54
As sintered BSCF5582	528.5	529.2	530.96	633	548	5987	0.09	0.08	0.84
Ar, 700°C	527.9	528.7	530.47	372	301	2242	0.13	0.10	0.77
Ar, 950°C	528.3	529.1	531	262	855	3414	0.06	0.19	0.75

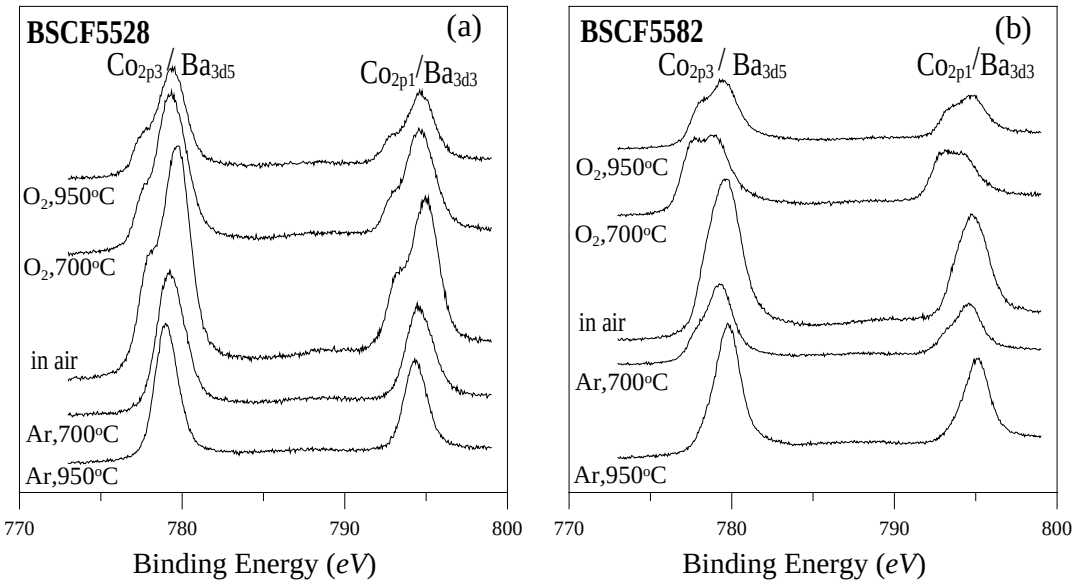

Figure 36. The XPS spectra of Co_{2p}/Ba_{3d} for the fractured surfaces of sintered (a) BSCF5528 and (b) BSCF5582 heat annealed at 700°C and 950°C under O_2 and Ar.

Table XII. Deconvoluted Results of Co_{2p} /Ba_{3d} for $Ba_{0.5}Sr_{0.5}Co_xFe_{1-x}O_{3-\delta}$ (x = 0.2 and 0.8) XPS Spectra

	BE (eV)		Area		Normalized Area	
	~778eV	780.1eV	~778eV	780.1eV	~778eV	780.1eV
O_2, 950°C	777.47	779.34	283	1614	0.15	0.85
O_2, 700°C	777.62	779.46	320	2172	0.12	0.88
As sintered BSCF5528	777.84	779.67	1060	1294	0.23	0.77
Ar, 700°C	778.94	779.35	1342	242	0.09	0.91
Ar, 950°C	778.7	779.1	1137	185	0.12	0.88
O_2, 950°C	777.9	779.44	1064	5470	0.16	0.84
O_2, 700°C	777.38	778.81	1698	6572	0.21	0.79
As sintered BSCF5582	778.33	779.57	693	13579	0.05	0.95
Ar, 700°C	777.72	779.23	683	5804	0.11	0.89
Ar, 950°C	778.28	779.75	644	9131	0.07	0.93

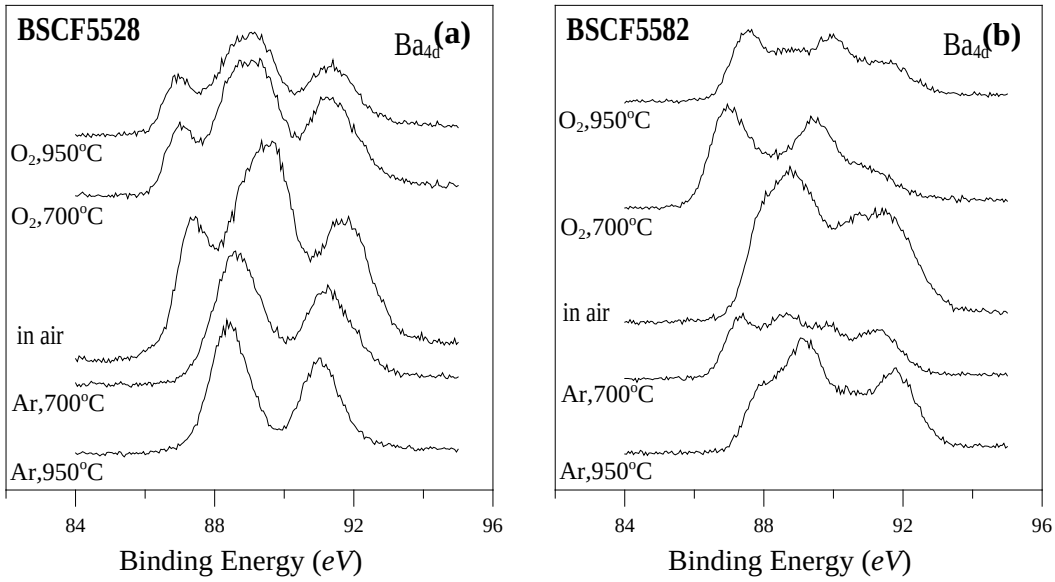

Figure 37. The XPS spectra of B_{4d} for the fractured surfaces of sintered (a) BSCF5528 and(b) BSCF5582 heat annealed at 700°C and 950°C under O_2 and Ar.

Table XIII. Deconvoluted Results of Ba_{4d} for $Ba_{0.5}Sr_{0.5}Co_xFe_{1-x}O_{3-\delta}$ (x = 0.2 and 0.8) XPS Spectra

	BE (eV)				Normalized Area			
	87.9eV	89.2eV	90.2eV	92.4eV	87.9eV	89.2eV	90.2eV	92.4eV
O_2, 950°C	86.9	88.91	90.9	91.5	0.11	0.63	0.02	0.24
O_2, 700°C	86.95	88.93	90.9	91.5	0.09	0.64	0.01	0.26
As sintered BSCF5528	87.39	88.77	89.75	91.71	0.19	0.23	0.29	0.28
Ar, 700°C	88.56	89.52	91	91.7	0.50	0.09	0.25	0.16
Ar, 950°C	88.35	89.14	90.9	91.5	0.49	0.08	0.31	0.11
O_2, 950°C	87.52	88.64	89.9	91.5	0.29	0.17	0.34	0.20
O_2, 700°C	86.99	88.8	89.7	91	0.32	0.42	0.16	0.10
As sintered BSCF5582	88.11	89.08	90.35	91.56	0.24	0.30	0.13	0.33
Ar, 700°C	87.38	88.54	89.7	91.2	0.25	0.23	0.25	0.27
Ar, 950°C	88.01	89.2	90.5	91.8	0.18	0.39	0.13	0.29

D. Discussion

With increasing cobalt concentration, the XPS BEs correlated with Ba-O bonds systematically increased, which is in line with the increasing unit cell volume and oxygen vacancy concentration. It is also noticeable that, even though the lattice parameter is determined by the bonding between B-site cations and oxygen anoins, the XPS BEs of typical Fe and Co peaks do not shift. This signifies that increased lattice parameter accompanied by oxygen vacancy formation could significantly affect the BE of Ba and O. The high t_f of BSCF at the high cobalt concentration in BSCF implies that the electron densities of Ba and O can be overlapped.

As the lattice parameter increases, the electron density around Ba and O would decrease and Madelung potential would increase, which will lead to the increase of BE, as shown in the Ba and O XPS peaks, which is evidently observed by the increase of shoulder peaks in Co_{2p}/Ba_{3d}, ~778eV from 777.4 to 778.3eV.

And, the subtracted peak area of $BaCO_3$ by BaO increased up to x = 0.4 and then decreased, which matches with the increase of $BaCO_3$ (862 and 1433 cm^{-1}) in the DRIFT analysis. This can be attributed to the absorption of CO_3^{2-} into $BaCO_3$ up to x=0.4 at the consumption of CO_3^{2-} which is expected to come from degraded carbon skeleton. This argument is supported by the decrease of CO_3^{2-} (800~1200cm^{-1}) peaks up to x = 0.4 in DRIFT.

In oxidation conditions for BSCF5582, there was significant uptake of oxygen within perovskite structure as shown in O_{1s} and Co_{2p}/Ba_{3d}. The reason for this can be ascribed to the high oxygen non-stoichiometry(δ) within the BSCF55282 structure, which is considered to enable the structure to take more oxygen into oxygen sites. In combination with the high oxygen intake, the high t_f in BSCF5582 can distort the perovskite structure, as shown in the co-existence of rhombohedral and cubic phase at 700°C, O_2 in the XRD data of Figure 33(b). Such a phase change is not observed at 900°C, in O_2 for BSCF5582, because the phase change of BSCF5582 is not viable above 900°C, according to S. Švarcová *et al.*'s report.[15]

The effect of interrelation between Ba and O is also observed in both the BEs areas of ~778eV(Ba_{3d}) and 528eV(O_{1s}), which increased significantly in O_2. Therefore, we are able to suggest two possibilities for the identity of the BE at ~778eV: i) another

oxidation state of Ba_{3d} and ii) the secondary shoulder peak of Ba_{3d}. But, it is not yet clear which assumption is more plausible. However, this study makes it clear that ~778eV comes from the interrelation between Ba and O.

In BSCF5528, the BE of lattice oxygen (O^{2-}) shows systematic increases from 527.9eV in O_2 at 950°C to 528.3eV in Ar at 950°C, as shown in Figure 35 and Table XI, which matches with the unit cell expansion of XRD data in Figure 33(a).

The BE of CO_3^{2-}/OH^- in BSCF5528 do not follow systematic increase but decrease in reduction conditions. Considering that the work function, ϕ, lies in the band gap between the surface energy level and the conduction level, we expect the BE peak shift of CO_3^{2-}/OH^- for O_{1s} to the lower BE under reduction (Ar at 700°C and Ar at 950°C) in Figure 35 to come from metallization of cations. This argument can be supported with the assumption that the polarizability of CO_3^{2-}/OH^- is greater than O^{2-}, that the BE of CO_3^{2-}/OH^- can easily be shifted to lower BE under reduction conditions despite the fact that there are no significant BE changes in cations or O^{2-}.

The preferential uptake of oxygen into $BaCO_3$ bonds under oxidation and loss of oxygen out of $BaCO_3$ in BSCF5528 under reduction, as illustrated in Figure 37, explains the hump number change from three to two as the BSCF structure loses oxygen. This in turn is the reason that three peaks of Ba_{4d} at x = 0 systematically change into two peaks as x increases to x = 1, as shown in Figure 30, for, as the oxygen non-stoichiometry (δ) increases, oxygen from $BaCO_3$ is preferentially removed.

E. Conclusions

With increasing cobalt concentration, the XPS BEs of Ba_{4d} and O_{1s} increased, while the BEs representing Co and Fe did not change, the reason for which can be explained by various aspects such as lattice parameter, tolerance factor, the overlapped zone between Ba and O, and so forth. For a more detailed explanation, a deeper study is required.

The increasing shoulder peaks, at ~778eV, for Co_{2p}/Ba_{3d} from 777.4 at x = 0 to 778.3eV x = 0.8 explains that this peak stands for another typical Ba_{3d} XPS peak coming from the interrelation between Ba and O.

The relative increase in $BaCO_3$ peak areas over BaO explains that CO_3^{2-} adsorbs as $BaCO_3$, which is supported by the decrease of DRIFT CO_3^{2-}(800~1200cm^{-1}) peaks up to x = 0.4.

In oxidation condition for BSCF5582, there was significant uptake of oxygen in the oxygen lattice sites, because of high oxygen non-stoichiometry (δ) within BSCF55282, which, combined with high t_f, causes phase changes at 700°C, O_2 of BSCF5582. We can assume that a phase transition point between 700 and 950°C under O_2 for BSCF5582.

The preferential uptake and loss of oxygen in $BaCO_3$ (Ba_{4d}) of BSCF5528 explain the peak number changes from three to two as the BSCF structure loses oxygen on the fractured sample surface. This also explains the systematic peak number change from three at x=0 into two at x=1.0, in which oxygen non-stoichiometry (δ) increases with increasing x, $0 \leq x \leq 1$.

F. References

1. P. Mills and J. Sullivan, "A Study of the Core Level Electrons in Iron and Its Three Oxides by Means of X-Ray Photoelectron Spectroscopy," *J. Phys. D: Appl. Phys.*, **16** [5] 723-32 (1983).

2. Y. Cho, K. Choi, Y. Kim, J. Jung, and S. Lee, "Characterization and Catalytic Properties of Surface La-Rich $LaFeO_3$ Perovskite," *Bull. Korean Chem. Soc.*, **30** [6] 1368-72 (2009).

3. K. Mori, T. Kamiyama, H. Kobayashi, K. Itoh, T. Otomo, and S. Ikeda, "Local Structure of $BaFeO_{3-D}$ Studied by Neutron Scattering," *Phys. B (Amsterdam, Neth.)*, **329-333** [Part 2] 807-8 (2003).

4. H. Falcon, J. Barbero, J. Alonso, M. Martinez-Lope, and J. Fierro, "$SrFeO_{3-\delta}$ Perovskite Oxides: Chemical Features and Performance for Methane Combustion," *Chem. Mater*, **14** [5] 2325-33 (2002).

5. J. Ovenstone, J. Jung, J. White, D. Edwards, and S. Misture, "Phase Stability of BSCF in Low Oxygen Partial Pressures," *J. Solid State Chem.*, **181** [3] 576-86 (2008).

6. R. Vasquez, M. Siegal, D. Overmyer, Z. Ren, J. Lao, and J. Wang, "Chemical Bonding in Tl Cuprates Studied by X-Ray Photoemission," *Phys. Rev. B: Condens. Matter Mater. Phys.*, **60** [6] 4309-19 (1999).

7. E. Fardin, A. Holland, K. Ghorbani, and P. Reichart, "Enhanced Tunability of Magnetron Sputtered BaSrTiO Thin Films on C-Plane Sapphire Substrates," *Appl. Phys. Lett.,* **89** 022901 3pp. (2006).

8. N. Merino, B. Barbero, P. Eloy, and L. Cadús, "$La_{1-x}Ca_xCoO_3$ Perovskite-Type Oxides: Identification of the Surface Oxygen Species by XPS," *Appl. Surf. Sci.,* **253** [3] 1489-93 (2006).

9. S. Rousseau, S. Loridant, P. Delichere, A. Boreave, J. Deloume, and P. Vernoux, "$La_{1-x}Sr_xCo_{1-y}Fe_yO_3$ Perovskites Prepared by Sol-Gel Method: Characterization and Relationships with Catalytic Properties for Total Oxidation of Toluene," *Appl. Catal., B,* **88** [3-4] 438-47 (2009).

10. C. Miot, E. Husson, C. Proust, R. Erre, and J. Coutures, "X-Ray Photoelectron Spectroscopy Characterization of Barium Titanate Ceramics Prepared by the Citric Route. Residual Carbon Study," *J. Mater. Res.*, **12** [9] 2388-92 (1997).

11. M. Viviani, M. T. Buscaglia, P. Nanni, R. Parodi, G. Gemme, and A. Dacca, "XPS Investigation of Surface Properties of $Ba_{1-x}Sr_xTiO_3$ Powders Prepared by Low Temperature Aqueous Synthesis," *J. Eur. Ceram. Soc.,* **19** [6-7] 1047-51 (1999).

12. V. G. Milt, M. A. Ulla, and E. E. Miró, "NOx Trapping and Soot Combustion on $BaCoO_{3-y}$ Perovskite: LRS and FTIR Characterization," *Appl. Catal., B,* **57** [1] 13-21 (2005).

13. L. Forni, C. Oliva, T. Barzetti, E. Selli, A. M. Ezerets, and A. V. Vishniakov, "FT-IR and EPR Spectroscopic Analysis of $La_{1-x}Ce_xCoO_3$ Perovskite-Like Catalysts for NO Reduction by CO," *Appl. Catal., B,* **13** [1] 35-43 (1997).

14. Y. Yang, Y. Jiang, Y. Wang, and Y. Sun, "Photoinduced Decomposition of $BaFeO_3$ During Photodegradation of Methyl Orange," *J. Mol. Catal. A: Chem.,* **270** [1-2] 56-60 (2007).

15. S. Švarcová, K. Wiik, J. Tolchard, H. Bouwmeester, and T. Grande, "Structural Instability of Cubic Perovskite $Ba_xSr_{1-x}Co_{1-y}Fe_yO_3$," *Solid State Ionics,* **178** [35-36] 1787-91 (2008).

16. R. Kriegel and N. Preu, "Dilatometric Determination of Phase Transition Temperatures and Oxidation Temperatures on the Compounds $SrMnO_{3-y}$ and Sr_2MnO_{4-y}," *Thermochim. Acta,* **285** [1] 91-8 (1996).

17. R. Kriegel, R. Kircheisen, and J. Töpfer, "Oxygen Stoichiometry and Expansion Behavior of $Ba_{0.5}Sr_{0.5}Co_{0.8}Fe_{0.2}O_{3-D}$," *Solid State Ionics,* **181** [1-2] 64-70 (2010).

18. J. Jung, S. Misture, and D. Edwards, "The Electronic Conductivity of $Ba_{0.5}Sr_{0.5}Co_xFe_{1-x}O_{3-\delta}$ (BSCF: X= 0 1.0) under Different Oxygen Partial Pressures," *J. Electroceram.,* **24** [4] 261-9 (2009).